SINGLE UPCONVERSION NANOPARTICLE OPTICAL CHARACTERIZATIONS FOR BIOPHOTONIC APPLICATIONS

By

Zhiguang Zhou

Institute for Biomedical Materials & Devices

School of Mathematical and Physical Sciences, Faculty of Science

Supervisors:

Prof. Dayong Jin & Dr. Fan Wang

UTS UNIVERSITY OF TECHNOLOGY SYDNEY

This thesis is presented for the degree of Doctor of Philosophy

Feb 2019

Certificate of Original Authorship

I, Zhiguang Zhou, declare that this thesis is submitted in fulfillment of the requirements for the award of Doctor of Philosophy, in the School of Mathematical and Physical Sciences, Faculty of Science, at the University of Technology Sydney.

This thesis is wholly my own work unless otherwise reference or acknowledged. In addition, I certify that all information sources and literatures used are indicated in the thesis.

This document has not been submitted for qualifications at any other academic institution.

Production Note:

Signature: Signature removed prior to publication.

Date: 25/02/2019

Acknowledgments

Firstly, I would like to thank my supervisor Prof. Dayong Jin who supervised me through my Ph.D. study. He have insights to foresee the trend of our research field and has great ideas of a wide research area related with biomedical photonics and devices. He has a desire for knowing new things and he still keeps reading literature even he is quite a busy man now. He also supported me with his philosophies about researching, team working and presentation. I record some of them in my notebook as the precious gift of my future life. His strong leadership also is a module that influences my life.

Greatly, I would like to appreciate Dr. Fan Wang for his precious supervision and help all through these three and a half years. Fan is a master of all optics topics. His knowledge and skill are one of a kind in this area. Through my research, I learned a lot of knowledge from him. What is more important, he accompanies me through the dark times of my research and tried his best to help me. He is really patient and nice out of my expectation. To be his student, it is a great honour and luxury. People who read this should consider to be his student or colleague if possible.

Next, I would like to acknowledge my colleagues and collaborators. Thanks to the people of the great optical group, including Chao Mi, Chaohao Chen, Yongtao Liu, Xuchen Shan and Baolei Liu. Thank you for a lot of beneficial discussions and helps. This group is like a big family and we have a memorable family lunch every Monday. I also thank the material guys, including Shihui Wen, Chenshuo Ma, Jiayan Liao, Du Li, for providing me the precious particles whose quality is really excellent. Thanks Yuan Liu, Yongtao Liu, Dr. Zhiyong Guo and Dr. Laixu Gao for the days with me in the dark room. Thanks my office mates: Ming Guan, Shihui Wen, Yulong Sun, Yinghui Chen, Wen Ren, Hao He, Chao Mi, Jiayan Liao, Dejiang Wang, Chi Li. I had a lot of fun with you and I appreciate your supports and friendship. I want to thank postdoctoral fellows: Helen Xu, Jiajia Zhou, Gungun Lin, Qian Su, Lixin Zhang, Yiqing Lu, Deming Liu, Hien Duong, and Maryam Parviz for your helps and discussion with me. I would like to also thanks Yingzhu Zhou, Leo Zhang, Baoming Wang, Huan Wu, Bo Shao, and Christian Clark for the help and friendship from you.

Format of Thesis

This thesis follows the conventional format of five chapters. The relationship between these chapters are shown in the flowchart below.
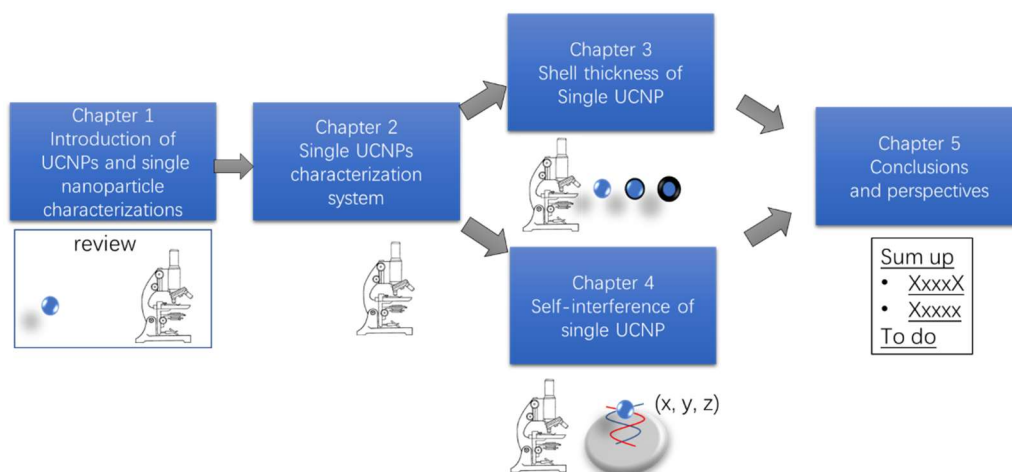
Chapter 1 is the introduction chapter and it has two sections. The first section introduces upconversion nanoparticles (UCNPs). It will introduce the upconversion luminescence mechanism, the material synthesis, the optical properties, and the current applications of UCNP. The second section is a literature review of the current progress in single nanoparticle characterization. It includes the significance and methods of single nanoparticle characterization as well as the specific characterizations and related applications it has already been applied to.

Chapter 2 provides detailed information of systems I developed for this thesis. The single nanoparticle optical characterization system (SNCS) will be introduced. Also, the operations of this system, such as preparation of samples and characterization methods, will be introduced. The applications of this system into cooperative works will also be shown in the last part of this chapter.

Chapter 3 and chapter 4 are the experimental chapters. In chapter 3, the single nanoparticle characterization methods will be applied to research the shell thickness of UCNP to get brighter particles. In chapter 4, the self-interference effects of UCNPs when placing on a mirror is researched and applied to get 3D super resolution position sensing.

Chapter 5 is the conclusions and perspectives of this thesis. The conclusions of this thesis will be summarized, and future works related with my thesis will be prospected.

List of Publications

Research Papers:

1. **Zhou Z**, Wang F, Liu Y, Yang X, Xi P, Xu Z, Kim S, Warkiani S, Jin D et al. *Partly destructive many-emitter self-interference in sub-diffraction limitation volume.* (About to submit)

2. Xu. X, **Zhou Z**, Liu Y, Wen S, Guo Z, , Gao L, Wang F, *Optimising passivation shell thickness of single upconversion nanoparticles using a time-resolved spectrometer.* APL Photonics. 2019, **4**(2): p. 026104.

3. Wang F, Wen S, He H, Wang B, **Zhou Z**, Shimoni O, et al. *Microscopic inspection and tracking of single upconversion nanoparticles in living cells*. Light: Science & Applications. 2018, **7**(4): p. 18007.

4. Guan M, **Zhou Z**, Mei L, Zheng H, Ren W, Wang L, et al. Direct cation exchange of surface ligand capped upconversion nanocrystals to produce strong luminescence. Chemical Communications. 2018, **54**(69): p. 9587-9590.

5. Liu Y, Lu Y, Yang X, Zheng X, Wen S, Wang F, Vidal X, Zhao J, Liu, D, **Zhou Z** et al. *Amplified stimulated emission in upconversion nanoparticles for super-resolution nanoscopy.* Nature. 2017, **543**(7644): p. 229.

6. Ma C, Xu X, Wang F, **Zhou Z**, Liu D, Zhao J, et al. *Optimal sensitizer concentration in single upconversion nanocrystals.* Nano Letters. 2017, **17**(5): p. 2858-64.

7. Ma C, Xu X, Wang F, **Zhou Z**, Wen S, Liu D, et al. *Probing the interior crystal quality in the development of more efficient and smaller upconversion nanoparticles.* The Journal of Physical Chemistry Letters. 2016, **7**(16): p. 3252-8.

([1-7] are closely related to my PhD program)

List of Acronyms

(in alphabetic order)

Abbreviations	Full names
2/3D	Two/three dimensions
AFM	Atomic Force Microscope
ALA	5-Aminolevulinic Acid
CCD	Charge-coupled device
CDs	Carbon Dots
CR	Cross Relaxation
CUC	Cooperative Upconversion
CW	Continuous Wave
demitter	distance change between emitter
DLS	Dynamic Light Scattering
EMU	Energy Migration Mediated Upconversion
ESA	Excited State Absorption
ETU	Energy Transfer Upconversion
FFT	Fast Fourier Transform
FOV	Field Of View
FRET	Fluorescence Resonance Energy Transfer
FWHM	Full Wavelength Half Maximum
IDI	Incomplete Destructive Interference

InM	Interference Microscopy
LUT	Look Up Table
MEANs	Mirror Enhanced Axial Narrowing Super resolution
MOF	Micro-structured Optical Fibers
ND	Neutral Density
NIR(IR)	Near Infrared (Infrared)
NIS	Nanoscale Interferometry Sensor
ODE	1-Octadecene
PA	Photon Avalanche
PALM	Photo-Activated Localization Microscopy
PDT	Photodynamic Therapy
PET	Positron Emission Tomography
PpIX	Protoporphyrin IX
PSA	Prostate Specific Antigen
PSF	Point Spread Function
QDs	Quantum Dots
RESOLFT	Reversible Saturable/Switchable Optical Linear Fluorescence Transition
RGB	Red Green Blue
SIM	Structured Illumination Microscopy
SLBL	Successive Layer-By-Layer

SNCS	Single Upconversion Nanoparticle Characterization System
SP	Short pass
SPAD	single-photon avalanche diode
SPECT	Single-Photon Emission Computed Tomography
STED	Stimulated Emission Depletion
STORM	Stochastic Optical Reconstruction Microscopy
TEM	Transmission Electron Microscopy
UCL	Upconversion Luminescence
UCNP(s)	Lanthanide-Doped Upconversion Nanoparticle(s)
ULISA	Upconversion-Linked Immunosorbent Assay

Abstract

Lanthanide elements-doped upconversion nanoparticles (UCNPs) are of great interest in both biophotonics and nanophotonics. These nanoparticles possess many advantages including low background noise level, low excitation energy, high photostability, tunable wavelength and lifetime, and high tissue penetration depth. However, the development of UCNPs has been hindered by a lack of quantitative analysis technology. Such technologies must have the ability to distinguish a single particle; and the sensitivity to detect the emission lifetime and spectrum of a single particle, both of which are challenging to achieve with the current optical measurement instrumentation.

In my PhD thesis, I will describe a novel single UCNPs characterization method, which offers a way to achieve highly precise, efficient, and quantitative measurements (Chapter 2). This technology will be applied in Chapter 3 to investigate the energy transfer process in the core shell UCNPs. The results revealed that the optimized shell thickness is 6.3 nm for fluorescence probe. In Chapter 4, I used this single particle characterization system to investigate the self-interference phenomenon of UCNPs on a mirror surface. Based on the observed intensity curves, I developed a nanosensor with the ability to detect axial position with 10 nm resolution. More importantly, I found an incomplete destructive

interference (IDI) phenomenon, which may enable real-time super-resolution microscopy in the future. In Chapter 5, conclusions are drawn and the prospectives including single UCNP lasing, mirror enhanced super resolution, and interaction of multi-emitters in a UCNP are introduced.

Key words: upconversion nanoparticles, single nanoparticle characterization, confocal microscopy, core-shell structure, filter-based spectrometer, self-interference, distance sensing, real-time super resolution

Table of Contents

Chapter 1 Introduction

Lanthanide-doped upconversion nanoparticles (UCNPs) have an essential role in the field of nanophotonics and biophotonics. Compared with traditional luminescence materials, UCNPs have many advantages including a low emission threshold, high photostability, and most importantly, a large anti-stokes shift, which results in a low background noise level and a high penetration depth in bioimaging. Moreover, due to the precise control of the doping element and concentration, UCNPs have tunable emission wavelengths and lifetimes, as well as the ability to sense environment perturbation such as temperature and pH change. These advantages allow for a wide range of applications, including anti-counterfeit applications, solar cells, biosensing, bioimaging, and laser therapy. Most importantly, UCNPs are a promising tool for biophotonics owing to their Infrared (IR) excitation wavelength and photostability. In my research, I will focus on the investigation of the optical properties of UCNPs for the development of advanced biophotonics applications such as super-resolution imaging and single particle tracking.

Although high-quality UCNPs have been investigated for more than 10 years, their emission mechanism and applications remain undeveloped due to the lack of an efficient characterisation tool for their complex energy levels. It is essential to obtain a precise, effective, and quantitative way to characterise UCNPs, thereby enabling a better understanding of the upconversion process and allowing wider applications of UCNPs. A stable, straightforward, quantitative method will also encourage commercialisation of the characterisation system and of UCNP probes.

In this chapter, I will provide a comprehensive review of UCNPs. First, I

will introduce the fundamental physics of UCNPs, their synthesis method, and the major applications. Second, I will review the existing single UCNP characterisation methods, their development trends, and their applications. Finally, I will introduce my research, demonstrating how my research benefits the field of single nanoparticle characterisation.

1.1 Introduction to UCNPs

UCNPs, as promising biomarkers, play an important role in biophotonics due to their unique optical properties. This section introduces the working mechanism of UCNPs and describes their biophotonics applications.

1.1.1 Upconversion luminescence mechanism

In the upconversion luminescence system, two or more photons with a longer wavelength (generally IR photons) are absorbed and then one photon with a shorter wavelength (higher photon energy) is emitted. This is where the term "upconversion" originates from.
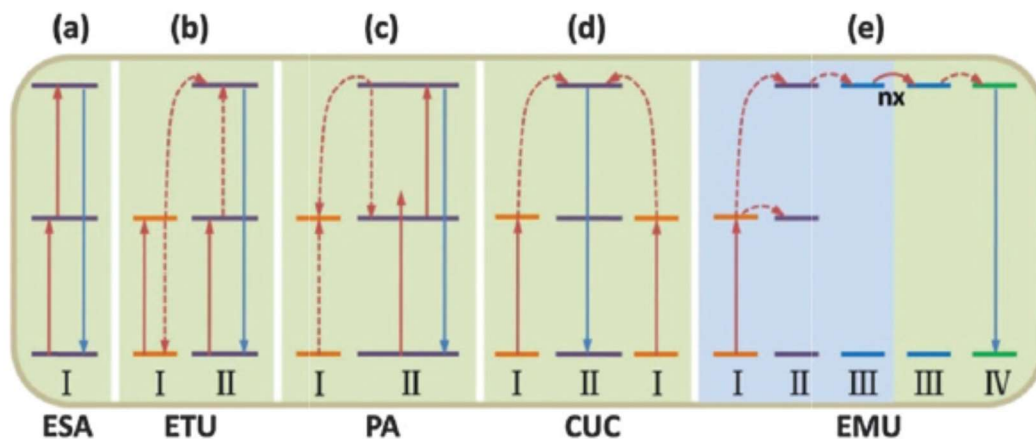
Figure 1.1 The proposed primary upconversion luminescence mechanisms [1]. Excitation state absorption（a）, energy transfer Upconversion (b), photon avalanche（c）, cooperative upconversion （d） and energy transfer upconversion （e）[1].

There are five primary mechanisms proposed underlying the upconversion process. It should be noted that the fifth mechanism, Energy Migration mediated Upconversion (EMU), was only proposed recently by Liu and Wang [2, 3].

The first mechanism, Excited State Absorption (ESA), is shown in Figure 1.1(a). Here, one ion absorbs one photon to the excited state and then it absorbs one more photon from the excited state; decay then occurs to the lower energy state creating upconversion emission. This mechanism only requires the involvement of one ion.

The second mechanism is Energy Transfer Upconversion (ETU). Energy transfer means that there are at least two ions taking part in the process. As shown in Figure 1.1(b), in ETU, one kind of ion acts as a sensitiser. It absorbs photons from the excitation source and transfers the energy to the other ions successively. The other kind of ion is called an activator. It absorbs photons one by one from the sensitiser, exciting it to higher energy levels. Then, decay to the lower energy state occurs to create upconversion emission.

The third mechanism is called Photon Avalanche (PA) (Figure 1.1(c)). This is an unusual mechanism. First, ETU occurs. Second, ESA occurs through which the ions are excited to the high energy level; then upconversion luminescence (UCL) occurs. Next, the cross relaxation (CR) between the high energy level ion and the adjacent ion on the ground state creates two ions on the mediate energy level. Subsequently, with enough excitation power provided, this feedback loop of ESA and CR will exponentially increase the population of intermediate and luminescent levels, thus producing strong upconversion luminescence.

The fourth mechanism is called Cooperative Upconversion (CUC) (Figure 1.1(d)). This involves the interaction of three ions and occurs at a much lower probability than the other mechanisms. In this process, two excited sensitiser ions work together at the same time to pump an activator ion to the excited energy level where upconversion luminescence happens. The activator has no intermediate levels which matches the energy level the sensitiser.

The final mechanism, EMU (Figure 1.1(e)) was first proposed by Liu and Wang[2, 3] in NaGdF4:Yb^{3+}, Tm^{3+}@NaGdF4:Ln^{3+} (Ln=Tb, Eu, Dy, and Sm) core-shell nanostructures. In this process, there are four types of ions: sensitisers (type I), accumulators (type II), migrators (type III), and activators (type IV). Sensitisers absorb photons and transfer them to the accumulator to achieve a higher energy level. However, different to activators, accumulators do not transfer radiance to emission. They pass energy to migrators and the migrators pass energy for some distance to the position where the activator are. Activators finally create upconversion luminescence.

1.1.2 Synthesis of upconversion nanoparticles

UCNPs are generally made of an inorganic host material and lanthanide doping ions. The host materials that have been used include fluorides and other halides (chlorides, bromides, and iodides), oxides, oxysulfides, phosphates, and vanadates. An ideal host material should possess low phonon energy and high chemical stability. Among the host materials mentioned above, fluorides usually have relatively low phonon energy, around 500 cm^{-1}, and also good chemical stability. Thus, fluorides are often used as host materials for UCNPs. To date, NaYF$_4$ is the most popular host material for upconversion materials.

There are three primary methods for the synthesis of upconversion nanoparticles: high temperature coprecipitation, the thermal decomposition method, and the hydrothermal method.

The thermal decomposition method uses organometallic compounds as raw materials. By heating fluoride precursors of lanthanide ions in a noncoordinating reaction solvent (such as 1-Octadecene (ODE)) for a period of time, in the presence of a coordinating ligand, uniform upconversion nanoparticles can be yielded.

The high-temperature co-precipitation method is a more complicated process. First, rare earth ion containing chlorides are added into the mixture containing the coordinating solvent and a noncoordinating solvent. Then, the mixture is elevated to a certain temperature and maintained for a period of time. A homogeneous solution is then formed. This solution is then cooled to room temperature. In the next step, methanol containing a fluorine source is then added, and the methanol is evaporated at certain temperature for a period of time with the reaction solution heated to a high temperature (e.g., 300°C). Then, after Ostwald-ripening, uniform nanocrystals are obtained.

In the hydrothermal method, the system includes three phases: the liquid phase of linoleic acid and ethanol (liquid), sodium linoleate (solid), and the solutions of ethanol and water containing noble metal ions (solution). After the phase transfer, chemical reaction, and product separation processes, nanoparticles are synthesised. Phase transfer occurs when heating the reaction compounds at a certain temperature and pressure (achieved using a sealed reaction vessel). Water and other solvents are in a critical or supercritical state, leading to elevated reaction activity. Thus, the physical and chemical properties of the substances in the solvents are

substantially altered [4].

NaYF$_4$ nanocrystals have two formations of crystal structure: α phase (cubic) and β phase (hexagonal). It has been shown that the β phase is more efficient than the α phase. With recent advances in synthesis, controllable synthesis of β phase NaYF$_4$ has been achieved with the high temperature coprecipitation method (Figure 1.2), thermal decomposition method, or hydrothermal method in both hydrophobic and hydrophilic phases [5]. In addition, the transformation of hydrophobic and hydrophilic UCNPs has also been achieved [6].
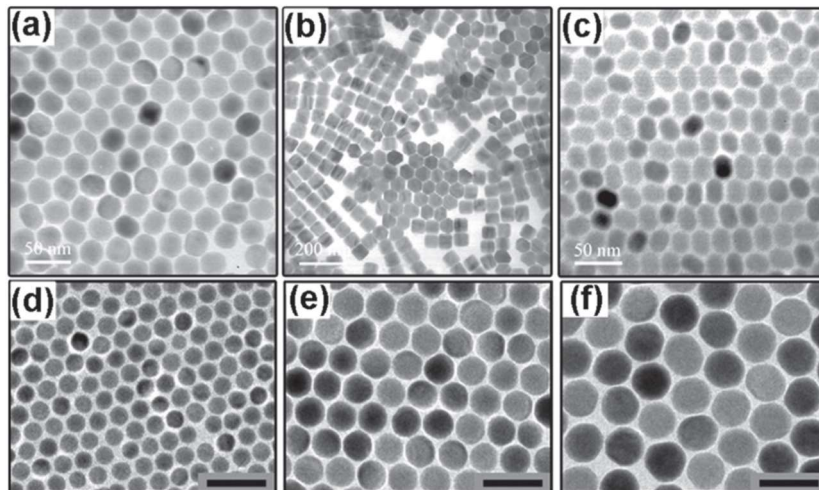
Figure 1.2 (a–c) Transmission Electron Microscopy (TEM) images of NaYF$_4$:Yb/Er UCNPs [7]. (d–f) TEM images of NaGdF$_4$:Yb/Tm UCNPs [8].

1.1.3 Properties of upconversion nanoparticles for biophotonics

Compared with other biomarkers, UCNPs have many advantages such as low background noise, high penetration depth, photostability in upconversion bioimaging, narrow emission bands, and low toxicity.

1.1.3.1 Low background noise

For tranditional biomarkers, there is strong backgroup noise, which is

caused by the autofluorescence phenomenon of the biosamples. Autofluorescence is the fluoresecence from the biosample itself when excited by light source (normally in the UV or blue region). The fluorescence is stokes emission, whose wavelength is longer than the excited light source. Autofluorescence is commonly happened in biosamples and is a big barrier for bio imaging, as it bring strong backgroud noise and blur the target we are observing.

When detecting UCNPs in biological samples, their upconversion emission is shorter than excitation wavelength, which is antistokes emission. The background noise can be reduced to very low, because biosamples do not have upconversion properties under continuous wave (CW) excitation. Thus, by filtering out the excitation light, we can easily get rid of the autofluorescence.

As one example, Figure 1.3 shows that, when placed under excitation, upconversion nanoparticles show strong upconversion luminescence without strong background noise from the sample.
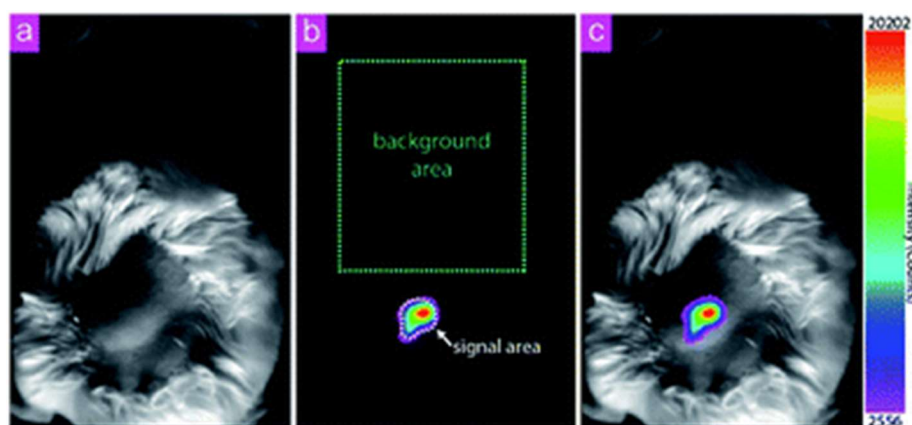
Figure 1.3 In vivo upconversion luminescence imaging with UCNPs. (a) Bright field image, (b) upconversion luminescence image. Signals were collected by a band-pass filter at 800 ± 12 nm, excited with a 980 nm laser source (30 mW cm^{-2}). (c) Merged image of bright field image and the upconversion luminescence signals [9].

1.1.3.2 High penetration depth

The UCNPs are typically doped with Yb^{3+} as sensitiser and other lanthanide ions such as Tm^{3+} and Er^{3+} as an activator. The excitation of Yb^{3+} is normally 980 nm laser and the upconversion emission is from 400 nm to 800 nm. Figure 1.4 shows the famous biological window for optical imaging. Because the excitation and emission wavelengths of the UCNP are inside the range of the NIR-I and NIR-II optical windows, the penetration depth can be high in biological tissues. Due to the flexible doping condition, the excitation wavelength and emission wavelength can be changed to further increase the penetration depth, such as using the Nd^{3+} to tune the excitation wavelength to the 800nm and using the downconverted NIR light to penetrate deeper.
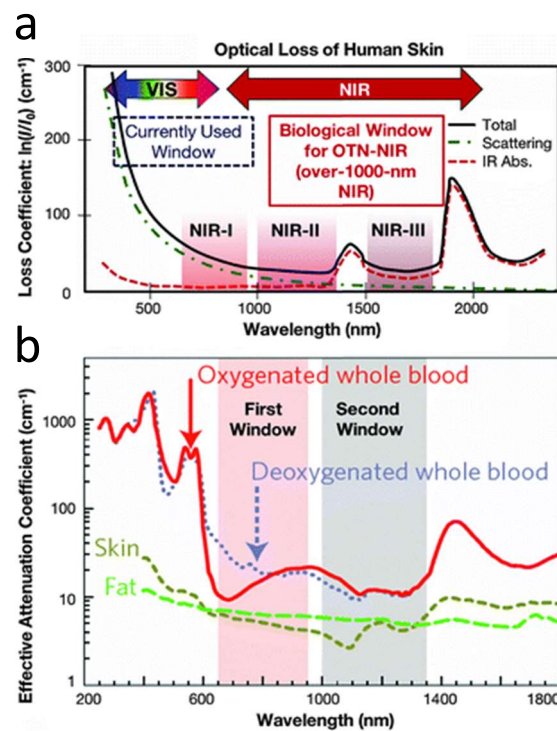
Figure 1.4 (a) Absorption spectrum of human skin showing the first (NIR-I), second (NIR-II), and third (NIR-III) biological windows [10]. (b) Zoom-in of the two first optical windows in some biological tissues and fluids [11] [12].

As another example, Figure 1.5 shows the advantage of the high penetration depth of UCNPs. Generally, 5-aminolevulinic acid (ALA) can convert to the photosensitiser protoporphyrin IX (PpIX) in cancer tumour cells. Irradiation with visible wavelength enables PpIX to convert triplet oxygen into singlet oxygen, thereby inducing cell death. However, the deep tissue absorbs or scatters visible light, substantially decreasing the working efficiency of PpIX. In contrast, with the help of UCNPs, the high penetration depth from the NIR excitation wavelength can reach the target area *in vivo*, as deep as 1.2 cm.
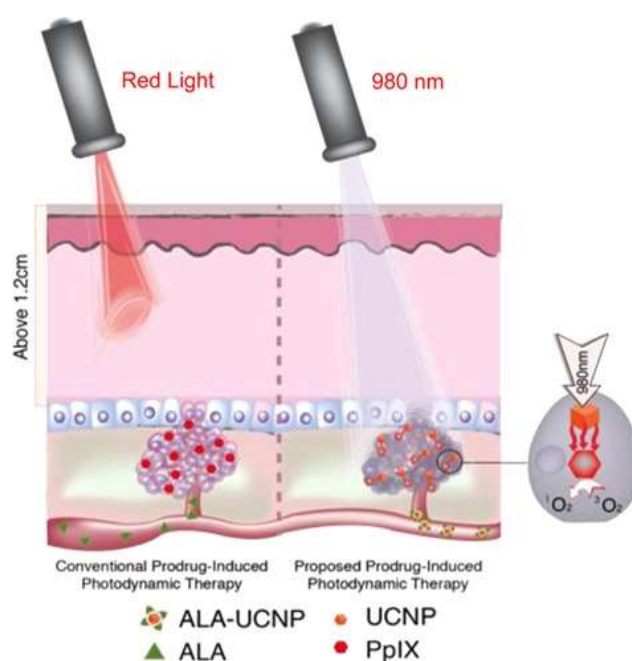
Figure 1.5 UCNPs help to enhance Photodynamic Therapy （PDT） treatment. ALA can convert to PpIX in cancer tumour cells but cannot be used for treatment as there is no red irradiation to trigger drug release (left) On the other hand, the IR excitation laser can penetrate into the target position, and with UCNP's red emission, the PDT drug gets released and can kill the cancer cells (right) [13].

1.1.3.3 Photostability in upconversion bioimaging

The continuous stream of emitted photons traditional bioprobes observed on log time scales is interrupted by dark or off time. Several possible

mechanisms have been discussed to explain the fluorescence intermittency such as intersystem crossing from the singlet excited state (on state) to the triplet state (off state) [14], charge-transfer [15] and conformational changes [16]. In ensemble measurements, this behavior is always hidden because the fluctuations of individual objects are not synchronized. While for single-molecule studies both in vitro and in vivo, the blinking must be avoided to carry out long time characterization and tracking.

The UCNPs has many emitters in one particle, and their emission is of random phase. Therefore its emission would be stable. Further, because of the stable host crystal and the lanthanide ion, the UCNP emission can be stable for a long time without bleaching.

As shown in Figure 1.6, under continuous excitation, the luminescence intensity of UCNPs can remain for a long period, without blinking or photobleaching. This feature makes UCNPs one of the best candidates for luminescent probes. Compared with quantum dots and dyes, this photostability enables tracking and labelling of targets over long periods.
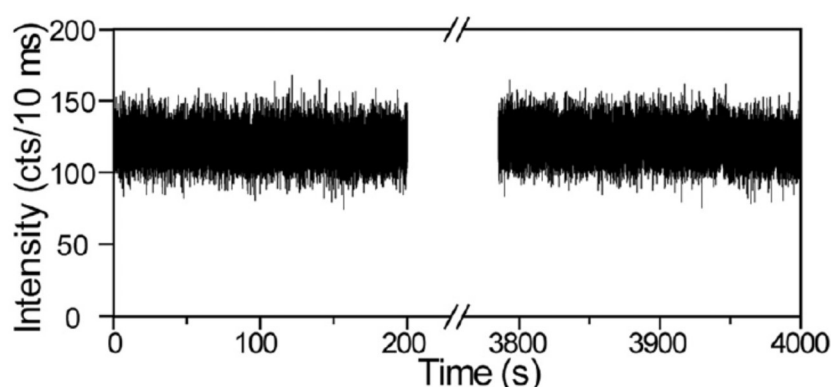
Figure 1.6 Photostability and non-blinking behaviour of a single UCNP. The time trace of emission intensity from a single UCNP under continuous laser illumination for more than 1 hour highlights the durable photostability of UCNPs [17].

1.1.3.4 Narrow emission bands

The lanthanide ions in UCNPs have partially filled 4f orbital electrons and fully filled 5s and 5p electrons. This causes weak electron-phonon coupling, thus when the electronic transition happens, the emission radiance has a narrow band. Due to this, UCNPs have emission bands with a full wavelength half maximum (FWHM) below 10 nm. Further, the emission can cover from UV to NIR with different lanthanide doping ions. Therefore, UCNPs can achieve multiplexing with more channels.

Figure 1.7 shows the narrow emission of UCNPs and the multiplexing abilities of UCNPs achieved by tuning the concentration of doping ions. This colour multiplexing can reach more than 10 channels. Figure 1.7 (a) is the emission of $NaYF_4$:Yb/Er (18/2 mol%). (b), (c) and (d) are $NaYF_4$:Yb/Tm (20/0.2 mol%), $NaYF_4$:Yb/Er (25–60/2 mol%), and $NaYF_4$:Yb/Tm/Er (20/0.2/0.2–1.5 mol%). It is shown that the colour will change when the doping ions are changed. Also, the doping concentration will change the colour. (e)-(n) shows the colours from (a) to (d) which could be distinguishable with naked eyes and feasible to multiplexing.
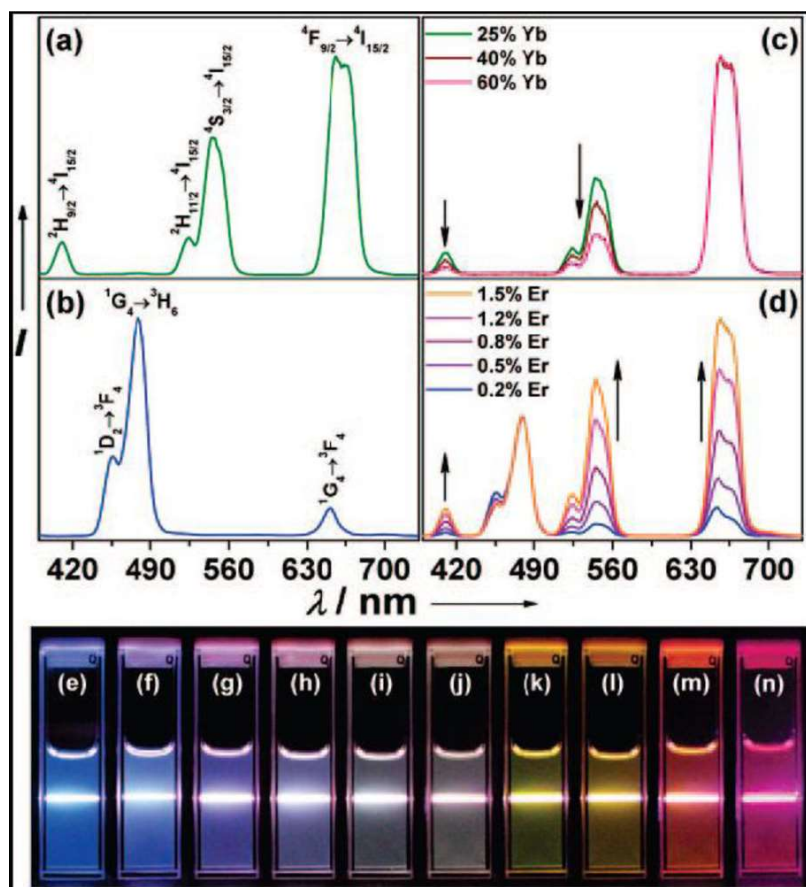
Figure 1.7 Room temperature upconversion emission spectra of (a) NaYF₄:Yb/Er (18/2 mol%), (b) NaYF₄:Yb/Tm (20/0.2 mol%), (c) NaYF₄:Yb/Er (25–60/2 mol%), and (d) NaYF₄:Yb/Tm/Er (20/0.2/0.2–1.5 mol%) particles in ethanol solutions. The spectra in (c) and (d) were normaelised to Er³⁺ 650 nm and Tm³⁺ 480 emissions, respectively. Compiled luminescent photos showing corresponding colloidal solutions of (e) NaYF₄:Yb/Tm (20/0.2 mol%), (f–j) NaYF₄:Yb/Tm/Er (20/0.2/0.2–1.5 mol%), and (k–n) NaYF₄:Yb/Er (18–60/2 mol%). The samples were excited at 980 nm with a 600 mW diode laser [18].

1.1.3.5 Low toxicity

The biosafety of UCNPs is of great importance for their potential application as bioimaging agents. Prof Li performed a systematic review of the toxicity of UCNPs[19]. The available toxicity studies cover cellular internalisation, biodistribution, excretion, cytotoxicity, and *in vivo* toxic effects of UCNPs. The results of this review indicated that UCNPs do not

show any evidence of toxic effects on cells, zebrafish, or mice at certain concentrations. This low toxicity paves the way for various biological applications of UCNPs.

1.1.4 Applications of upconversion nanoparticles

With the efforts of material scientists, UCNPs have been introduced in an increasing number of applications and are becoming promising candidates as next-generation luminescent biomarkers. To date, UCNPs have been applied in fields such as biological imaging, drug delivery, molecular detection, security, display, and optoelectronics.

1.1.4.1 UCNPs for bioimaging

Optical imaging is one of the most facile and straightforward ways to investigate biomedical specimens. For bioimaging applications, down-shifting probes such as fluorescent proteins [20], organic fluorophores [21], metal complexes [22], semiconductor quantum dots (QDs) [23], and carbon dots (CDs) [24] have revealed life science from the single molecular level up to the *in vivo* tissue level [25]. However, these probes are severely limited by their intensity, photostability, autofluorescence, and limited penetration depth. As discussed above, UCNPs can overcome many of these limitations by its advantages such as low backgroud noise and high penetration depth.

UCNPs have been widely used for upconversion photoluminescence imaging *in vitro/in vivo*. As Figure 1.8 illustrates, UCNPs have been successfully used as imaging agents in cells [26], zebrafish [27], and small animals [28, 29], as well as for lymphatic imaging [30], tumour imaging [31], and so on. These researches prove that act as a universal bio-marker, the UCNPs could be beneficial for a large range of life science researches.
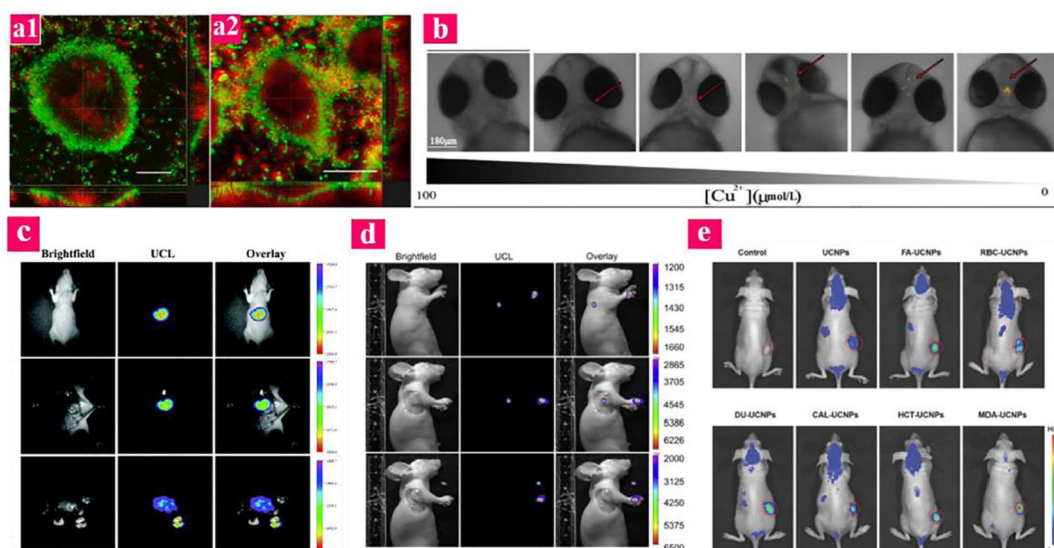
Figure 1.8 Confocal images and upconversion photoluminescence of (a) HeLa cell, (b) zebrafish, (c) a nude mouse acquired 1 h after intravenous injection of UCNPs @mSiO2-Eu(dbm)4 (1 mg/mL), (d) nude mice after injection of Lu-UCNPs, (e) nude mice bearing MDA-MB-435 tumour xenografts [26, 27, 29-32].

Moreover, UCNPs can be used by other imaging technologies as multimodal imaging agents that can be conveniently functionalised with other imaging agents. As such, UCNPs have been applied in magnetic resonance (MR) [33, 34], X-ray computed tomography [34, 35], and positron emission tomography/single-photon emission computed tomography (PET/SPECT) imaging [36, 37] (Figure 1.9). These multimodal imaging applications would be very useful because it will enable us to detect more comprehensive information with just one test.
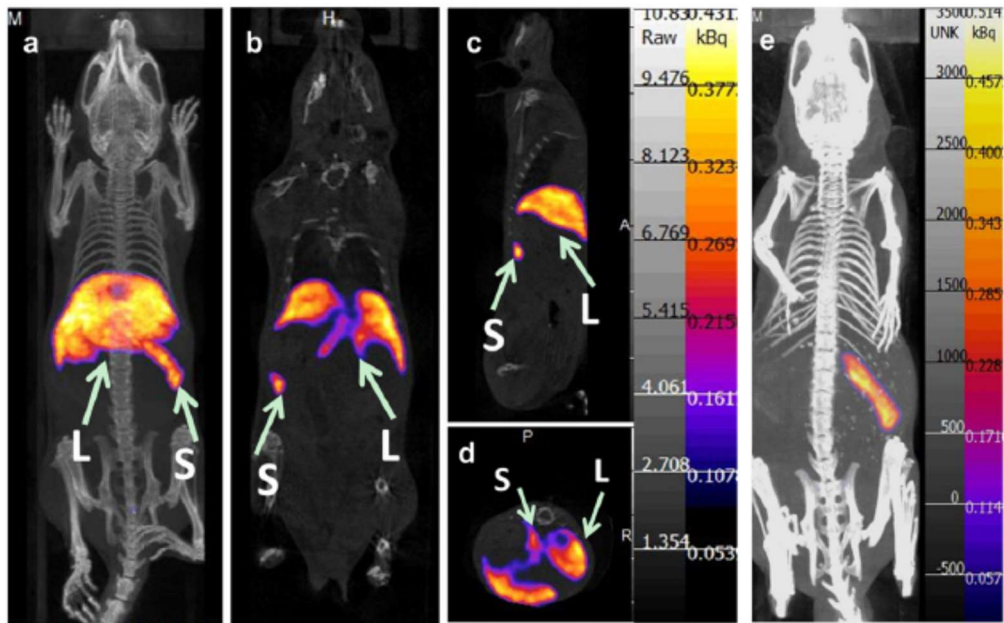
Figure 1.9 In vivo SPECT images after intravenous injection of Sm-UCNPs. (a) Whole-body three-dimensional projection, (b) coronal, (c) sagittal, and (d) transversal images acquired at 1 h, and (e) whole-body three-dimensional projection images acquired at 24 h. The inset arrows point to the liver (L) and spleen (S) [37].

1.1.4.2 UCNPs for drug release

Traditional medical treatments kill cancer cells but at the same time also cause significant damages to healthy cells, which limits their application. Further, the treatment efficiency is low because the drugs are not accurately transferred to the specific target location. Drug release technologies have been developed to enhance the drug uptake efficiency and reduce the side effects of these medications.

Drug carriers like liposomes, polymer micelles, vesicles, and other nanoparticles have been used in these drug release technologies. UCNPs, in particular, provide convenience given that they are long-duration tracking particles that are able to locate the target position without the addition of other contrast agents. Further, UCNPs have excellent optical

properties which enable them to be triggered by diverse ways [38]
including the pH value [39-41] (Figure 1.10), NIR light [42-44], and
temperature, as well as the combination of these factors [45, 46]. These
drug release technologies by UCNPs were promising due to the unique
properties in 1.1.3.
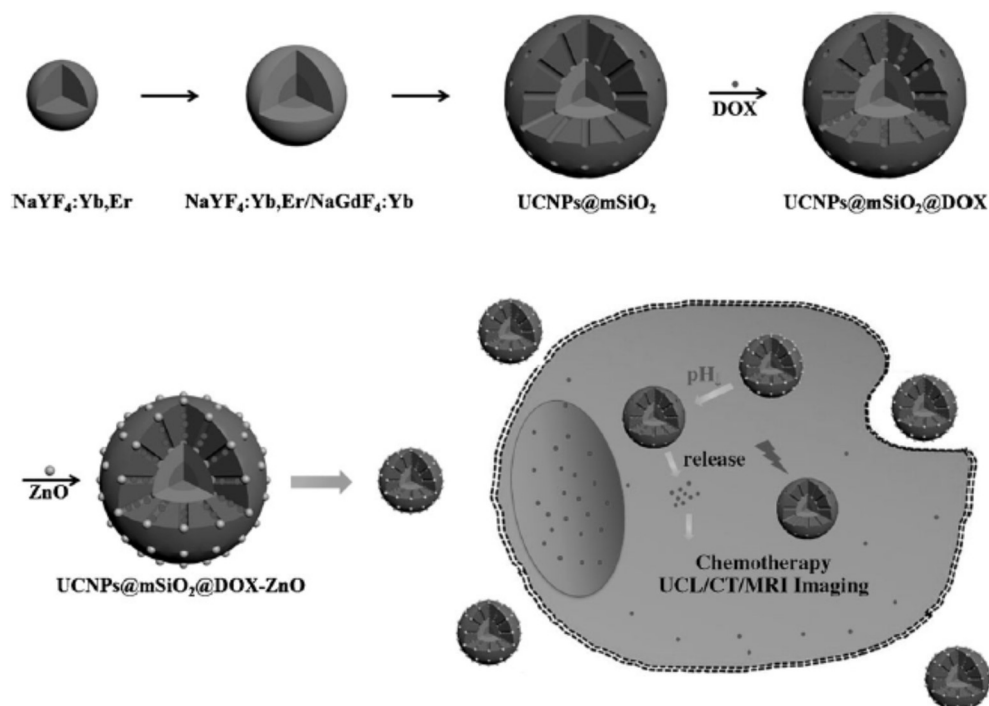
*Figure 1.10 Synthesis of UCNPs@mSiO2@DOX-ZnO for multi-modality bioimaging
guided pH-triggered chemotherapy [40].*

1.1.4.3 UCNPs for biosensing

Fluorescence resonance energy transfer (FRET) is an energy transfer
mechanism between two light-sensitive molecules. A donor, initially in its
electronic excited state, may transfer energy to an acceptor through the
nonradiative dipole-dipole coupling. The efficiency of FRET is inversely
proportional to the sixth power of the distance between the donor and
acceptor, making FRET extremely sensitive to small changes in distance.
FRET works typically within a range of less than 10 nm.

In FRET processes, UCNPs mostly serve as energy donors. Generally, the receptors are sensitive to a specific factor, such as cations, anions, or temperature/pH value. By monitoring changes in the emission of UCNPs, the target factor can be sensed. To date, sensors based on UCNPs and the FRET process exhibit high sensitivity and selectivity. They have been widely applied to various situations, such as cations (Figure 1.11), anions, molecules, pH, and temperature [31].
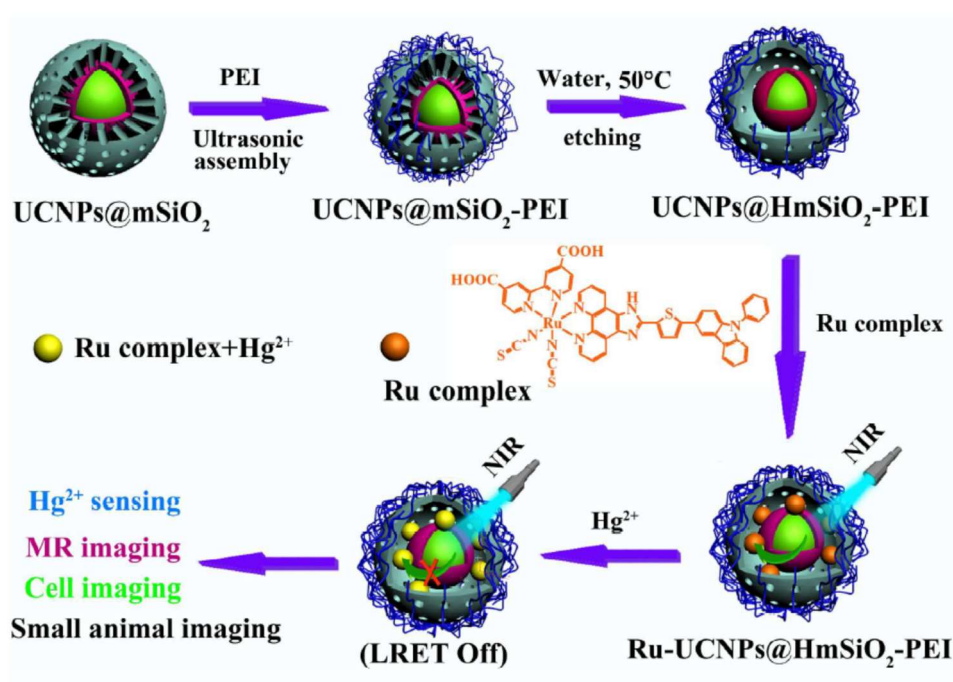
Figure 1.11 Use of UCNPs to detect Hg^{2+} [47].

1.1.4.4 UCNPs for anti-counterfeiting applications

Anti-counterfeiting is very important for item identification. Loss of value in currency and other counterfeited items costs governments and private industries billions of dollars each year. Various anti-counterfeit technologies have been developed to meet this need, including laser holography [48], nuclear track technology [49], and luminescence printing [50, 51]. Among them, luminescence printing is advantageous

because it is designable, high-throughput, and shows advanced anti-counterfeit performance. With comprehensive spatial and spectral information provided, UCNPs fabricated luminescence printing has been widely used in anti-counterfeit technology to enhance encryption strength or feasibility [52-56].

As shown in figure 1.12, the green and blue patterns could be seen with different illumination. Under room daylight, all of the patterns are hidden. While under NIR excitation, there will be a green QR code, and under UV excitation, there will be BEBC characters and the QR code disappears. This two dimension coding could enhance the security obviously.
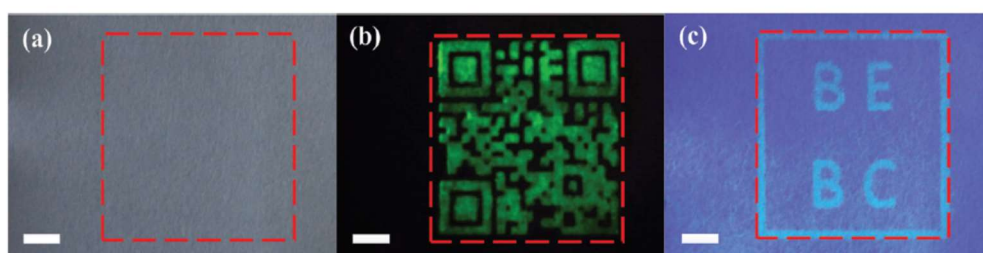
Figure 1.12 Double anti-counterfeiting pattern. (a) Area of both NIR-to-visible and UV-to-visible printing features. (b) The two-dimensional code printed using NIR-to-visible upconversion ink. (c) 'BEBC' mark printed using UV-to-visible downconversion ink. The scale bar represents 2 mm [54].

In addition to the above applications, UCNPs could also be used for solar energy harvesting [57], fingerprint detection [50, 58], and 3D-displays [59].

In summary, UCNPs have shown powerful applications in bioimaging, drug release, sensing, anti-counterfeiting, and several other fields. However, there are still many challenges UCNP are facing, such as smaller and brighter UCNPs and super resolution bioimaging. The development of UCNPs relies not only on material science but also on the

development of characterisation methods. This thesis will focus on developing optical characterisation methods to characterise UCNPs; this characterisation can then be used to identify properties to apply in biophotonics. In the next section, I will introduce the methods for characterisation of UCNPs.

1.2 Characterisation and applications of single UCNPs

1.2.1 Significance of single nanoparticle characterisations
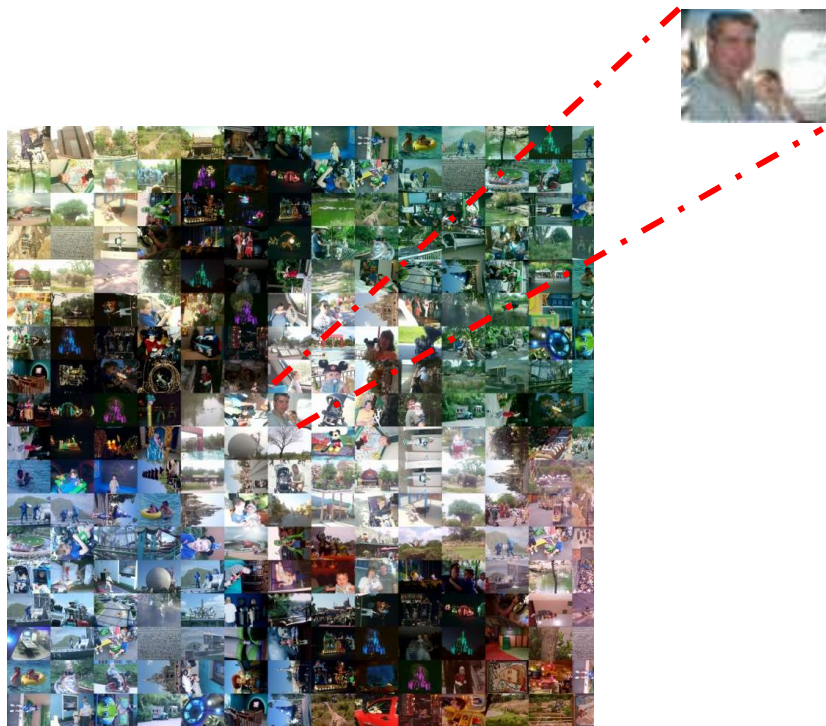
Figure 1.14 Illustration of property differences between single nanoparticles and bulk materials

The characterisation of a material at the single nanoparticle level is key for future nanomaterial research. A simple illustration of this is provided in Figure 1.14. The full picture looks like Micky Mouse®, but the single pieces are entirely different from each other and are of no relevance to Mickey Mouse®.

For nanomaterials, it is similar. The bulk material might show several properties, but in fact, every single nanoparticle may be different from the bulk material. Further, some properties of a single nanoparticle may be hidden without single nanoparticle characterisation. As shown in Figure 1.15, the spectrum of a single UCNP is quite different from the cluster [60], and the upconversion efficiency is also different [61] (Table 1.1).
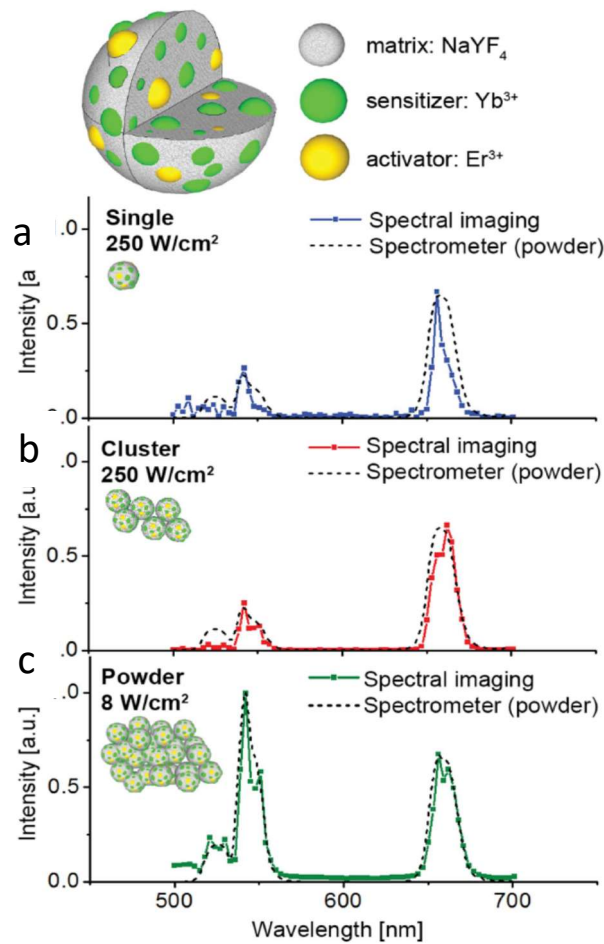
Figure 1.15 Emission spectra of UCNPs in (a) single, (b) small cluster, and (c) powder form [61].

Table 1.1   the absolute upconversion efficiency single and small clusters of UCNPs[61]. Here, P_{em} is photon emission rate, N_{Yb} is number of Ytterbium (Yb^{3+}) ions per node that absorbed the excitation light. σ_{abs} is absorption cross-section, I_{ex} is excitation intensity, η_{uc} is conversion efficiency.

	P_{em} [W] (25%)	N_{Yb} (10%)	σ_{abs} [cm^2] [b)	I_{ex} [W/cm^2](10%)	η_{uc} [%]
Cluster 1[a)	2.6×10^{-14}	5.5×10^5	1.0×10^{-20}	2.6×10^2	2.0 ± 0.5
Cluster 2[a)	2.2×10^{-14}	6.1×10^5	1.0×10^{-20}	2.6×10^2	1.3 ± 0.3
Single[a)	4.9×10^{-15}	2.3×10^5	1.0×10^{-20}	2.6×10^2	1.2 ± 0.3

The characterisation of a single nanoparticle can provide quantitative information about nanoparticles from which we can determine several essential characteristics as shown in Figure 1.16:

a: Single NP location

Single nanoparticle characterisation can provide location correlated information including fluorescence intensity, fluorescence decay lifetime, power dependent properties, etc. With the analysis of data, we can separate particles within a small distance of each other according to their property differences. This creates opportunities for high or super resolution techniques.

As shown in Figure 1.16 (a), with careful characterisation of fluorescent protein, the optical switch on-off property has been identified and scientists have developed this character into the stimulated emission depletion (STED) super resolution technology. With this technology, details within the diffraction limit (<200 nm) can be obtained, enabling researchers to proceed into the nanoscale world. Further, with single

nanoparticle tracking, we can follow the biology reaction process, enabling insight into the dynamic details of biological activities.

b: Inter-particle information

As shown in Figure 1.16 (b), single nanoparticle characterisation also allows inter-particle information to be obtained. Barcode technology is one technology benefitting from this. A barcode is encoded with target information with different emission colours as a code. With single nanoparticle characterisation, we can recognise the barcode information of every single nanoparticle; therefore, each of the barcodes is identified and decoded. Nanoparticle barcode technology is widely used in multiplexing labelling and security. With the development of super resolution technologies, nanoparticles used in barcoding technology can be reduced to a few hundred nanometres. Further, the elements, lifetime, and luminescence can also be investigated within a single nanoparticle.

c: Intra-particle information

As shown in Figure 1.16 (c), Characterisation of single nanoparticles also provides information on intra-particle activation. With interaction between particles, the intensity or lifetime can be enhanced and the wavelength can be shifted. With single nanoparticle characterisation, these interaction parameters can be quantified in detail and further researches can proceed.

d: Weak signal sensing

The development of single nanoparticle characterisation enables advanced detection of weak signals. For example, early cancer symptoms do not have a strong signal in the currently available technologies. For

weak signals, only one or several nanoparticles will exist in the sampling area. Single nanoparticle characterisation technology, together with the help of material and other technologies, enables efficient detection of weak signals, as shown in Figure 1.16 (d).
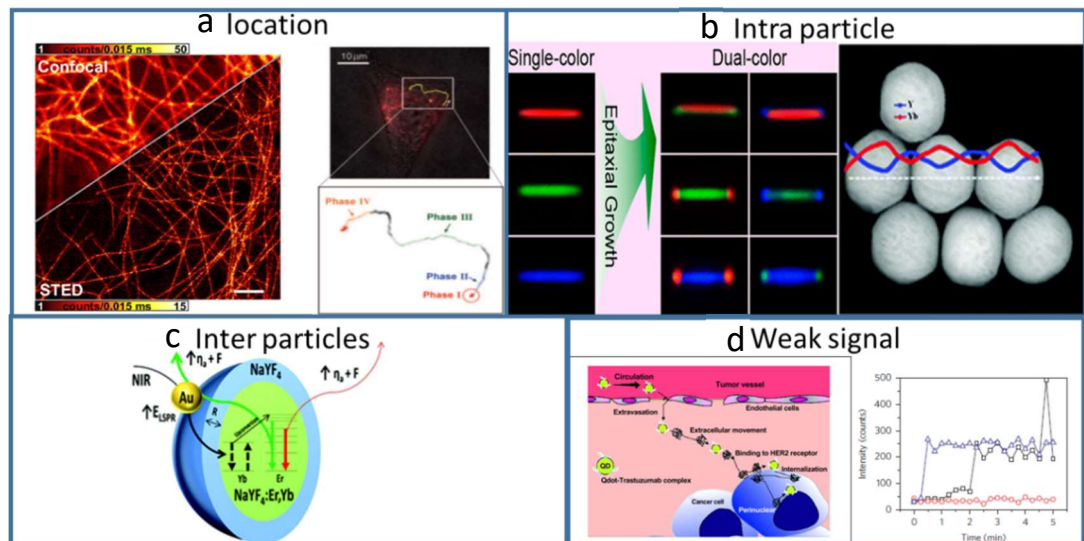
Figure 1.16 The significant benefits of single nanoparticle characterisation [62-68]. (a) is the enhanced location resolution and tracking ability with the help of single particle characterisation. (b) is the barcode and elemental mapping technology to characterise emission or element distribution within a particle. (c) is the interaction of a UCNP particle with gold nanoparticles. (d) is the detecting weak signal for a cancer cell from a quantum dots and from a UCNP.

1.2.2 Methods for single UCNP characterisation

1.2.2.1 TEM

TEM is a microscopy technique in which a beam of electrons transmits through a specimen (a thin section less than 100 nm thick) to form an image. TEM is a major analytical tool in the physical, chemical, and biological sciences. TEM measurement of UCNPs requires dropping UCNP solution onto a copper or carbon grid and then measurement can

be performed as normal. This technique primarily checks the size and morphology of single UCNP nanoparticles. Using imaging software, static data like size distribution can also be determined. However, this method cannot be applied to live biological samples such as living cells and animals.

1.2.2.2 Dynamic light scattering (DLS)

TEM is a common method for size measurements of nanoparticle in dried samples. Other methods are required for measuring size distribution in solution samples. DLS is a technique that can be used to measure the size distribution of nanoparticles in suspension. In DLS, a monochromatic light source, usually a laser, shines through a polariser into a sample. When the light hits small particles, the light scatters in all directions (Rayleigh scattering); the scattering intensity fluctuates over time. By analysing this time-related information, the size can be calculated.

1.2.2.3 X-ray diffraction

X-ray crystallography is a technique to measure the atomic and molecular structure of a crystal. The incident X-rays diffract into many directions due to the modulation of the crystal structure. By measuring the correlated angles and intensities, a picture of the density of electrons within the crystal can be constructed.

1.2.2.4 Zeta potential

Zeta potential, as shown in Figure 1.17, is the difference in potential between the dispersion medium and the stationary layer of fluid attached to the dispersed particle. The Zeta potential value is related to the electrical charge contained within the region near the slipping plane. It is

also related to the location of the plane. This technique is widely used to quantify charge magnitude. For UCNPs, it is used to measure the surface charge level and also to determine the trend of particle aggregation.
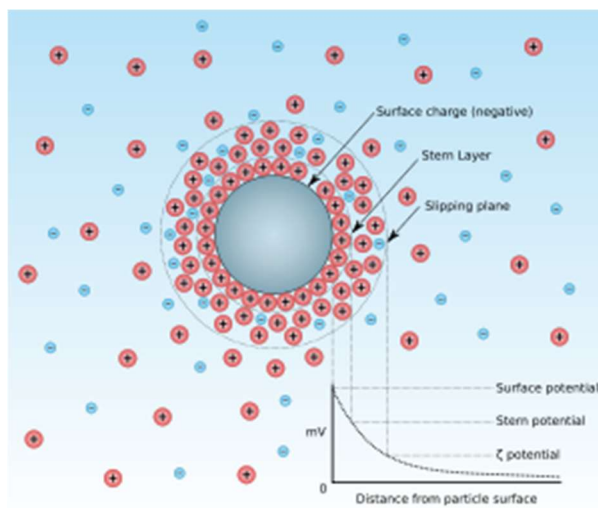
Figure 1.17 The ionic concentration and potential difference as a function of distance from the charged surface of a particle suspended in a dispersion medium [69].

1.2.2.5 Optical characterisation methods

Optical characterisation is essential for single UCNPs because UCNPs are mainly used as luminescence probes. Many useful properties can be studied by optical characterisation, including luminescence intensity, luminescence decay lifetime, luminescence rise time, luminescence spectrum, as well as polarisation or power dependent properties. To optically characterise UCNPs, the mainstream methods are confocal microscopy, fibre loaded systems, and optical tweezer systems.

1.2.2.5.1 Confocal microscopy

In a typical single UCNP confocal characterisation system (Figure1.18), a pair of pinholes are placed to reduce the light out of focus, which could help microscopy achieve higher resolution. A high numerical aperture

(NA) objective lens is used to focus the NIR laser (typically 980 nm or 800 nm) on the single UCNP. After passing through the pinhole, the signal is guided into a detector or spectrometer for analysis of useful parameters. In my thesis, the main characterisation system is based on confocal microscopy; I will introduce this system with more details in Chapter 2.
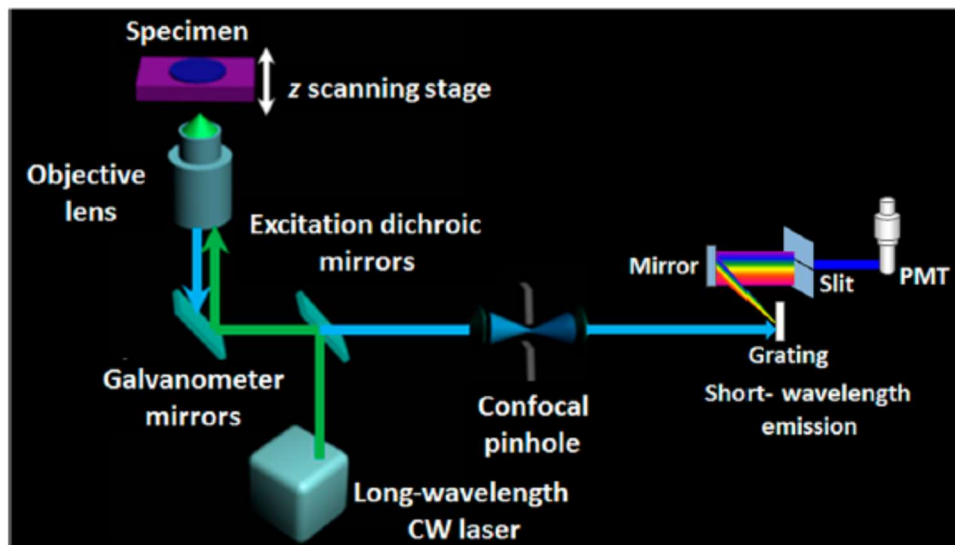
Figure 1.18 A typical confocal system [70].

1.2.2.5.2 Fibre-loaded single nanoparticle measurement system

Luminescence detection using liquid-immersed exposed-core microstructured optical fibres (MOF) has been proposed and applied by Monro et al. [71-73]. A schematic of the system is demonstrated in Figure 1.19. This system uses a suspended core to capture a single nanoparticle and then measure its luminescence. A 980 nm fibre-coupled diode laser is coupled into the MOF using a dichroic mirror and an objective lens. The emission of UCNPs is collected by the same fibre. Then, the emission propagates through the dichroic filter and a bandpass filter and is detected by a spectrometer.

The experimental procedure firstly involves optimising and recording the amount of power coupled into the suspended core of the fibre by varying the fibre position using XYZ stages. Then, with the tip of the fibre immersed in the nanoparticle solution, the nanoparticles are captured by the fibre. Here, the nanoparticle solution is diluted, and the UCNPs are dispersed in a nonpolar solvent, e.g., toluene, cyclohexane, etc., with a concentration ranging from tens of femto mol to tens of nano mol [74].
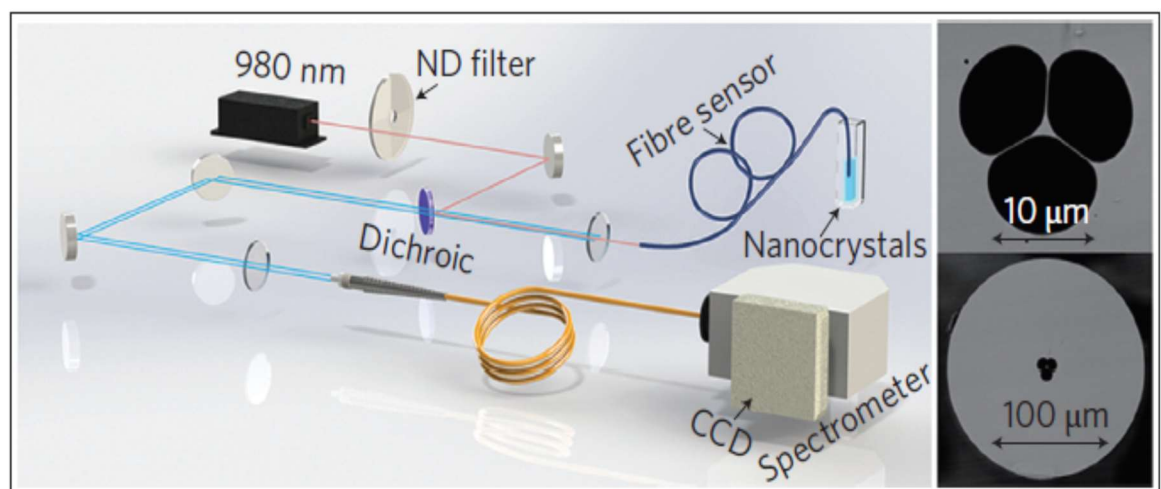
Figure 1.19 Schematic of the experimental configuration for capturing upconversion luminescence of nanoparticles using a suspended-core microstructure optical-fibre dip sensor [68].

1.2.2.5.3 Optical tweezer system

Optical tweezers use a highly focused laser beam to provide an attractive or repulsive force to trap several nanoparticles. The trapping force depends on the relative refractive index between the particles and the surrounding medium. The typical tweezer system is shown in Figure 1.20. Prof. Daniel Jaque's group from Universidad Autónoma de Madrid is the main research group using optical tweezers to investigate UCNPs. Optical tweezers are not only used to collect emission from nanoparticles, but can also collect the correlated shape and surface charge information through

monitoring the trapping mobility [60, 75, 76]. This technique also provides more opportunities for real-time applications in optical sensing due to the optical manipulation capability.
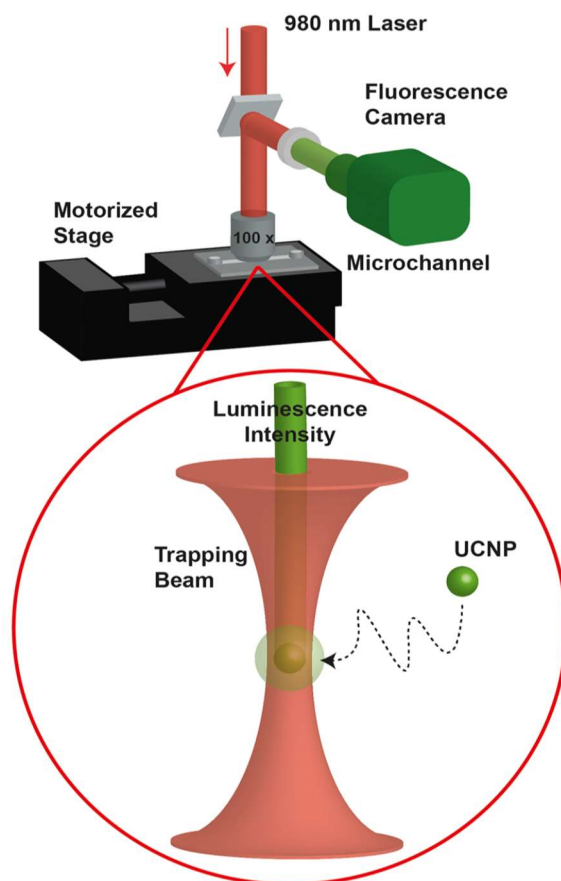
Figure 1.20 Schematic representation of an optically trapped UCNP [75].

1.2.3 Single UCNP optical characterisation and its applications

With the development of characterisation technology, the characterisation of UCNPs at the single nanoparticle level has been of great research interest owing to the resultant rich correlated information. This has resulted in the discovery of more useful specific spectroscopic properties, and thus, more applications have benefited from UCNPs. Here, I would like to introduce some important work performed by the pioneers of this field using single UCNP characterisation methods.

This section has two parts. In the first part, I will review the basic researches using single UCNP optical characterisation. In the second part, I will introduce practical applications of single particle characterisation.

1.2.3.1 Single UCNP optical characterisation

Single UCNP characterisation has been applied to characterise many properties that could not be precisely measured or even can not be measured before, such as intensity, polarisation, lifetime. Some outstanding works in this area are introduced below.

1.2.3.1.1 Single UCNP characterisation of particles with different dopping concentration

Concentration quenching is a severe problem which limits the intensity of UCNPs. In 2013, our group found that high excitation power can overcome the Tm^{3+} concentration quenching effect, and therefore, enhance luminescence intensity [68]. With the intensity improvement, we developed a system to remotely track single nanoparticles with a fibre dip system. Cohen, Schuck, and their colleagues studied highly Er^{3+} doped single nanoparticles [77] and also found the intensity enhancement phenomenon. Enhanced intensity was produced with high doping concentration and excitation intensity. The single particle luminescence images shown in Figure 1.21 with low, medium, and high laser intensity are a clear evidence of this concentration quenching abatement effect at high doping levels.

The single nanoparticle characterisation is essential for this research topic, because the intensity characterisation has to be done on the single nanoparticle. Otherwise, the intensity is not precise and also the excitation power intensity cannot be precisely controlled. Single nanoparticle

characterisation also helps to show the difference between particles with different concentrations as shown in figure 1.21 (b)-(d).
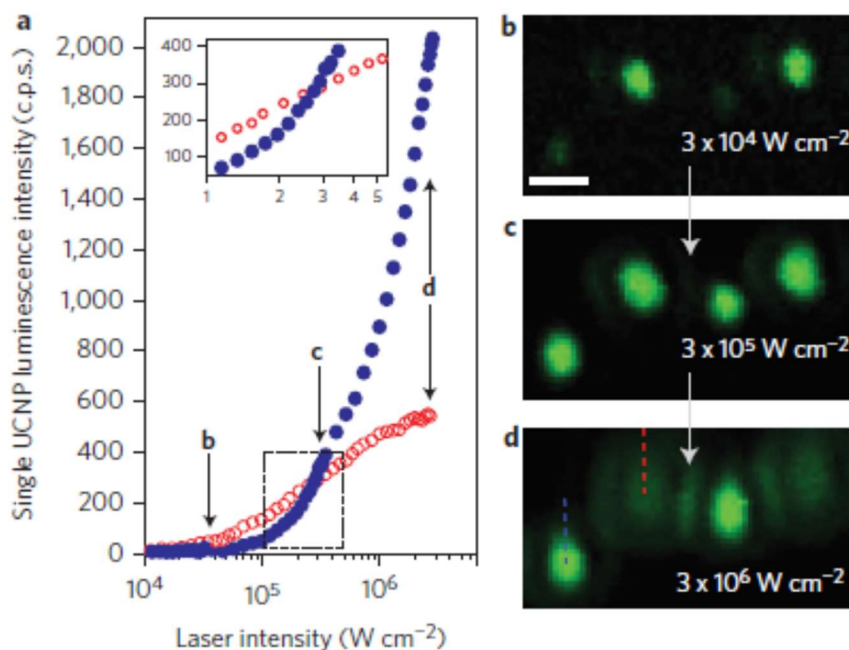
Figure 1.21 (a) Luminescence intensity of single 8 nm UCNPs with 20% (blue circles) and 2% (red circles) Er³⁺ dependent on excitation power density. (b)(c) and (d) are confocal luminescence images taken at points shown in (a) with different excitation power level. Dashed lines indicate regions from which luminescence intensity was collected for data in (a) [77].

1.2.3.1.2 Single UCNP characterisation for particles with different position

Another research benefited from single nanoparticle characterisation is surface plasmon research. Surface plasmon is known to enhance luminescence, but the mechanism underlying the enhancing process is still unclear. One important factor for enhancement that has been identified in research is the distance between the emitter and metal surface. And the single nanoparticle characterization could clearly research the effect of distance and that is why we need single nanoparticle characterization here.

Research has been carried out with UCNPs and gold nanospheres at the single nanoparticle level [78]. As Figure 1.22(a) shows, with the help of an Atomic Force Microscope (AFM) tip, a gold nanosphere was brought to the proximity of the UCNP with their central axes along the laser polarisation axis. The emission intensity was enhanced several times depending on the wavelength (Figure 1.22(b)). Similar research has also been performed with an AFM tip to locally enhance electric fields in the vicinity [79] (Figure 1.22(c, d)). These studies provide important tools for the optimum design of future hybrid UCNPs and metal nanostructures. Further detailed studies on the distance based research would help to understand the plasmon effects and apply them in to distance sensing or intensity enhancement.
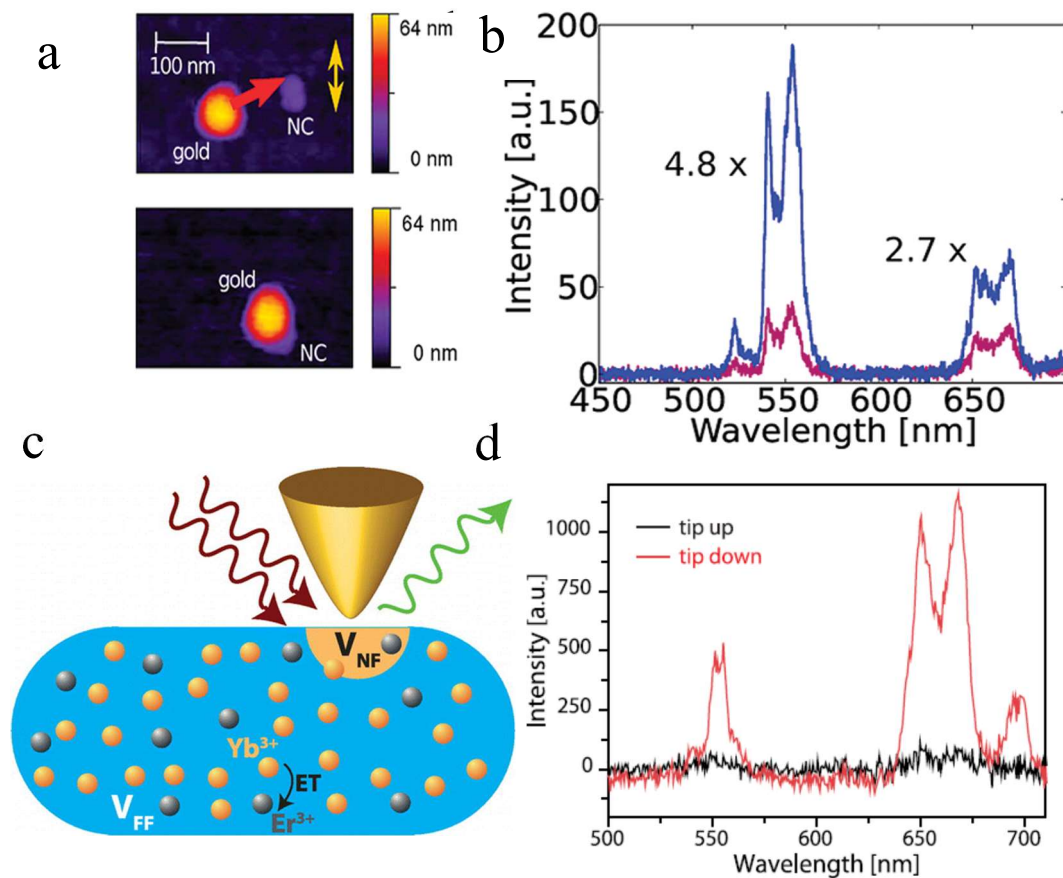
Figure 1.22 (a) A gold sphere was brought to the vicinity of a UCNP; the emission

intensity was enhanced with the enhanced local field by surface plasmon (b) [78]. The
tip was used to enhance the local electric field to improve intensity. (c) An illustration
of the experiment; (d) the enhanced intensity [79].

1.2.3.1.3 Single UCNP characterisation of particles with different doping distribution
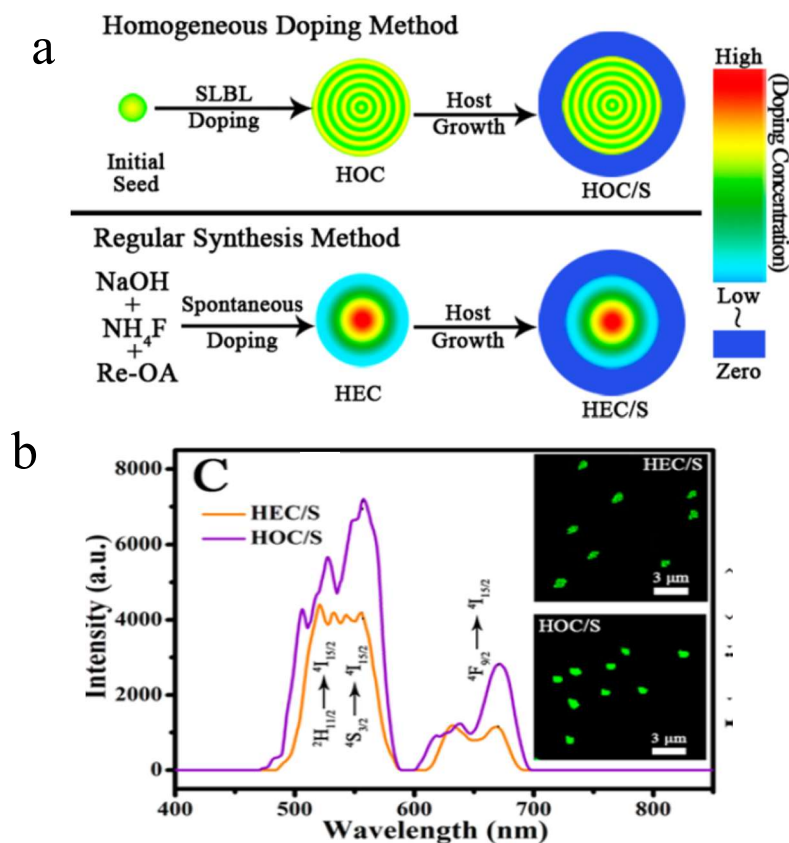
Figure 1.23 (a) Homogenous doping method (HOC/S) and regular doping method
(HEC/S). (b) Single nanoparticle spectrum of HOC/S and HEC/S particle which shows
the intensity enhancement of homogenous doping [80].

To date, studies of the doping concentration of lanthanide-doped UCNPs
are usually denoted by the reactant feed ratio in the experiment. Very little
attention has been paid to the dopant ion distribution at the single
nanoparticle level. This raises the question of whether the doping
elements are statistically distributed in the single nanoparticle and
whether changing the distribution can vary the luminescence property.

Profs. Zhang and Zhao fabricated UCNPs from a niche angle [80]. The influences of the spatial distributions and relative concentrations of the dopants on the optical properties of UCNPs were investigated for the first time at the single nanoparticle level (Figure 1.23). Based on the one-pot successive layer-by-layer (SLBL) method, homogenous doping particles were found to exhibit 20−30% improvement compared with normal heterogeneous doping particles.

1.2.3.1.4 Single UCNP characterisation of particles with hybrid structure

Hybrid UCNP nanomaterials are state-of-the-art materials due to the combined merits from the combination of multiple materials. Energy transfer can occur between interfaces. Due to the complicated nature of hybrid materials, intensity research must be performed at the single nanoparticle level to confirm the data. The UCNP hybrid with ZnO material has successfully undergone single nanoparticle characterisation and the intensity was characterised along the cross-section line [81]. With the help of single nanoparticle characterisation, the luminescence uniformity of the hybrid nanoparticles was confirmed and the double intensity enhancement was precisely measured (Figure 1.24). This hybrid material also possesses superior photoelectrochemical properties. This strategy provides an excellent approach to understand the versatile properties of lanthanide-doped UCNPs.
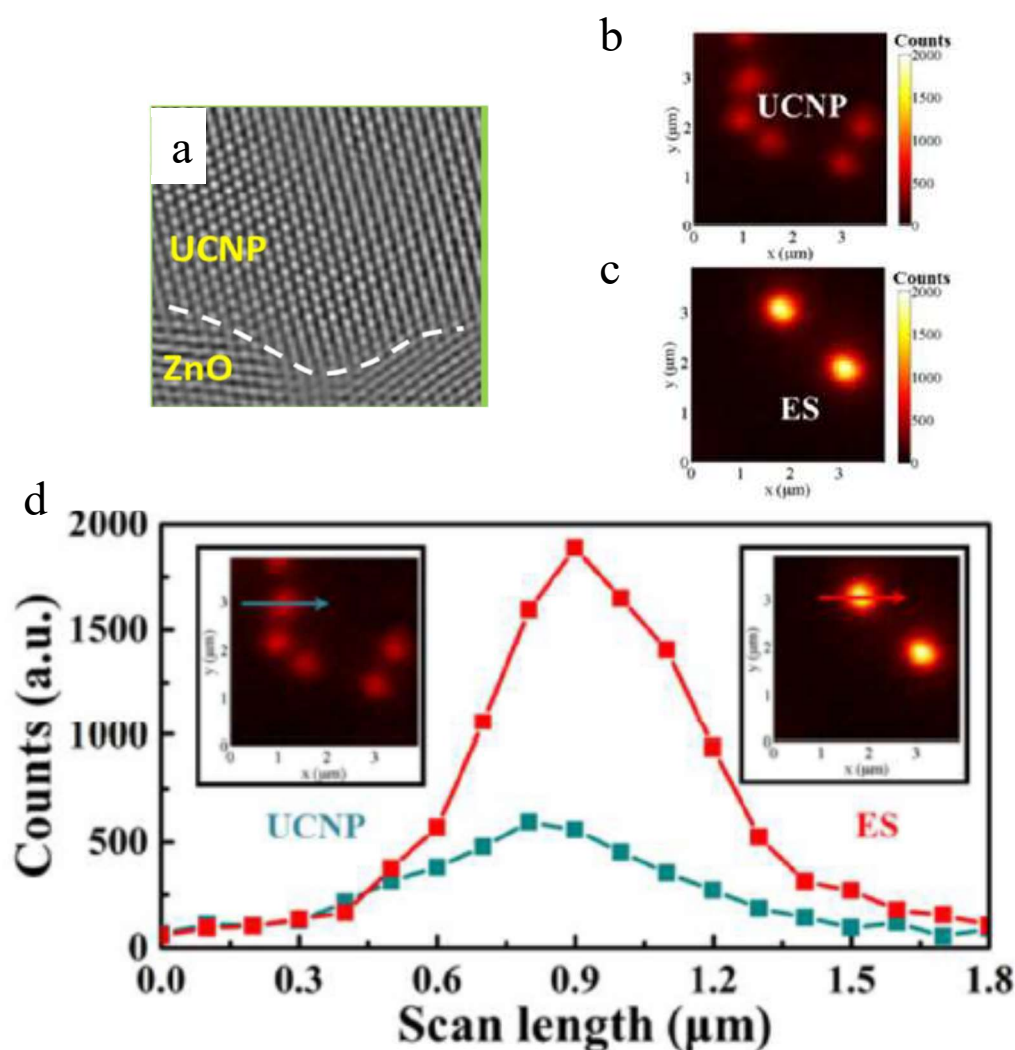
Figure 1.24 Characterisation of UCNP-ZnO hybrid nanoparticle. (a) Inverse FFT images from the local areas. The confocal microscopy quantitative measurement of (b) single NaYF₄: Yb, Tm@ZnO synthesised at 210ºC and (c) NaYF₄: Yb, Tm nanoparticles. (d) Comparison of single particle emission intensity for NaYF₄: Yb, Tm and NaYF₄: Yb, Tm@ZnO synthesised at 210ºC [81].

1.2.3.1.5 Single UCNP characterisation of polarisation

Single particle luminescence polarisation has been widely studied in semiconductor systems. The emission peaks of UCNPs are much narrower than semiconductor materials. The polarisation of a UCNP will be particularly useful for accurate interpretation in the event of

overlapping emission spectra, allowing detailed analysis such as sensing and super resolution analyses to be carried out.

Single UCNP polarisation has been studied by Prof. Qiu's group. They found that intra-ion transition orientations and crystal local symmetry dominates polarisation anisotropy [82]. With further study, they found that the polarisation of UC luminescence depends upon the orientation of the nanodisk with respect to the polarisation angle of the excitation light [83] (Figure 1.25). This phenomenon was also reported in several other studies [76, 84].

Because the orientation of single nanoparticles is random in samples, single nanoparticle characterisation is essential for polarisation research. Such UCNP polarisation research paves the way for polarisation related to multiplexing and bioimaging research of UCNPs.
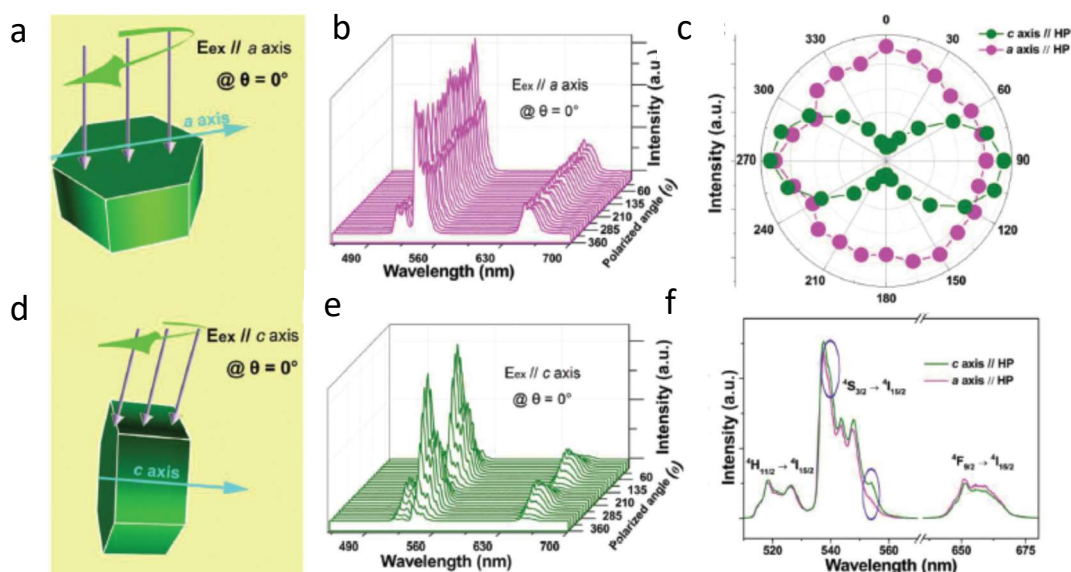
Figure 1.25 Schematic representation of the NaYF₄ nanodisk with its a axis (a) and c axis (d) parallel to the horizontal plane (HP). UC luminescence spectra of a single nanodisk, with a axis (b) and c axis parallel (e) to excitation polarisation, recorded at excitation polarisation angles varying from 0° to 360°, with no polariser placed in the detection part. (c) Polar plots of the integrated UC luminescence intensity as a function of excitation polarisation angle for the transition from $^4S_{3/2} \rightarrow ^4I_{15/2}$ of Er^{3+} recorded at two different configurations of the single nanodisk. (f) Comparison of UC luminescence spectra of a single nanodisk with its c and a axes parallel to HP [83].

1.2.3.1.6 Single UCNP characterisation of spectrum profile

Using precise single particle spectral investigations, microscopic electron behaviour and energy transfer mechanisms can be exploited. This is important for intrinsic improvement of UCNPs. Gargas and colleagues investigated the single nanoparticle spectrum [77](Figure 1.26(a)) and observed particle-to-particle variations in the peak intensity of single UCNP spectra. The observed spectral differences may arise from variation in lanthanide distributions, surface defects, surface reconstruction, and/or faceting [77]. Rodríguez-Sevilla and colleagues found spectra differences between single nanoparticles and multiparticles, as shown in Figure

1.26(b). They proposed that the difference is due to the UCNP−UCNP interaction processes [60].
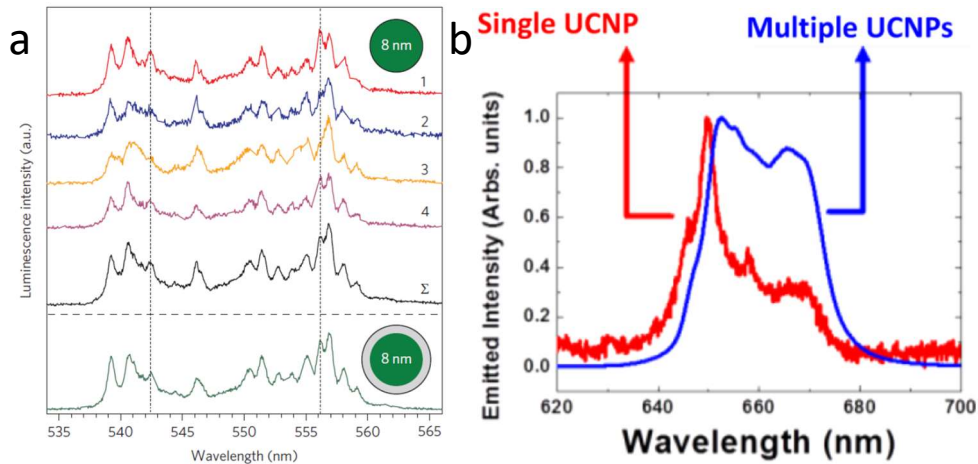
Figure 1.26 (a) Fine spectra of the green emission bands collected from four single 8 nm UCNPs (curves 1–4) and their averaged spectra (curve Σ). The green emission spectrum of an 8 nm UC nanoparticle with epitaxial 1.8 nm undoped shell is shown below the horizontal dashed line [77]. (b) Upconversion emission spectra as obtained from a single UCNP (red) and from multiple UCNPs (blue). Data were obtained from a single optically tweezer trapped UCNP and from a colloidal suspension [60].

1.2.3.1.7 Single UCNP characterisation of lifetime

The narrow emission bands of UCNPs enable multi-colour channel multiplexing. Furthermore, as shown in Figure 1.27, with precise characterisation of single UCNPs, their lifetime as well as their variation levels can be given. In the upper part of Figure 1.27, it shows high doping concentration UCNPs have a short lifetime, and vice versa low doping concentration UCNPs have a long lifetime. With this principle, in the lower part, the UCNPs with lifetime ranging from 48.6 μs to 668.8 μs have been fabricated and tested. This research enables lifetime of UCNPs as a dimension to be applied to produce multiplexing [85]
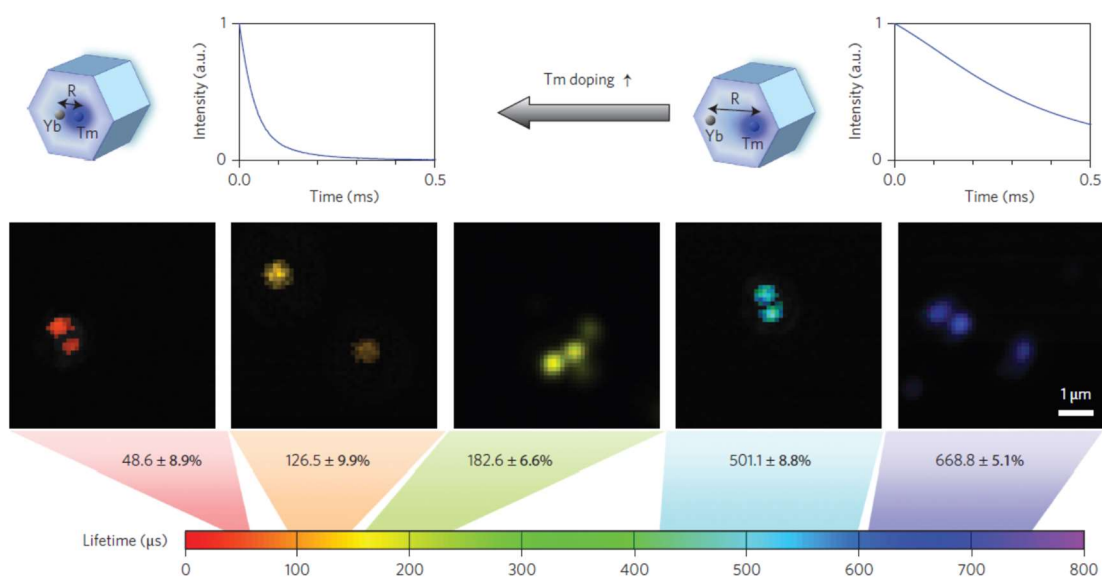
Figure 1.27 Lifetime tuning scheme and time-resolved confocal images for NaYF$_4$: Yb, Tm upconversion nanocrystals [85].

In conclusion, the researches of single UCNP has been applied on broad research areas, including the intensity, lifetime, polarisation, spectrum, distance, doping concentration, and hybrid structure of single nanoparticles. At this stage, the researches of increasing the intensity of UCNPs are still quite hot, such as plasmon enhanced and dye sensitised methods. These characterisations provide promising opportunities for further development of UCNPs in versatile applications.

1.2.3.2 Applications at the single nanoparticle level

As discussed above, single nanoparticle characterisation has been applied to characterise many properties that could not be measured or could not be precisely measured before. With these property characterisations, many applications are now feasible.

1.2.3.2.1 Single nanoparticle characterisation for bioimaging applications

UCNPs are of immense interest for microscopy because of their excellent imaging quality without a luminescence background. Single characterisation of UCNPs makes single nanoparticle imaging possible. With a known single particle intensity, we can identify single nanoparticles and design specific experiments to research their intercellular activities (Figure 1.28). The current research in this field is mainly in cellular investigations, and the cellular uptake and stability research is the top issues researchers are focusing.
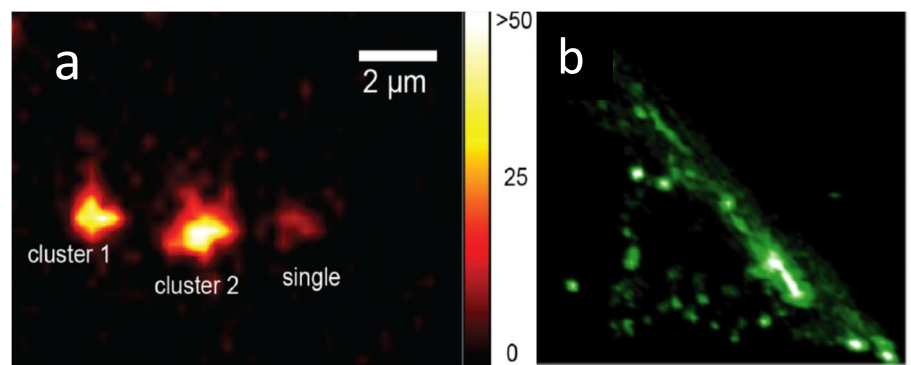
Figure 1.28 (a) Epi luminescence microscopy image of the UCNP constellation, imaged using the blood-immersion objective [61]. (b) Live-cell imaging of UCNPs in NIH 3T3 murine fibroblasts using 980 nm excitation [17]. The single UCNP is clearly observable, although blurred.

1.2.3.2.2 Single nanoparticle characterisation for super resolution applications

Super resolution is a new technique developed in the past 20 years. With the help of super resolution technologies, scientists can observe biological activities under the diffraction limit (200 nm). UCNPs have excellent imaging properties. The combination of super resolution and UCNP benefits will enable frontier development in this field. The reported feasible solution to achieve this is the Stimulated Emission Depletion (STED) method where excitation is achieved with an orange 609 nm laser

and a doughnut-shaped 532 nm beam is exploited as a second excitation step. After that, the remaining population of $^1D_2$ state can be read out by a short 532 nm pulse. This achieves ~50 nm resolution [86] (Figure 1.29).

Nonetheless, the super resolution technique is still complicated and the resolution needs to be improved. More detailed characterisation of UCNPs together with smart experimental design is required. Our research group first reported the UCNP enabled super resolution with 28nm resolution[87]. Prof. He and Prof. Zhan also reported super resolution phenomenon with UCNPs[87, 88]. These current progress shows promising of UCNPs to be applied in super resolution field, especially with deep tissure imaging potential.
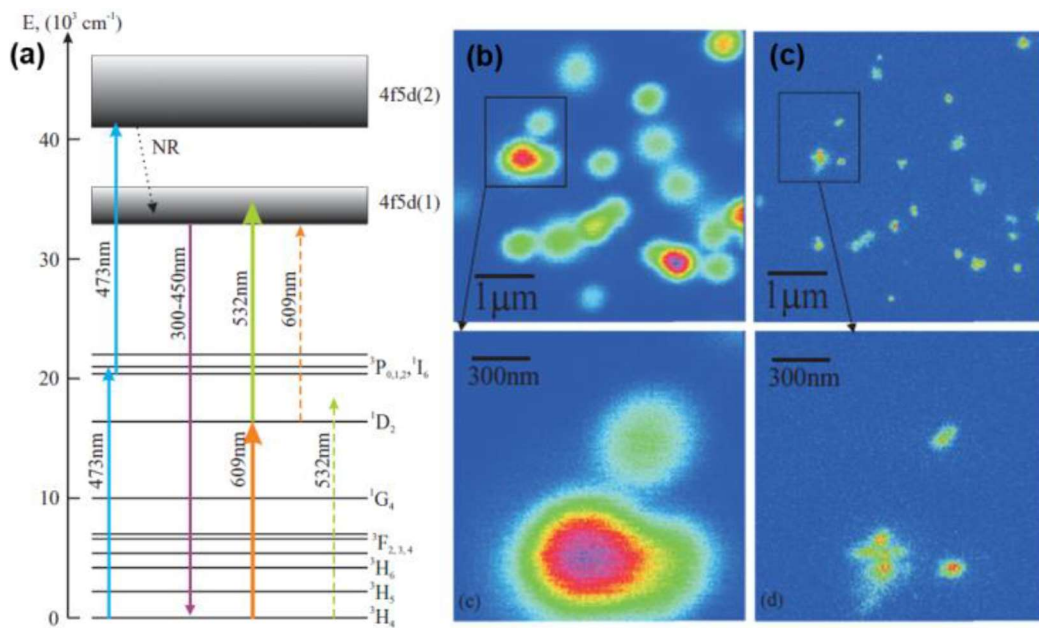
Figure 1.29 (a) Energy level diagram of Pr^{3+} electronic states in YAG crystal. (b) Confocal image of Pr^{3+}: YAG nanoparticles. (c) Super-resolution image of the same area [86].

1.2.3.2.3 Single nanoparticle characterisation for particle tracking

Long-term 3D tracking of nanoparticles and their intracellular motions have advanced our understanding of endocytosis and exocytosis and of active transport processes. UCNPs, with their non-bleaching and non-blinking properties, are among the best probes for long-term tracking studies. With single UCNP nanoparticle tracking, scientists can conduct detailed research on biological technologies, as shown in Figure 1.30[63]. From the following figure, researchers could watch the movement of the particles with camera. Then by analysing their movement, the activity of the UCNP could be seperated into four phases. With rotation, three dimesion imaging has been obtained in a live cell (Figure 1.30 (b)) [89].
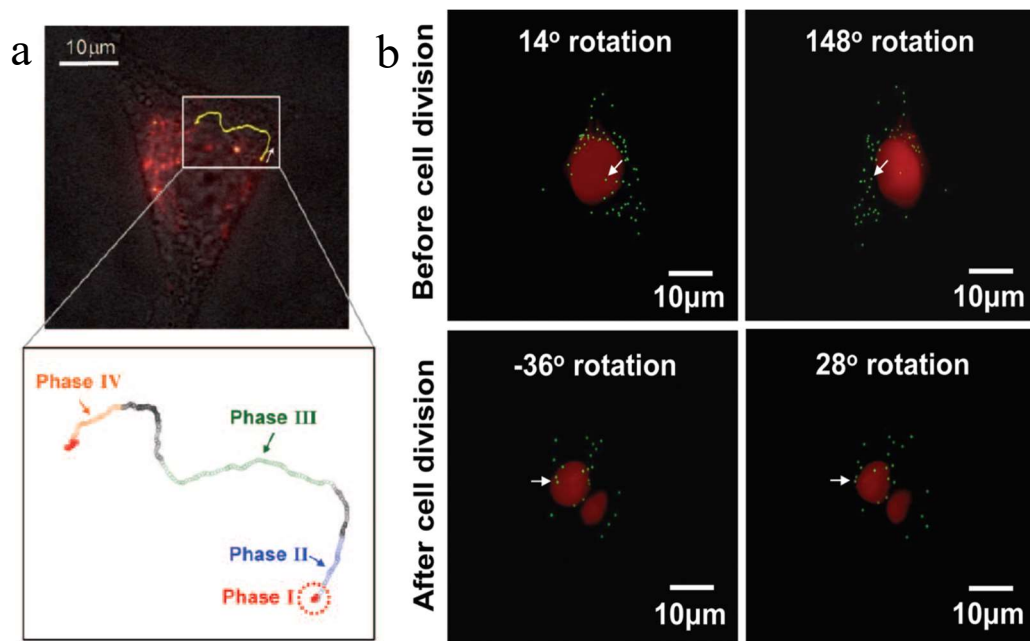
Figure 1.30 (a) Trajectory of a vesicle containing UCNPs transported from the cell periphery to the perinuclear region presumably by dyneins [63]. (b) Three-dimensional live-cell imaging with lanthanide-doped upconverting nanoparticles [89].

This research in figure 1.30 (a), is the first work tracking single UCNP movement. Later researchers from our group made the tracking possible with naked eye tracking and introduced excitation power density as a new

multiplexing dimension[90]. In the future, lower excitation tracking is the trend and tracking correlated medical research would be very interesting.

1.2.3.2.4 Single nanoparticle characterisation for biological detection

With the development of single UCNP characterisation, weak signals, as low as one nanoparticle, can be detected [68, 91] (Figure 1.31). This could enable super sensitive detection technologies such as early cancer detection. At this stage, there is not many researches using single nanoparticle characterization as a detection method due to the available sensitivity of measurement system, but this is a trend when the researches become more precise and the UCNP become more powerful.
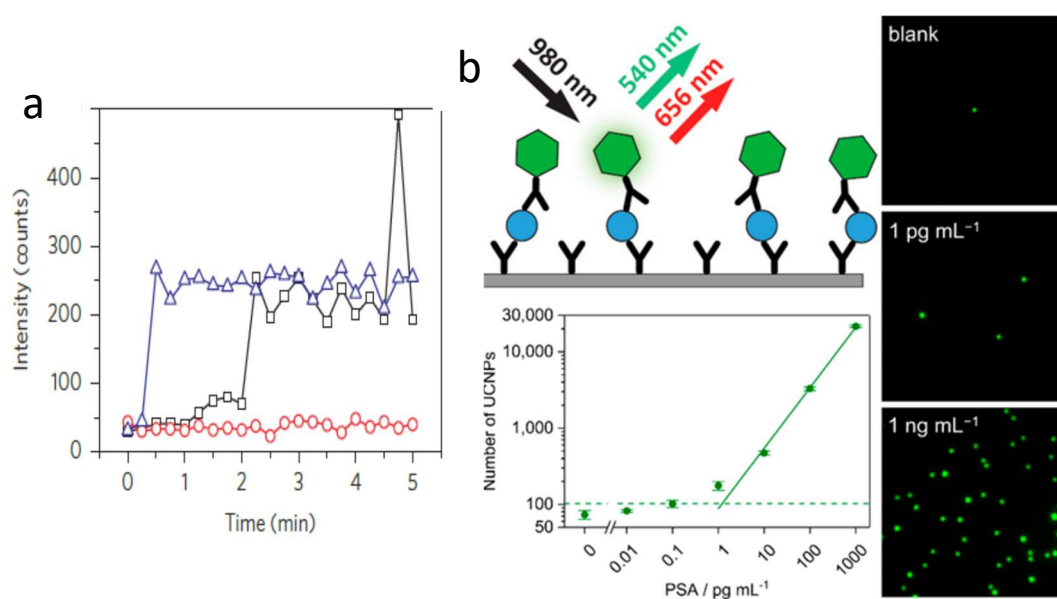
Figure 1.31 (a) Time-dependent dynamics of three independent trials detecting a single nanoparticle [68]. (b) The single-molecule (digital) upconversion-linked immunosorbent assay (ULISA) reaches a limit of detection of 1.2 pg mL−1 (42 fM) prostate specific antigen (PSA) in 25% blood serum [92].

1.2.3.2.5 Single nanoparticle characterisation for 3D display

3D display is an essential technology of the future. As lanthanide ions have a wide range of luminescence wavelengths, lanthanide materials have been widely used in display technology. 3D display technology requires single nanoparticle scanning to enhance resolution. Thus, characterisation at the single nanoparticle level is necessary. As shown in Figure 1.32, Prof. Liu and his colleagues were the first to achieve 3D display [59]. This is achieved by using colour tunable UCNP and laser scanning.

The 3D display research using UCNP is quite rare at this present, this is because of the long lifetime and the weak intensity of the lanthanide ions. How to find a way to solve the lifetime and intensity problem to increase the scanning speed is quite essential for the next step.
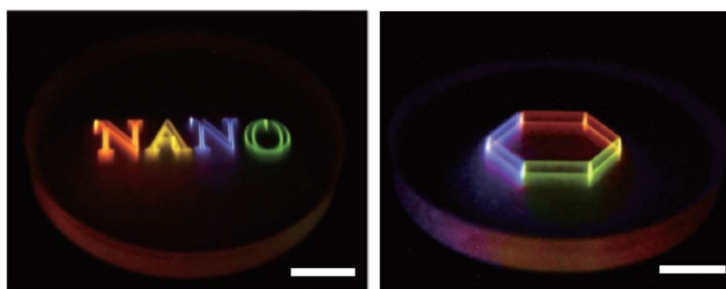
Figure 1.32 The true image generated through the use of multilayer upconversion nanocrystals [59].

1.2.3.2.6 Single nanoparticle characterisation for anti-counterfeit technologies

UCNP materials have been used for anti-counterfeiting technology due to its coding ability. To enhance the security, the next step is to move this technology to the single nanoparticle level.

As shown in Figure 1.33, a single nanoparticle barcode has been used in anti-counterfeit applications [64]. In this figure it can be seen that the

emission spectra of these two S patterns are nearly identical. However, on a microscopic level, single nanoparticles are clearly distinguishable under high magnification [56].

In the future, UCNPs with more specific coding ability will be developed such as colour coding, lifetime coding, or even polarisation coding. The anti-counterfeit technology using single UCNP will be further developed for high value items need high level of anti-counterfeit.
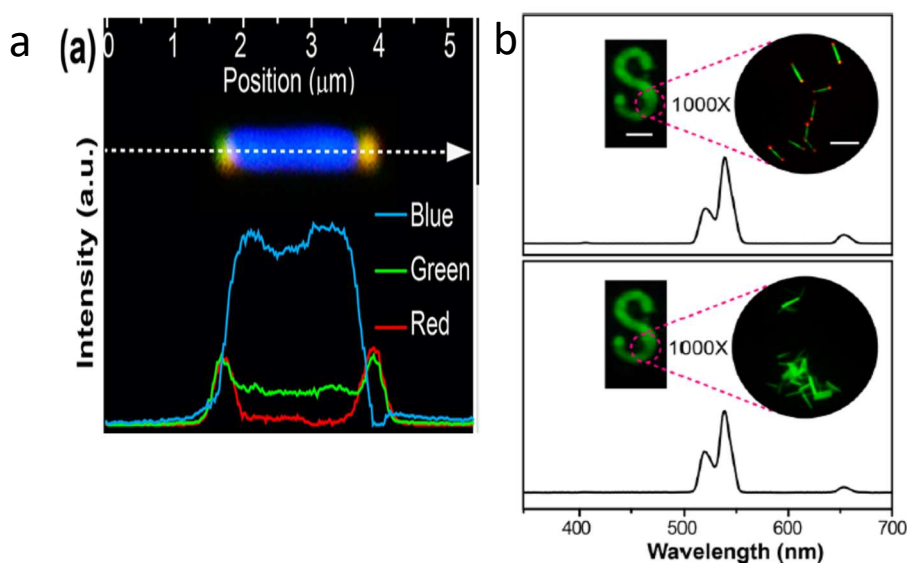
Figure 1.33 (a) is the emission colour distribution of the barcode particle (b)is the luminescence image of a stamped letter S generated with dual-colour microrods and control sample [64].

1.3 Objectives and Outline

In the above introduction, the significance of single UCNP characterisation has been illustrated by its benefits in multiple applications. However, there are still a lot of work to do. First, there remains a lack of efficient single particle characterisation methods for UCNPs. The current characterisation systems are not sensitive enough to fully characterization the properties of single UCNP, especially the

lifetime and spectrum. Second, the core-shell structure has been widely used in UCNPs, but the details have not been researched, such as the thickness, and the energy transfer principle. Third, besides the researches of the UCNP itself, there is a need to research the interaction of the UCNP with the optical device, which would open the door to UCNP nanoscale device.

 In this thesis, I will provide the details to build a single UCNP characterisation system and will describe my research based on this system. This thesis will not only describe the results of my studies during my PhD, but will also provide future researchers and students with a guidebook for UCNPs and UCNP-related research topics.

In Chapter 1, I have introduced UCNPs and have discussed upconversion luminescence mechanisms, synthesis methods, advantages, and applications. Secondly, I have introduced single nanoparticle characterisation, including its significance and methods. Finally, I have shown the applications of single UCNP optical characterisation.

In Chapter 2, I will introduce how to build a single nanoparticle system, how to operate it, and the applications of the system. This chapter consists of the background knowledge in material science and optical engineering that is required for the development of the system.

In Chapter 3, I will research the optimal shell thickness with the help of the single UCNP spectrum measuring system. The results describe the energy transfer process inside UCNPs with different shell thicknesses.

In Chapter 4, I will combine UCNPs with a mirror to construct a nanoscale interferometer to research the self-interference phenomenon of UCNPs.

Then, I will apply the experimental and simulation results to achieve 3D super resolution location.

In Chapter 5, I will give conclusions and perspectives of my research.

References

1.   Zheng W., Huang P., Tu D., et al., *Lanthanide-doped upconversion nano-bioprobes: electronic structures, optical properties, and biodetection.* Chemical Society Reviews, 2015. **44**(6): p. 1379-1415.

2.   Su Q., Han S., Xie X., et al., *The effect of surface coating on energy migration-mediated upconversion.* Journal of the American Chemical Society, 2012. **134**(51): p. 20849-20857.

3.   Wang F., Deng R., Wang J., et al., *Tuning upconversion through energy migration in core–shell nanoparticles.* Nature Materials, 2011. **10**(12): p. 968-973.

4.   Wang F., Han Y., Lim C.S., et al., *Simultaneous phase and size control of upconversion nanocrystals through lanthanide doping.* nature, 2010. **463**(7284): p. 1061.

5.   Chen C., Li C., and Shi Z., *Current advances in lanthanide‐doped upconversion nanostructures for detection and bioapplication.* Advanced Science, 2016. **3**(10): p. 1600029.

6.   Lu J., Chen Y., Liu D., et al., *One-step protein conjugation to upconversion nanoparticles.* Analytical chemistry, 2015. **87**(20): p. 10406-10413.

7.   Li Z., Zhang Y., and Jiang S., *Multicolor core/shell‐structured upconversion fluorescent nanoparticles.* Advanced Materials, 2008. **20**(24): p. 4765-4769.

8.   Wang F., Deng R., and Liu X., *Preparation of core-shell NaGdF$_4$ nanoparticles doped with luminescent lanthanide ions to be used as upconversion-based probes.* Nature protocols, 2014. **9**(7): p. 1634.

9.   Shen B., Gao Y., Liu Q., et al., *A facile strategy for the synthesis of a NaREF$_4$-gold nanocomposite as a dual-modal bioimaging agent.* RSC Advances, 2017. **7**(35): p. 21625-21629.

10.   Hemmer E., Venkatachalam N., Hyodo H., et al., *Upconverting and NIR emitting rare earth based nanostructures for NIR-bioimaging.* Nanoscale, 2013. **5**(23): p. 11339-11361.

11.   Smith A.M., Mancini M.C., and Nie S., *Bioimaging: second window for in vivo imaging.* Nature nanotechnology, 2009. **4**(11): p. 710.

12.   Hemmer E., Benayas A., Légaré F., et al., *Exploiting the biological windows: current perspectives on fluorescent bioprobes emitting above 1000 nm.* Nanoscale Horizons, 2016. **1**(3): p. 168-184.

13.   Punjabi A., Wu X., Tokatli-Apollon A., et al., *Amplifying the red-emission of upconverting nanoparticles for biocompatible clinically used prodrug-induced photodynamic therapy.* ACS nano, 2014. **8**(10): p. 10621-10630.

14.   Yeow E.K., Melnikov S.M., Bell T.D., et al., *Characterizing the fluorescence intermittency and photobleaching kinetics of dye molecules immobilized on a glass surface.* The Journal of Physical Chemistry A, 2006. **110**(5): p. 1726-1734.

15.   Schuster J., Cichos F., and Von Borczyskowski C., *Blinking of single molecules in various environments.* Optics and spectroscopy, 2005. **98**(5): p. 712-717.

16.   Huang Z., Ji D., Xia A., et al., *Direct observation of delayed fluorescence from a remarkable back-isomerization in Cy5.* Journal of the American Chemical Society, 2005. **127**(22): p. 8064-8066.

17.   Wu S., Han G., Milliron D.J., et al., *Non-blinking and photostable upconverted luminescence from single lanthanide-doped nanocrystals.* Proceedings of the National Academy of Sciences, 2009. **106**(27): p. 10917-10921.

18.   Wang F. and Liu X., *Upconversion multicolor fine-tuning: visible to near-infrared emission from lanthanide-doped NaYF₄ nanoparticles.* Journal of the American Chemical Society, 2008. **130**(17): p. 5642-5643.

19.   Sun Y., Feng W., Yang P., et al., *The biosafety of lanthanide upconversion nanomaterials.* Chemical Society Reviews, 2015. **44**(6): p. 1509-1525.

20.   Tanenbaum Marvin E., Gilbert Luke A., Qi Lei S., et al., *A protein-tagging system for signal amplification in gene expression and fluorescence imaging.* Cell, 2014. **159**(3): p. 635-646.

21.   Juette M.F., Terry D.S., Wasserman M.R., et al., *The bright future of single-molecule fluorescence imaging.* Current Opinion in Chemical Biology, 2014. **20**: p. 103-111.

22.   Maldonado C.R., Salassa L., Gomez-Blanco N., et al., *Nano-functionalization of metal complexes for molecular imaging and anticancer therapy.* Coordination Chemistry Reviews, 2013. **257**(19): p. 2668-2688.

23. Jin Z. and Hildebrandt N., *Semiconductor quantum dots for in vitro diagnostics and cellular imaging.* Trends in Biotechnology, 2012. **30**(7): p. 394-403.

24. Zhao Y., Shi L., Fang J., et al., *Bio-nanoplatforms based on carbon dots conjugating with F-substituted nano-hydroxyapatite for cellular imaging.* Nanoscale, 2015. **7**(47): p. 20033-20041.

25. Achilefu S., *Introduction to concepts and strategies for molecular imaging.* 2010, ACS Publications.

26. Kostiv U., Kotelnikov I., Proks V., et al., *RGDS- and TAT-conjugated upconversion of NaYF4:Yb^{3+}/Er^{3+}&SiO$_2$ nanoparticles: in vitro human epithelioid cervix carcinoma cellular uptake, imaging, and targeting.* ACS Applied Materials & Interfaces, 2016. **8**(31): p. 20422-20431.

27. Cui Z., Bu W., Fan W., et al., *Sensitive imaging and effective capture of Cu^{2+}: Towards highly efficient theranostics of Alzheimer's disease.* Biomaterials, 2016. **104**: p. 158-167.

28. Xue Z., Yi Z., Li X., et al., *Upconversion optical/magnetic resonance imaging-guided small tumor detection and in vivo tri-modal bioimaging based on high-performance luminescent nanorods.* Biomaterials, 2017. **115**: p. 90-103.

29. Sun L., Ge X., Liu J., et al., *Multifunctional nanomesoporous materials with upconversion (in vivo) and downconversion (in vitro) luminescence imaging based on mesoporous capping UCNPs and linking lanthanide complexes.* Nanoscale, 2014. **6**(21): p. 13242-13252.

30. Zhou J., Zhu X., Chen M., et al., *Water-stable NaLuF$_4$-based upconversion nanophosphors with long-term validity for multimodal lymphatic imaging.* Biomaterials, 2012. **33**(26): p. 6201-6210.

31. Sun L., Wei R., Feng J., et al., *Tailored lanthanide-doped upconversion nanoparticles and their promising bioapplication prospects.* Coordination Chemistry Reviews, 2018. **364**: p. 10-32.

32. Rao L., Bu L.L., Cai B., et al., *Cancer cell membrane‑coated upconversion nanoprobes for highly specific tumor imaging.* Advanced Materials, 2016. **28**(18): p. 3460-3466.

33. Cheng L., Yang K., Li Y., et al., *Multifunctional nanoparticles for upconversion luminescence/MR multimodal imaging and magnetically targeted photothermal therapy.* Biomaterials, 2012. **33**(7): p. 2215-2222.

34.   Xing H., Bu W., Zhang S., et al., *Multifunctional nanoprobes for upconversion fluorescence, MR and CT trimodal imaging.* Biomaterials, 2012. **33**(4): p. 1079-1089.

35.   He S., Johnson N.J., Nguyen Huu V.A., et al., *Simultaneous enhancement of photoluminescence, MRI relaxivity, and CT contrast by tuning the interfacial layer of lanthanide heteroepitaxial nanoparticles.* Nano letters, 2017. **17**(8): p. 4873-4880.

36.   Sun Y., Yu M., Liang S., et al., *Fluorine-18 labeled rare-earth nanoparticles for positron emission tomography (PET) imaging of sentinel lymph node.* Biomaterials, 2011. **32**(11): p. 2999-3007.

37.   Yang Y., Sun Y., Cao T., et al., *Hydrothermal synthesis of NaLuF$_4$: 153Sm, Yb, Tm nanoparticles and their application in dual-modality upconversion luminescence and SPECT bioimaging.* Biomaterials, 2013. **34**(3): p. 774-783.

38.   Wang Y. and Kohane D.S., *External triggering and triggered targeting strategies for drug delivery.* Nature Reviews Materials, 2017. **2**(6): p. 17020.

39.   Liu B., Chen Y., Li C., et al., *Poly (Acrylic Acid) modification of Nd^{3+}‐sensitized upconversion nanophosphors for highly efficient UCL imaging and pH‐responsive drug delivery.* Advanced Functional Materials, 2015. **25**(29): p. 4717-4729.

40.   Wang Y., Song S., Liu J., et al., *Zno‐functionalized upconverting nanotheranostic agent: multi‐modality imaging‐guided chemotherapy with on‐demand drug release triggered by pH.* Angewandte Chemie International Edition, 2015. **54**(2): p. 536-540.

41.   Li H., Wei R., Yan G.-H., et al., *Smart self-assembled nanosystem based on water-soluble pillararene and rare-earth-doped upconversion nanoparticles for ph-responsive drug delivery.* ACS Applied Materials & Interfaces, 2018. **10**(5): p. 4910-4920.

42.   Liu J., Bu W., Pan L., et al., *NIR‐triggered anticancer drug delivery by upconverting nanoparticles with integrated azobenzene‐modified mesoporous silica.* Angewandte Chemie, 2013. **125**(16): p. 4471-4475.

43.   Min Y., Li J., Liu F., et al., *Near‐infrared light‐mediated photoactivation of a platinum antitumor prodrug and simultaneous cellular apoptosis imaging*

by upconversion‑luminescent nanoparticles. Angewandte Chemie International Edition, 2014. **53**(4): p. 1012-1016.

44. Xu J., Xu L., Wang C., et al., *Near-infrared-triggered photodynamic therapy with multitasking upconversion nanoparticles in combination with checkpoint blockade for immunotherapy of colorectal cancer.* ACS nano, 2017. **11**(5): p. 4463-4474.

45. Zhang X., Yang P., Dai Y., et al., *Multifunctional up‑converting nanocomposites with smart polymer brushes gated mesopores for cell imaging and thermo/pH dual‑responsive drug controlled release.* Advanced Functional Materials, 2013. **23**(33): p. 4067-4078.

46. Li X., Zhou L., Wei Y., et al., *Anisotropic growth-induced synthesis of dual-compartment Janus mesoporous silica nanoparticles for bimodal triggered drugs delivery.* Journal of the American Chemical Society, 2014. **136**(42): p. 15086-15092.

47. Ge X., Sun L., Ma B., et al., *Simultaneous realization of Hg^{2+} sensing, magnetic resonance imaging and upconversion luminescence in vitro and in vivo bioimaging based on hollow mesoporous silica coated UCNPs and ruthenium complex.* Nanoscale, 2015. **7**(33): p. 13877-13887.

48. McGrew S.P., *Anticounterfeiting method and device utilizing holograms and pseudorandom dot patterns.* 1995, Google Patents.

49. Yushun Y., Xiangming H., and Quanrong Z., *Breakthrough in fake prevention. Nuclear track-etching.* Physics, 1999. **28**: p. 295-298.

50. Darshan G., Premkumar H., Nagabhushana H., et al., *Blue light emitting ceramic nano-pigments of Tm^{3+} doped $YAlO_3$: Applications in latent finger print, anti-counterfeiting and porcelain stoneware.* Dyes and Pigments, 2016. **131**: p. 268-281.

51. Kumar P., Singh S., and Gupta B.K., *Future prospects of luminescent nanomaterial based security inks: from synthesis to anti-counterfeiting applications.* Nanoscale, 2016. **8**(30): p. 14297-14340.

52. Tan H., Xie S., Xu J., et al., *Branched $NaYF_4$: Yb, Er up-conversion phosphors with luminescent properties for anti-counterfeiting application.* Science of Advanced Materials, 2017. **9**(12): p. 2223-2233.

53.   Da Luz L.L., Milani R., Felix J.F., et al., *Inkjet printing of lanthanide–organic frameworks for anti-counterfeiting applications.* ACS Applied Materials & Interfaces, 2015. **7**(49): p. 27115-27123.

54.   You M., Zhong J., Hong Y., et al., *Inkjet printing of upconversion nanoparticles for anti-counterfeit applications.* Nanoscale, 2015. **7**(10): p. 4423-4431.

55.   Meruga J.M., Baride A., Cross W., et al., *Red-green-blue printing using luminescence-upconversion inks.* Journal of Materials Chemistry C, 2014. **2**(12): p. 2221-2227.

56.   You M., Lin M., Wang S., et al., *Three-dimensional quick response code based on inkjet printing of upconversion fluorescent nanoparticles for drug anti-counterfeiting.* Nanoscale, 2016. **8**(19): p. 10096-10104.

57.   Su W., Zheng M., Li L., et al., *Directly coat TiO$_2$ on hydrophobic NaYF$_4$:Yb, Tm nanoplates and regulate their photocatalytic activities with the core size.* Journal of Materials Chemistry A, 2014. **2**(33): p. 13486-13491.

58.   Chen X., Xu W., Zhang L., et al., *Large upconversion enhancement in the "Islands" Au–Ag Alloy/NaYF$_4$: Yb^{3+}, Tm^{3+}/Er^{3+} composite films, and fingerprint identification.* Advanced Functional Materials, 2015. **25**(34): p. 5462-5471.

59.   Deng R., Qin F., Chen R., et al., *Temporal full-colour tuning through non-steady-state upconversion.* Nature nanotechnology, 2015. **10**(3): p. 237.

60.   Rodríguez-Sevilla P., Rodríguez-Rodríguez H., Pedroni M., et al., *Assessing single upconverting nanoparticle luminescence by optical tweezers.* Nano letters, 2015. **15**(8): p. 5068-5074.

61.   Nadort A., Sreenivasan V.K., Song Z., et al., *Quantitative imaging of single upconversion nanoparticles in biological tissue.* PloS one, 2013. **8**(5): p. e63292.

62.   Hein B., Willig K.I., and Hell S.W., *Stimulated emission depletion (STED) nanoscopy of a fluorescent protein-labeled organelle inside a living cell.* Proceedings of the National Academy of Sciences, 2008. **105**(38): p. 14271-14276.

63.   Nam S.H., Bae Y.M., Park Y.I., et al., *Long‑term real‑time tracking of lanthanide ion doped upconverting nanoparticles in living cells.* Angewandte Chemie, 2011. **123**(27): p. 6217-6221.

64.   Zhang Y., Zhang L., Deng R., et al., *Multicolor barcoding in a single upconversion crystal.* Journal of the American Chemical Society, 2014. **136**(13): p. 4893-4896.

65.   Xu X., Clarke C., Ma C., et al., *Depth-profiling of Yb^{3+} sensitizer ions in $NaYF_4$ upconversion nanoparticles.* Nanoscale, 2017. **9**(23): p. 7719-7726.

66.   Clarke C., Liu D., Wang F., et al., *Large-scale dewetting assembly of gold nanoparticles for plasmonic enhanced upconversion nanoparticles.* Nanoscale, 2018. **10**(14): p. 6270-6276.

67.   Tada H., Higuchi H., Wanatabe T.M., et al., *In vivo real-time tracking of single quantum dots conjugated with monoclonal anti-HER2 antibody in tumors of mice.* Cancer research, 2007. **67**(3): p. 1138-1144.

68.   Zhao J., Jin D., Schartner E.P., et al., *Single-nanocrystal sensitivity achieved by enhanced upconversion luminescence.* Nature nanotechnology, 2013. **8**(10): p. 729.

69.   contributors W. *Zeta potential*. 2019; Available from: https://en.wikipedia.org/wiki/Zeta_potential.

70.   Yu M., Li F., Chen Z., et al., *Laser scanning up-conversion luminescence microscopy for imaging cells labeled with rare-earth nanophosphors.* Analytical chemistry, 2009. **81**(3): p. 930-935.

71.   Warren-Smith S. and Monro T., *Theoretical study of liquid-immersed exposed-core microstructured optical fibers for sensing.* Optics express, 2008. **16**(12): p. 9034-9045.

72.   Afshar S., Ruan Y., Warren-Smith S.C., et al., *Enhanced fluorescence sensing using microstructured optical fibers: a comparison of forward and backward collection modes.* Optics letters, 2008. **33**(13): p. 1473-1475.

73.   Ruan Y., Schartner E.P., Ebendorff-Heidepriem H., et al., *Detection of quantum-dot labeled proteins using soft glass microstructured optical fibers.* Optics express, 2007. **15**(26): p. 17819-17826.

74.   Zhou J., Xu S., Zhang J., et al., *Upconversion luminescence behavior of single nanoparticles.* Nanoscale, 2015. **7**(37): p. 15026-15036.

75.   Rodríguez-Sevilla P., Prorok K., Bednarkiewicz A., et al., *Optical forces at the nanoscale: size and electrostatic effects.* Nano letters, 2018. **18**(1): p. 602-609.

76.   Rodríguez-Sevilla P., Labrador-Páez L., Wawrzyńczyk D., et al., *Determining the 3D orientation of optically trapped upconverting nanorods by in situ single-particle polarized spectroscopy.* Nanoscale, 2016. **8**(1): p. 300-308.

77.   Gargas D.J., Chan E.M., Ostrowski A.D., et al., *Engineering bright sub-10-nm upconverting nanocrystals for single-molecule imaging.* Nature nanotechnology, 2014. **9**(4): p. 300.

78.   Schietinger S., Aichele T., Wang H.-Q., et al., *Plasmon-enhanced upconversion in single $NaYF_4$: Yb^{3+}/Er^{3+} codoped nanocrystals.* Nano letters, 2009. **10**(1): p. 134-138.

79.   Mauser N., Piatkowski D., Mancabelli T., et al., *Tip enhancement of upconversion photoluminescence from rare earth ion doped nanocrystals.* ACS nano, 2015. **9**(4): p. 3617-3626.

80.   Li X., Wang R., Zhang F., et al., *Engineering homogeneous doping in single nanoparticle to enhance upconversion efficiency.* Nano letters, 2014. **14**(6): p. 3634-3639.

81.   Wang L., Ren L., Mitchell D., et al., *Enhanced energy transfer in heterogeneous nanocrystals for near infrared upconversion photocurrent generation.* Nanoscale, 2017. **9**(47): p. 18661-18667.

82.   Zhou J., Chen G., Wu E., et al., *Ultrasensitive polarized up-conversion of $Tm^{3+}-Yb^{3+}$ doped β-$NaYF_4$ single nanorod.* Nano letters, 2013. **13**(5): p. 2241-2246.

83.   Chen P., Song M., Wu E., et al., *Polarization modulated upconversion luminescence: single particle vs. few-particle aggregates.* Nanoscale, 2015. **7**(15): p. 6462-6466.

84.   Green K.K., Wirth J., and Lim S.F., *Nanoplasmonic upconverting nanoparticles as orientation sensors for single particle microscopy.* Scientific reports, 2017. **7**(1): p. 762.

85.   Lu Y., Zhao J., Zhang R., et al., *Tunable lifetime multiplexing using luminescent nanocrystals.* Nature Photonics, 2014. **8**(1): p. 32.

86.   Kolesov R., Reuter R., Xia K., et al., *Super-resolution upconversion microscopy of praseodymium-doped yttrium aluminum garnet nanoparticles.* Physical Review B, 2011. **84**(15): p. 153413.

87.   Liu Y., Lu Y., Yang X., et al., *Amplified stimulated emission in upconversion nanoparticles for super-resolution nanoscopy.* nature, 2017. **543**(7644): p. 229.

88.   Zhan Q., Liu H., Wang B., et al., *Achieving high-efficiency emission depletion nanoscopy by employing cross relaxation in upconversion nanoparticles.* Nature communications, 2017. **8**(1): p. 1058.

89.   LiáJo H., HanáSong Y., and TaekáLee K., *Fast and background-free three-dimensional (3D) live-cell imaging with lanthanide-doped upconverting nanoparticles.* Nanoscale, 2015. **7**(46): p. 19397-19402.

90.   Wang F., Wen S., He H., et al., *Microscopic inspection and tracking of single upconversion nanoparticles in living cells.* Light: Science & Applications, 2018. **7**(4): p. 18007.

91.   Haro-Gonzalez P., Del Rosal B., Maestro L., et al., *Optical trapping of NaYF4: Er^{3+}, Yb^{3+} upconverting fluorescent nanoparticles.* Nanoscale, 2013. **5**(24): p. 12192-12199.

92.   Farka Z., Mickert M.J., Hlavacek A., et al., *Single molecule upconversion-linked immunosorbent assay with extended dynamic range for the sensitive detection of diagnostic biomarkers.* Analytical chemistry, 2017. **89**(21): p. 11825-11830.

Chapter 2. Single upconversion nanoparticle optical characterisation system (SNCS)

As introduced in Chapter 1, there are three kinds of systems developed for single UCNP characterisation: the confocal system, the fibre-loaded system, and the optical tweezer system. Among them, the confocal system is the most commonly used one. One reason for this is that the confocal system is easily accessible. Another reason is that the confocal system has the capacity for the addition of extra components to the system. Thus, it can easily be further developed. In this thesis, I will use confocal microscopy as the basis for my characterisation system.

In this chapter, I will first introduce the theory behind confocal microscopy. Then I will describe how I built SNCS. Following this, I will explain how to operate this SNCS and apply this system to several important research topics relevant to single UCNP characterisation.
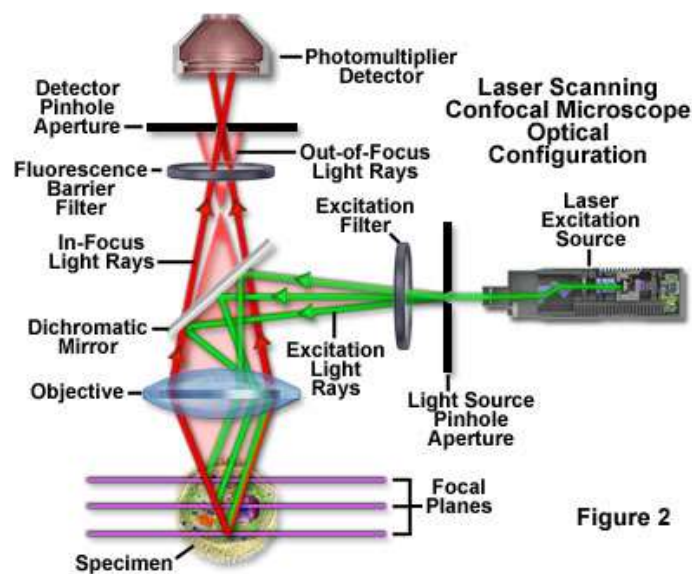
2.1 Confocal microscopy

Figure 2.1 Fluorescence confocal microscopes [1].

Confocal microscopy is an optical imaging technique for increasing optical resolution and contrast of a microscope using spatial pinholes to block out-of-focus light in image formation. The position of the pinholes is at the "phase conjugate" focal plane of the point light source (Figure 2.1). This is where the term "confocal" comes.

The confocal theory was first described by Marvin Minsky in the mid-1950s. However, due to a lack of intense light sources and the limited ability of computers to handle large amounts of data, its development was limited. From the 1990s, advances in computer and laser technology, coupled with new algorithms for digital manipulation of images, led to significant progress in confocal microscopy.

The working principle of confocal microscopy is shown in Figure 2.1. The coherent laser as an excitation source passes through a pinhole aperture and is then collimated with lenses and focused with an objective lens into a focal spot. The luminescence of the specimen passes through the objective lens and then through the dichroic mirror. The second pinhole is here on the focal plane of the lens. The camera or point detector collects the image at the image plane. The two pinhole positions and the focal plane of the sample are on the same focal phase. The signal from outside of the focal plane will be filtered out by the pinhole. The collected intensity from the point detector will be data from one point of the sample. By scanning the whole sample plane, the software is able to reconstruct the confocal image.

The fluorescence from above or below the focal plane of the specimen will form an extended airy disk in the aperture plane. The size of the pinhole on the aperture plane is precisely designed just to let the emission

of the focal plane pass through; the extended aspect in airy disks will be blocked out (Figure 2.1). This is called the "optical section".

Confocal microscopy provides several advantages over conventional widefield optical microscopy. First, it is able to serially produce thin (0.5 to 1.5 micrometre) optical sections through thick fluorescent specimens. The second advantage is the improved contrast and definition due to the reduction in background fluorescence. The third advantage is that the confocal optical sectioning technique is non-invasive, which enables the examination of both living and fixed specimens under a variety of conditions, with enhanced clarity [1].

2.2 The built SNCS

2.2.1 Main configuration of the SNCS

The system we built is called an SNCS. As shown in Figure 2.2, the main configuration is easy to understand. The details of the SNCS are provided below.

We use Fiber-Bragg-Grating (FBG) stabilised 976 nm laser diode, coupled with single-mode and polarisation-maintaining fibre coupling. An 842 long pass (LP) filter is placed in front of the laser collimator to remove the other laser wavelength and ensure the laser we used is pure. Then, the collimated laser beam is magnified with a 4f system. The beam size out of the collimator is required to be as large as the size of the back aperture of the objective lens in order to use the maximum effective numerical aperture and resultant optical resolution. Then, the 976 nm laser passes through into an objective lens.

The objective lens used in SNCS is Olympus UPLSAPO100X. It is a super apochromat objectives lens which could fully compensate for both

spherical and chromatic aberrations from the visible to the near-infrared region. Further, this objective lens also provides flat-field corrections.

The luminescence from UCNPs passes through the 842 nm short pass (SP) dichroic filter. Then, a filter wheel with 475±25 nm, 543±11 nm, 650±6 nm, and 800±25 nm bandpass filters is applied to obtain the emission bands of interest (other bandpass filters are also available too).

Next, a flip mirror switches the signal to either a CCD camera (Nikon, DS-2Mv) to obtain an image or to a fibre which is connected with a single photon avalanche detector (SPAD) (Excelitas, SPCM-AQRH-14-FC) to obtain an intensity value. This fibre has a core size of 50 μm and works as a confocal pinhole with 1.01 airy disk. Aside from the single photon counter, the fibre can also be connected to a spectrometer and the single photon counter can be used as a detector for the spectrometer.
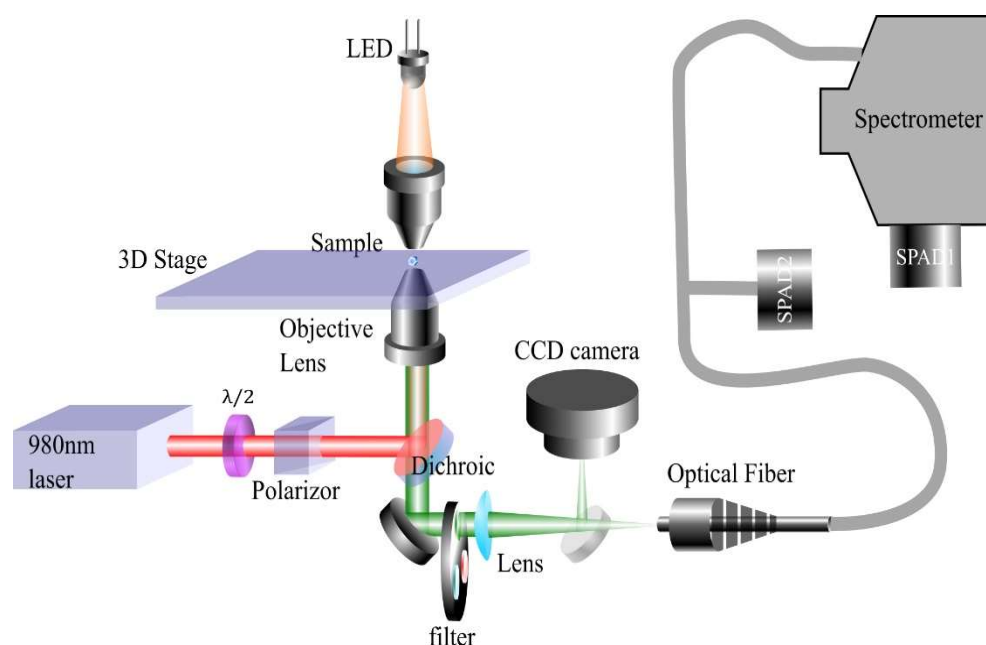

Figure 2.2 Single upconversion nanoparticle characterisation system (SNCS) [2].

2.2.2 Wide-field imaging module

To research samples with a large area of interest, we need a large field of view (FOV). For our SNCS system, the original excitation laser spot is about one μm. To expand the area, we designed a wide-field imaging module.

For the standard 4f system, the laser is focused on the focal plane of the objective lens, as shown in Figure 2.3. By inserting a thin lens (defocusing lens) at the phase conjugate plane of the back aperture of the objective lens, the laser's focusing position will be shifted, as shown in Figure 2.3. This position shift results in an expended Gaussian beam on the focal plane of the objective lens. Different focal lengths of the defocus lens will result in different spot sizes on the focal plane. For 200 mm, 150 mm, and 100 mm focal lengths of the defocusing lens, the radiuses of the Gaussian beam spots are 5.2 μm, 5.72 μm, and 6.9 μm, respectively. The excitation intensity at the centre of the beam can be estimated from the emission counts from UCNPs under defocused beam excitation.
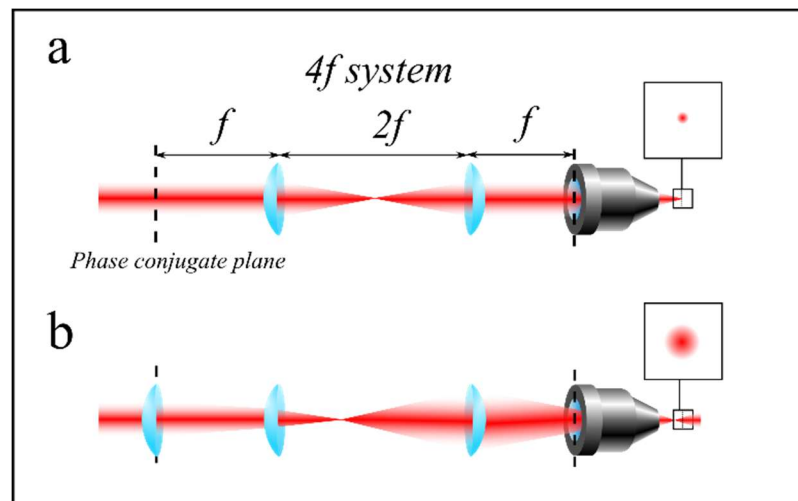
Figure 2.3 Schematic diagram of expanded laser spot for wide field imaging. (a) 4f system in the excitation beam path. (b) By inserting a defocusing lens at the phase conjugate plane of the back aperture of objective lens, the input laser beam can be defocused to a larger excitation spot. By changing the defocusing lens, the size of the large excitation spot can be controlled.
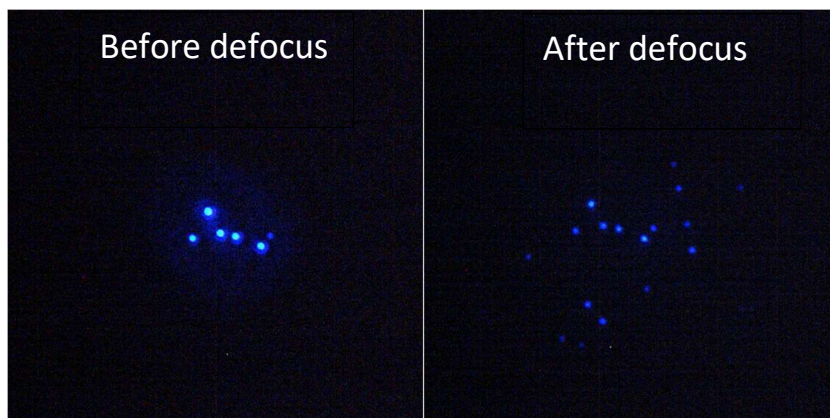
Figure 2.4 Image of UCNPs before and after defocus.

2.2.3 Precise excitation power change unit

The luminescence of UCNPs is strongly power dependent, not only on the intensity of luminescence but also the lifetime luminescence, and perhaps other parameters too. Thus, research on this power dependence is required. The traditional way to research power dependence is to manually change the excitation power and measure multiple power levels to plot the figure. This is time-consuming and the result is not precise. Therefore, development of a convenient tool is crucial. Here, we apply the polarisation principle to obtain the precise power over a large range.
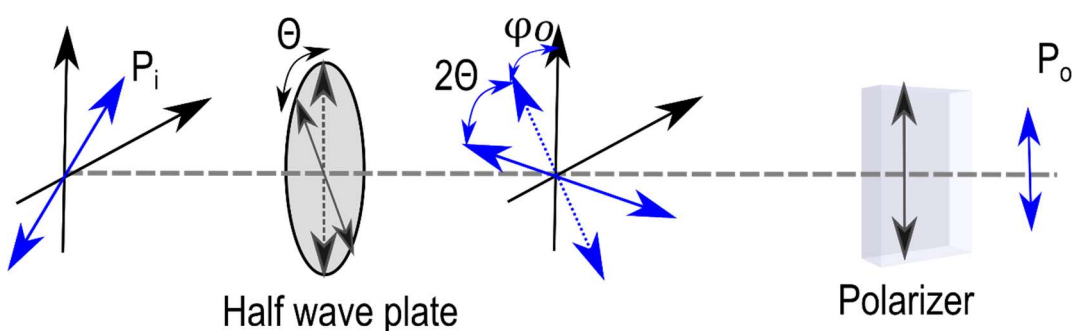
Figure 2.5 The working principle of the power change unit

As shown in Figure 2.5 the laser passing through the half-wave plate will change the polarisation by 2θ degrees with a θ degree rotation of the half wave plate. Then, the power transmitted by the polariser will obey the rule:

$$P_o = P_i \cos\varphi$$

Here, P_o is the output power from the polariser and P_i is the input power of the polariser; φ is the angle of the polariser and laser which pass through the half wave plate. $\varphi = \varphi_o + 2\theta$. Here, φ_o is the initial angle of the polariser and laser passed half wave plate.

Therefore, rotating the half wave plate will change φ and the output laser power will be changed correspondingly. With the help of a Neutral Density (ND) filter with a suitable attenuation ratio, we can expand the power range to 0.001-700 mW. This power range is equal to an optical density range from 10^2 to 10^8 W/cm^2.

2.2.4 Stage scanning

To scan the sample, we need to either move the sample to scan it or move the objective lens. Compared with moving the objective lens, moving the sample is more easier and the setup remains more stable. Here we used a piezo stage to move the sample to scan it.

A Thorlabs 3-axis NanoMax flexure stages (MAX311D) is used in our system. This stage has a built-in piezo stage. The scanning travel range is 20 nm and the theoretical resolution is 5 nm.

2.2.5 System calibration

The first part of the calibration processes for this SNCS is beam spot calibration. This is an examination of the collimation for the excitation part of SNCS. The laser beam which is linear polarised transfers through the objective lens and is reflected by the glass slide. The dichroic mirror could reflect most of the laser. However, there will still be a small portion that will go through the dichroic mirror and arrive at the CCD camera to

form a laser spot image. And when we do not need this laser spot, an 842 SP filter could be placed in the front of the camera to filter out the laser.

The spot image has a cross in the middle, as shown in Figure 2.6 left. This is caused by the polarisation selection of the dichroic mirror. The morphology of this spot also shows whether the incident laser is straight. Thus, if some part of the spot is brighter (Figure 2.6, right), the optical mirror should be aligned in the pathway to make it symmetric.
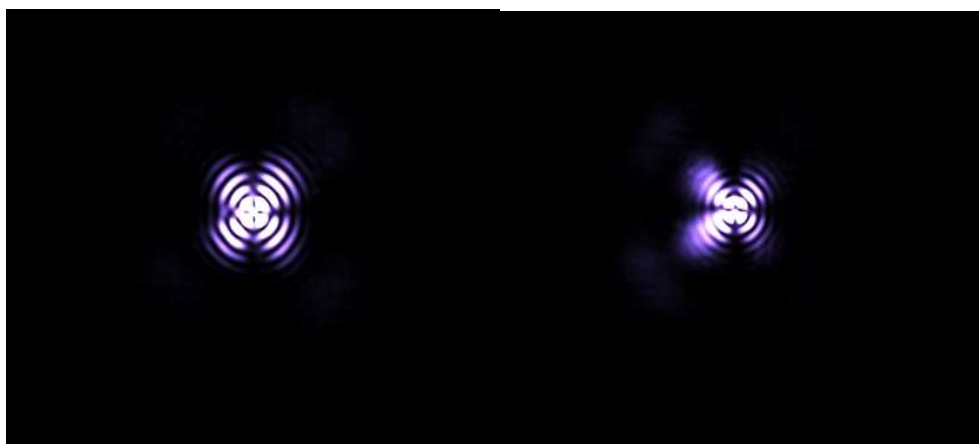
Figure 2.6 The correct laser spot in the SNCS (left) and the unsymmetrical laser spot in the SNCS (right).

The second part of the calibration process is the intensity calibration. With an aligned excitation laser, the intensity of the collected emission mostly depends on the fibre coupling efficiency of the signals focused by the tube lens. An XYZ translation stage was built to hold the fibre holder.

To align the fibre with the focused signal we first used a bright light source to align coarsely. The axis of focused bright light could be fixed in parallel with one line of the bench table, which is easy with the help of a cage system. Then, the XYZ stage is fixed on the bench with fibre parallel with the focused light axis. By moving the XYZ axis, the fibre is coarsely aligned with the focused light. After that, the bright light source is

exchanged with the UCNP cluster sample and then with the single particle sample to precisely align the fibre. Finally, one sample can be selected as a calibration sample and its intensity is used as a standard for the SNCS system.

It is important to note that the cleanliness of the filters, lens, and mirrors can impact the intensity the system detected. It should also be noted the direction of the lens and filters should be placed correctly. Usually, there is an arrow placed by manufacturers indicating the direction of the light propagation.

The third part of the system calibration process is piezo position calibration. This is because the piezo stage movement may not be precise. To calibrate this, we used a micro ruler from Thorlabs. The ruler is placed in the sample holder and the piezo voltage value is changed to move the ruler by 10 um (Figure 2.7). The voltage that is obtained will be the corresponding voltage for 10 um. This ratio can be used in our software program for scanning.
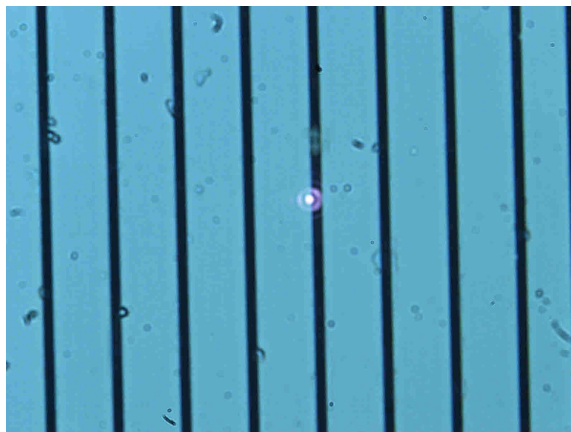
Figure 2.7 The piezo position calibration method.

The fourth calibration process is the excitation laser power calibration. The power change unit can change excitation power, but it still requires

calibration to enable the program. A power metre can be positioned close to the laser output near the objective lens. Then, the rotation angle can be calibrated to the power collected using software shown below in Figure 2.8. This correlation data table is the traceback table used for the power change program.
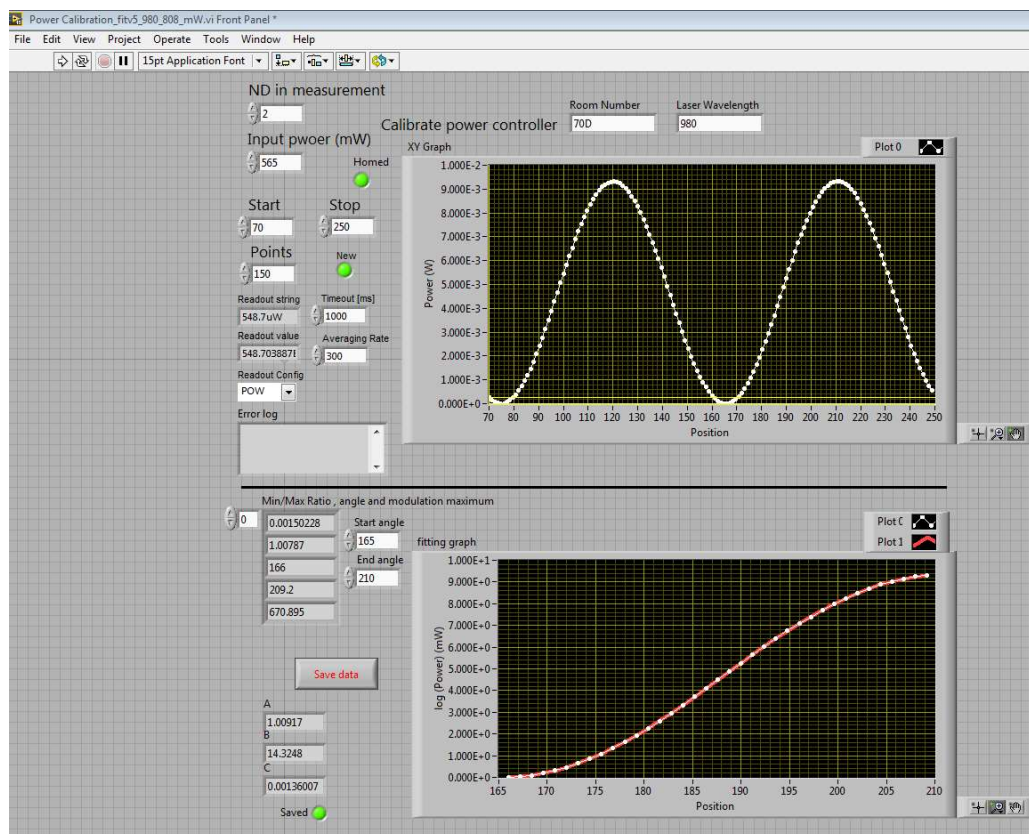
Figure 2.8 The excitation laser power calibration software.

2.3 Operation of the SNCS

2.3.1 Preparation of a single nanoparticle sample

The preparation of a single nanoparticle sample is very important and can be tricky to achieve. We tried many methods and finally were able to successfully make it quite easy and applicable.

The easiest method for preparation of a uniformly dispersed UCNP glass slide sample is described here. First, the glass slide must be cleaned with

ethanol and left to dry. Second, the synthesised hydrophobic solution is diluted to the concentration of 0.01 mg/ml. Third, 10 µl of diluted UCNP solution is dropped onto the cover glass (<0.17 mm) and left to dry. Then, the cover glass is sealed on a glass slide with glue to exclude water or other contamination.

To obtain better single nanoparticle samples, there are other options. One is to use Poly-L-lysine solution to soak the cover glass for about an hour and then let it air dry. This can utilise surface charge to capture a single nanoparticle. Another option is to rinse the cover glass with 100 µl cyclohexane after dropping 0.01 mg/ml UCNP solution on it. This can remove the UCNP particles not attached to the surface and allow more sparse distribution. The third option is to use Mowiol® solution as an embedding media to fix UCNPs onto the cover glass, which will make the single nanoparticle sample last for a longer period of time.

2.3.2 How to find single nanoparticles

Methods to locate single nanoparticles are still required. Using the bright field to find the focus plane is not easy as the UCNP solution is transparent and the trace of this layer is not apparent in the camera.

We employ the laser spot on the CCD camera to locate the UCNP sample layer. As the sample is in the middle of two glass media, there is a refractive index difference. Therefore, the laser will have a stronger reflection on these interfaces. The sample surface should be in the first position of an obvious converged laser spot, as shown in Figure 2.9. Then, the 842 SP filter is placed in front of the camera to filter out laser spot, and the UCNP image is obtained (normally the camera exposure time must be adjusted to a much longer duration in order to view the UCNP image).
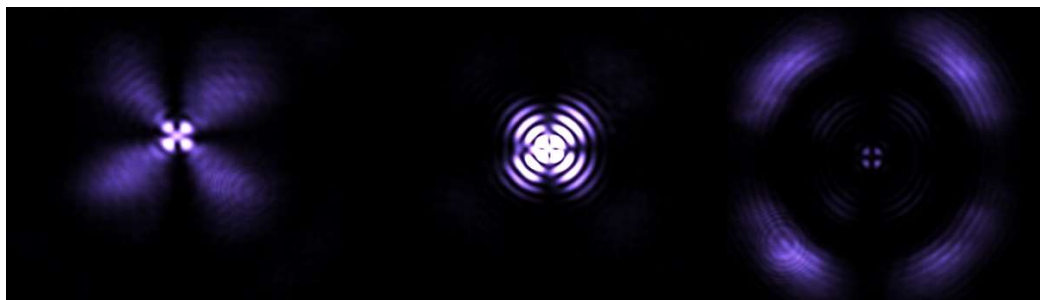
Figure 2.9 The change in the laser spot pattern when the sample is moved from far to near. Left is further than the focal plane, middle is on the focal plane, and right is nearer than the focal plane.

Luminous nanoparticles can easily be found by moving the XY stage after the sample layer is determined (fixed Z position). Now we need to recognise a single nanoparticle. The select criteria of single nanoparticles are that those particles have nearly the lowest emission brightness and there is a large enough quantity of them. The reason why we do not use the lowest emission brightness as the criteria is that the synthesis of UCNPs still leaves smaller UCNP particles in the sample. The fluorescent intensity of these nanoparticles is much lower than that of normal nanoparticles. Thus, we consider them as contamination rather than single UCNPs.

2.3.3 Single nanoparticle confocal intensity measurement
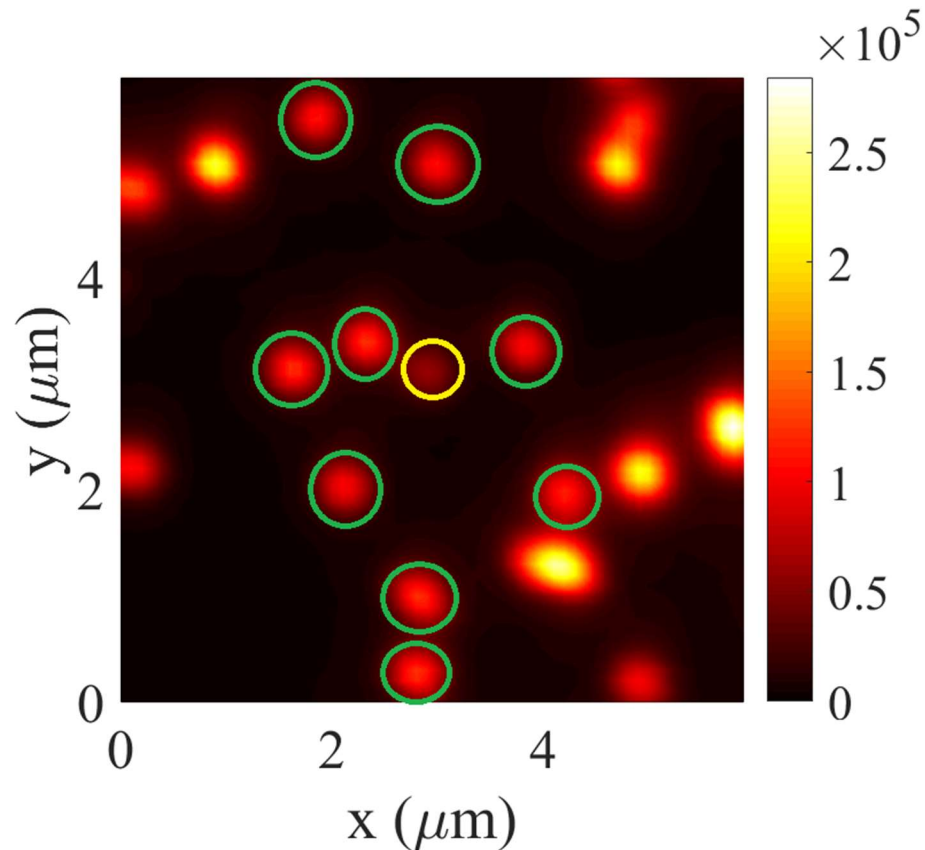
Figure 2.10 The confocal scan result of a UCNP.

Fluorescence intensity confocal scanning measurement is the basic function of the SNCS. As shown above, after the single nanoparticle area is located and we switch the flip mirror to allow the signal to reach the fibre which is connected to the SPAD detector. Then, we start to scan. The normal scan exposure time is 50 ms and the scan step is 0.1 μm.

The confocal scan picture can be drawn by MATLAB. As shown in Figure 2.10, the area with green circles is recognised as a single UCNP and the yellow circle area in the middle is the where we think there are rare minor particles whose size or quality is not sufficient.

2.3.4 Single nanoparticle spectrum measurement

To measure a single particle spectrum, we need to connect the fibre to the spectrometer. The sensitivity of this spectrometer is required to be high while the resolution of the spectrometer does not need to be very high. The standard resolution needed for studies today is about 0.5 nm. The spectrometer outputs the signal to a SPAD detector. As shown below in Figure 2.11, the spectrometer is controlled by a software we programmed using LabVIEW.
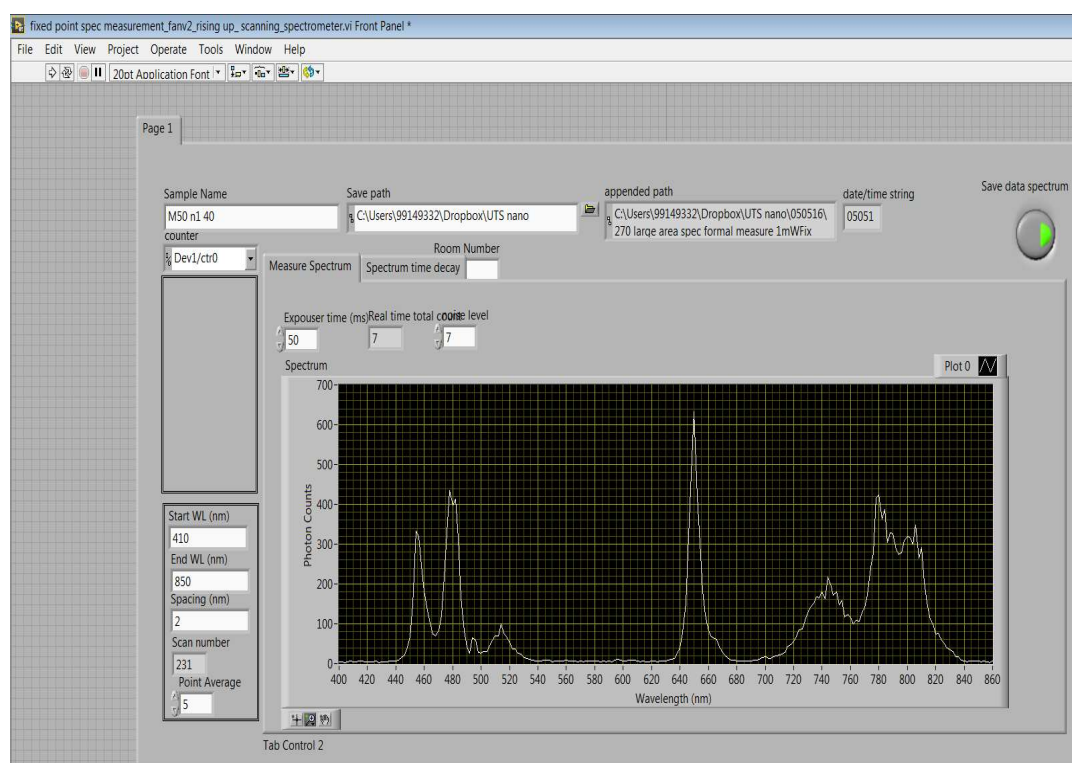
Figure 2.11 The interface of the spectrum measurement software.

2.3.5 Single nanoparticle lifetime measurement

Lifetime information can help the study of energy transfer mechanisms and the development of technologies like multiplexing or time-resolved imaging. When measuring lifetime, the excited laser needs to switch off, and the fluorescence intensity is measured over time. The time value since the laser switched off until the intensity decreases to $1/e$ of the initial value

is called the lifetime of the emission. The measurement program is shown in Figure 2.12.

A SPAD is a solid-state photodetector in which a photon-generated carrier (via the internal photoelectric effect) can trigger a short-duration but relatively large avalanche current. It exploits the incident radiation triggered avalanche current of a p–n junction when reverse biased.

However, SPADs has dark time. While the avalanche recovery circuit is quenching the avalanche and restoring bias, the SPAD cannot detect photons. Any photons that reach the detector during this brief period are not counted. This period is called dark time. The dark time for the SPAD used in SNCS is around the 20-30 ns level. For UCNPs, the lifetime scale is about 10 to hundreds of milliseconds. Thus, the dark time is not a big issue.
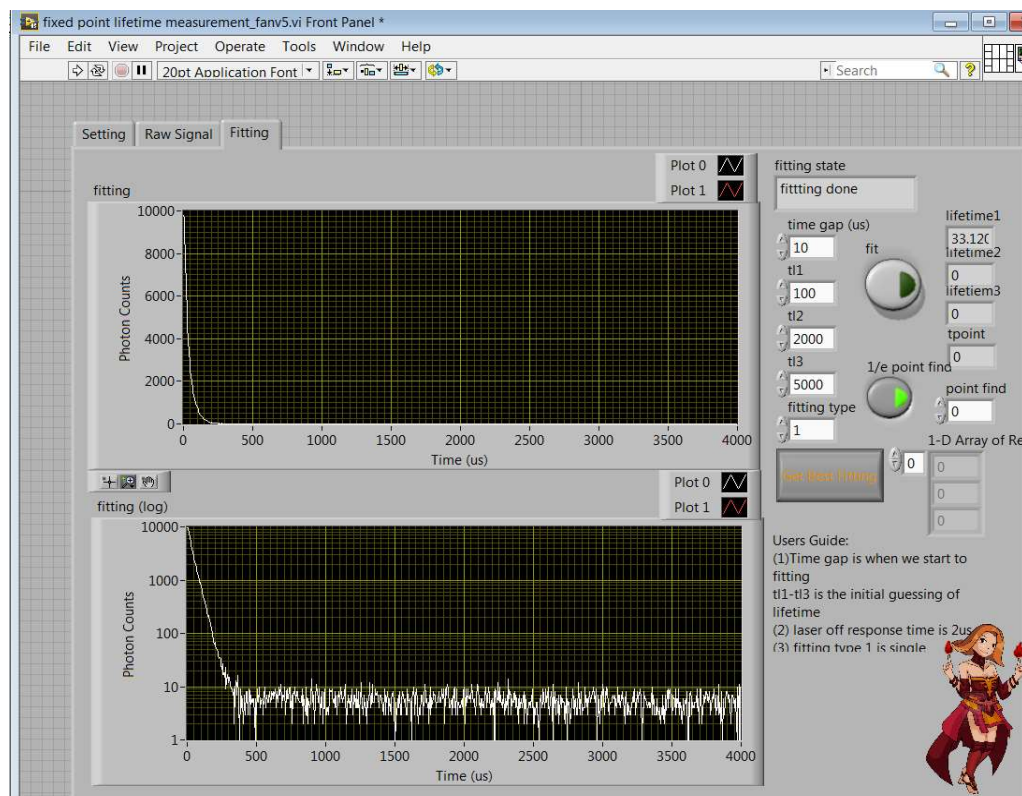
Figure 2.12 The interface of the lifetime measurement software.

2.4 Applications of the SNCS system

This developed SNCS system allows for quantitative measurement of the brightness, lifetime, and spectrum of a single UCNP. The advances in this SNCS system provide opportunities for a wide range of research, including material science and biomedical imaging research. After building this system, I then contributed to a series of research projects, as described below.

2.4.1 Applications of single particle brightness characterisation

The SNCS system can precisely measure the brightness of a single UCNP. We are able to measure a signal intensity as low as 50 counts/50 ms, which provides the ability to research nanoparticles with weak fluorescence intensity. The single UCNP characterisation is essential in these following works because the intensity change can only be confirmed in single particle level to exclude other factors.

One example of this application is for comparison of the cation exchange methods of UCNPs [3]. Most of the current fluorescence materials show colorful emission for light-based functionality beyond their size/morphology advantages, which enables their enormous applications in life science, display, energy harvest, and quantum engineering. To enrich the emission color, the cation exchange method allows the high-throughput production of multicolor emitting nanoparticles while preserving the original size, morphology, and crystal phase of the nanoparticles. Here, we developed a novel cation exchange method directly exchange the cations when the surface of the as-synthesized nanocrystals is capped with ligands. It is called organic solvent cation exchange (OSCE) method.

My contribution in this research is to compare this method with traditional cation exchange of UCNPs in water (WACE) with single nanoparticle confocal intensity characterization. The intensity of the particles after cation exchange is so low that cannot be characterized with typical confocal system. I carefully applied the method introduced in 2.3.2 and successfully find the single UCNP. Also, because of the low intensity, there is a balance between scanning speed and the mobility of the particles. High scanning speed would reduce the intensity we could collect while low scanning speed would cause mobility of the particles which is caused by the motor stage.
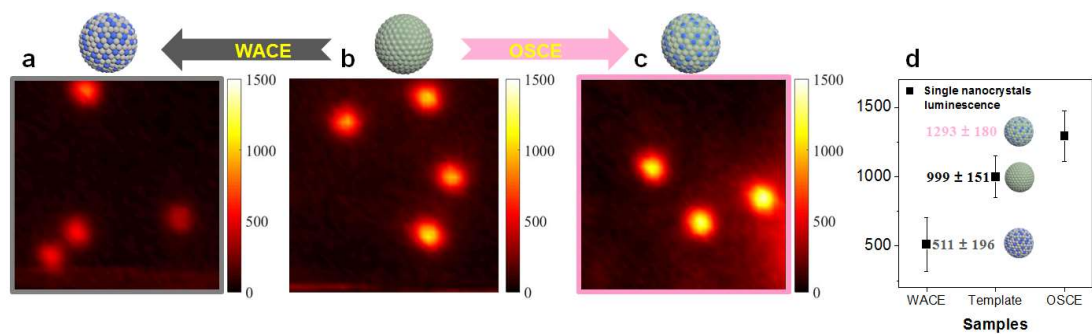
Figure 2.13 The confocal scanning images and the averaged brightness of core-shell NaGdF4: Yb^{3+}, Tm^{3+}@NaGdF4 single nanocrystals. (a-c) Confocal images of UCNP by WACE, an initial template of UCNP, and UCNP by OSCE, respectively (under 1 μM Tb^{3+} exchange). (d) Brightness statistics for the single UCNCs corresponding to a−c [3].

Using the SNCS system to characterise the intensity of cation exchanged single UCNPs (Figure 2.13), we can clearly see that the OSCE method enhances the intensity while the traditional WACE method decreases the intensity to some extent. The OSCE method produces 2.5-fold stronger intensity than the WACE method. From Figure 2.13 we could clearly see the intensity of the UCNPs in all of the three samples (WACE, the initial template of UCNP, and UCNP by OSCE) is around 100 counts per 50ms, which is far beyond the limits of the commercial confocal system. The

quantitative compare gives a clear evidence of the advantage of our OSCE method. This facile and rapid OSCE strategy opens a new way for the synthesis of UCNCs with intense colourful luminescence.

Another example of using the SNCS system is for characterisation of UCNPs with different sensitiser doping concentrations in order to study the concentration quenching effect. This study aims to enhance the brightness of UCNPs [4].

To enhance the brightness of UCNPs, increasing the sensitizers' concentration is a normal method. However, to avoid concentration quenching effect, normally we could only use 20% sensitizer (Yb^{3+}) concentration. Here we find surface quenching and the large size of $NaYbF_4$ nanocrystals are the only factors limiting Yb^{3+} optimal concentration.

My contribution to this work is applying SNCS to characterise the emission intensity of single UCNPs with modified sensitiser doping concentrations and core-shell structures. The intensity of the particles we measure here is also quite low (hundreds of counts per 50ms). We also applied the careful particle search method to find the particles. And the system is fully aligned to optimise the collected signal. The noise level is carefully minimised by reducing the laser scattering and other noise source.

Figure 2.14 shows the confocal scanning of the samples with higher sensitiser doping concentration compared with the monolithic UCNPs of $NaYF_4$: 20% Yb^{3+}, 4% Tm^{3+}. In this Figure, core particle $NaYF_4$: 60% Tb^{3+}, 4% Tm^{3+} with a size of 8.9 nm is used to make smaller particle size as size of Yb^{3+} highly doped particles cannot be controlled well at smaller size. A thin layer of $NaYF_4$ inert shell is also applied to reduce the surface

quenching of the Yb³⁺ highly doped particles. Two groups of particles with size around 13 nm and 25 nm is fabricated for this research.
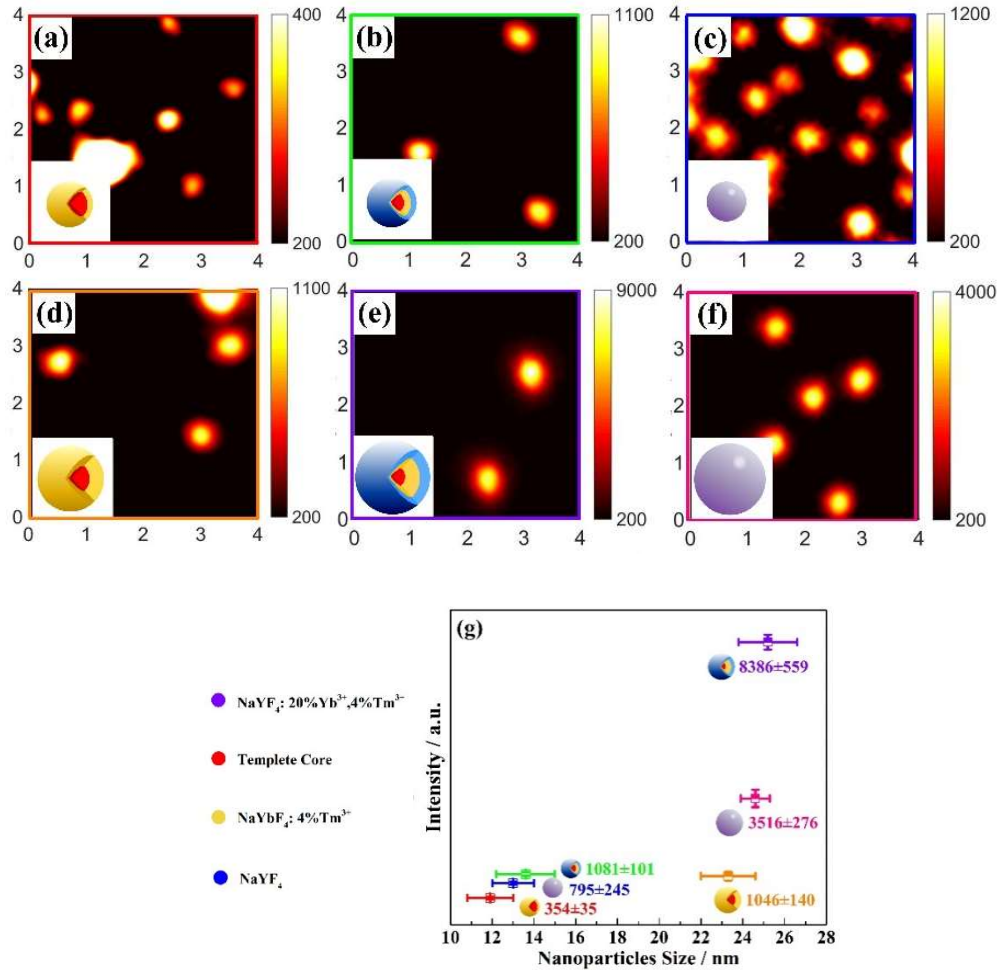
Figure 2.14 Confocal microscopy quantitative measurement of the whole spectrum emission for single UCNPs. (a) UCNPs of template core−active shell of NaYbF₄: 4% Tm³⁺ with a size of 11.9 nm, (b) UCNPs of template core−active shell−inert shell of NaYF₄ with a size of 13.6 nm, (c) monolithic UCNPs of NaYF₄: 20% Yb³⁺, 4% Tm³⁺ with a size of 13.0 nm, (d) UCNPs of the template core−active shell with a size of 23.2 nm, (e) UCNPs of the template core−active shell of NaYbF₄: 4% Tm³⁺−inert shell of NaYF4 with a size of 25.2 nm, (f) monolithic UCNPs of NaYF₄: 20% Yb³⁺, 4% Tm³⁺ with a size of 24.6 nm, (g) quantitative analysis of the whole spectrum emission intensities for single UCNPs corresponding to a−f [4].

Based on our quantitative measurements (Figure 2.14), we could see that the Yb^{3+} highly doped particles are 1.36 times and 3.78 times higher than monolithic UCNPs in the sizes of 13.6 and 25.2 nm. In conclusion, we found that the optimal sensitiser concentration in a single UCNC is not limited by the "concentration quenching" effect as long as surface defects and interior defects can be minimised. The reliable measurement of nanoparticle intensity using SNCS system provides firm evidence to prove the factor of highly Yb^{3+} doping concentration, which is the essential test method for this research.

2.4.2 Applications of single particle power dependent measurement

With our precise power change unit, we can conveniently measure the power dependent properties of UCNPs by changing the optical density from 10^2 to 10^8 W/cm². One application is to characterise the power dependent fluorescence intensity of UCNPs with different activator concentrations [2].

Long-term 3D tracking of nanoparticles and their intracellular motions have provided us opportunities of understanding of intracellular activities such as endocytosis and exocytosis. The sophisticated correlative optical-electron microscopy and scientific-grade cameras are often used to study intercellular processes. Nonetheless, most of these studies are still limited by separating a single nanoparticle from a cluster of nanoparticles or their aggregates. Here, I developed a novel method to separate them using the characterisation of single UCNP.

As shown in figure 2.15, the power dependent property of 8% and 1% mol Tm^{3+} doped UCNPs was measured. We could see the intensity of 1% Tm^{3+} particle is higher at lower excitation power while 8% Tm^{3+} particle is brighter at higher excitation power.
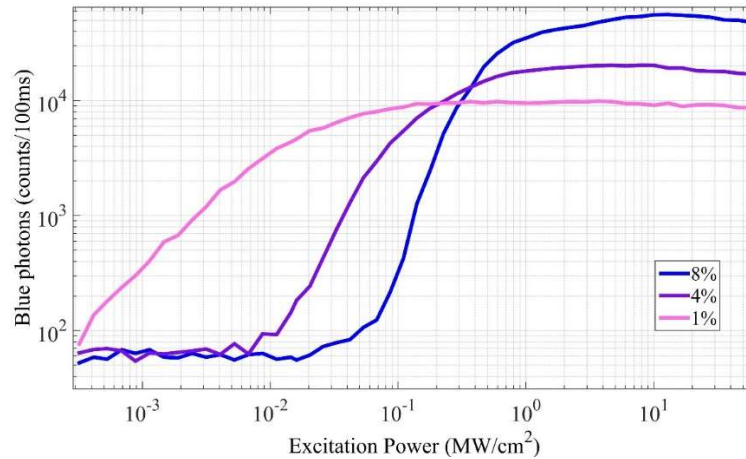
Figure 2.15. Blue band (475±25 nm) power dependent emission response curve for single UCNPs with Tm^{3+} doping concentrations of 8%, 4%, and 1% mol [2].

This property can be used to distinguish them by changing the excitation power, which provides the fifth-dimension tracking of single UCNP as shown in figure 2.16. In Figure 2.16, in the first column, (a)-(c) show, under low excitation power 0.0557 MW cm^{-2}, only the blue emission of the 1% mol Tm^{3+}-doped UCNPs are visible for single UCNP observation. Under a medium excitation power density of 0.2783 MW cm^{-2} and with the same settings of the CCD camera, both 8% mol Tm^{3+} UCNPs and 1% mol Tm^{3+} UCNPs can be seen. Under high excitation intensity, 0.6851 MW cm^{-2} and above, the 8% mol Tm^{3+} UCNPs can be distinguished with other particles with adjusting the camera gain as they are super bright.
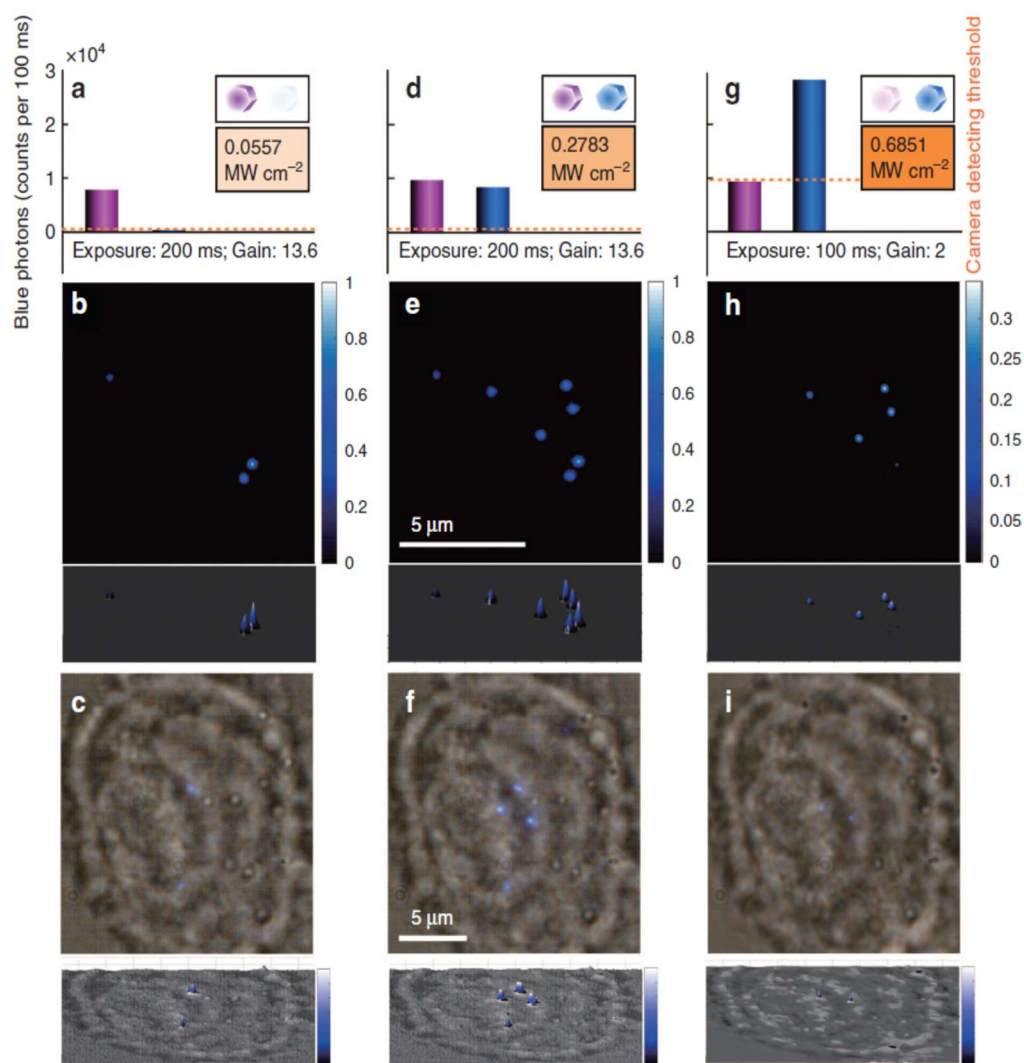
Figure 2.16 Multiplexed imaging strategy for tracking multiple types of UCNPs at the same emission colour band. (a–c) Under an average excitation power density of 0.0557 MW cm⁻² and with the CCD camera set at a 200 ms exposure time with a gain value of 13.6, only the blue emission of the 1% mol Tm^{3+}-doped UCNPs are sufficiently bright for single UCNP observation. (d–f) Under a medium excitation power density of 0.2783 MW cm⁻² and with the same settings of the CCD camera, the 8% mol Tm^{3+} UCNPs start to emit a comparable amount of upconversion luminescence to that of the 1% mol Tm^{3+} UCNPs. (g–i) Under a relatively high excitation intensity, e.g., 0.6851 MW cm⁻² and above, the 8% mol Tm^{3+} UCNPs become so bright that they saturate the camera; thus, a reduced gain (a value of 2) and an exposure time of 100 ms are applied for the image recording [2].

2.4.3 Applications of wide-field single particle imaging

As discussed above, wide-field imaging is crucial for studies of large areas of interest such as single nanoparticle tracking. To expand the excitation area, as discussed in Section 2.2.2, we constructed a wide-field imaging module. Using this wide-field imaging module we were able to expand the excitation area.

To distinguish single nanoparticles, the standard emission intensity of UCNP under known excitation intensity is needed. But the excitation beam is still of Gaussian profile after expansion. To distinguish them easily, it is good to make the excitation of them on a same value. With the power dependent properties measured by the SNCS (Figure 2.17 a), together with excitation power distribution, we were able to calculate the standard emission intensity in the FOV (Figure 2.17 b).
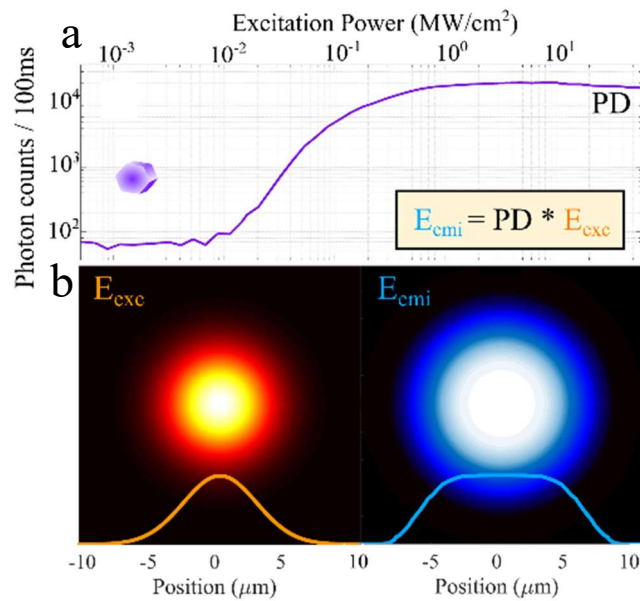
Figure 2.17. (a)The excitation power dependent curve of a single 4% mol Tm^{+3}-doped UCNP.(b) The bottom red spot is the excitation laser pattern. The bottom blue pattern is the emission intensity of a single UCNP in different positions of the excitation beam. [2].

Then we could compensate for the fluorescence intensity in the wide-field image to ensure it was excited with the same intensity. The original image under excitation is shown in Figure 2.18 (a). It could be converted to make all the particles within this wide area have the same excitation intensity using Look Up Table method (LUT) (Figure 2.18 (b)). Then, single nanoparticles could be easily distinguished, and the non-single particles could be filter out. It is clear that the This method provides an efficient way to distinguish single nanoparticles; this method could easily be applied for cell tracking [2].
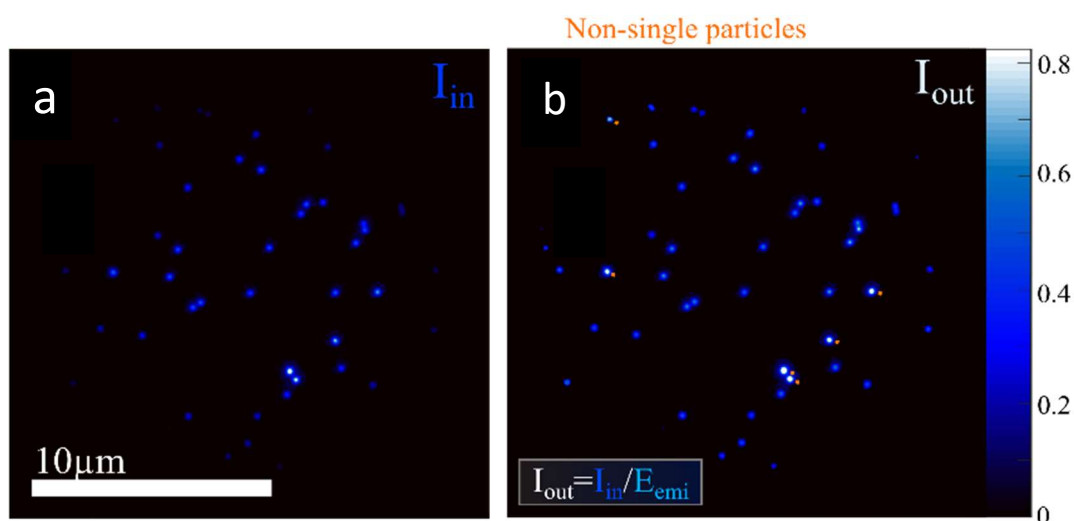
Figure 2.28 (a) CCD recorded image before LUT correction. (b) Intensity compensated image is able to be used in single UCNP determination[2]. The emission pattern (E_{emi}) which indicates emission intensity of a single UCNP will vary in different positions of excitation beam. E_{emi} can be calculated through $E_{emi} = PD* E_{exc}$, where PD is the excitation power dependency of emission intensity of single UCNP and can be measured through single particle characterization. E_{exc} is the calculated excitation beam profile with measured spot size.

2.5 Conclusions

In this chapter, I first described the methods used to design and build a single UCNP characterisation system (SNCS). The design of this system had to consider the properties of UCNPs, including emission wavelength and power dependent properties. This finished system is an advanced state-of-the-art system for UCNP characterisation.

Then I introduced the operation of this SNCS including descriptions of sample preparation, the search for single UCNPs, and normal measurements. It takes a lot of time to explore these factors and this chapter could be a guidebook for researchers using similar systems.

Finally, the applications of the SNCS were introduced. Weak single nanoparticle intensity measurement, power dependent measurement, and wide-field imaging provide many opportunities for researchers in material science to study UCNPs. The SNCS opens up the door for single nanoparticle researchers in biphotonic applications.

In summary, I have introduced the details of the SNCS system we have built based on confocal microscopy. Though the confocal microscope is not complicated, it consistently plays an important role in biophotonics. Many technologies, including super-resolution technologies (e.g., STED and GSD) and optical tweezers, can be constructed from a confocal microscope.

References

1.   Fellers T.J. and Davidson M.W. *Olympus fluoview resource center*. Available from: http://fluoview.magnet.fsu.edu.

2.   Wang F., Wen S., He H., et al., *Microscopic inspection and tracking of single upconversion nanoparticles in living cells.* Light: Science & Applications, 2018. **7**(4): p. 18007.

3.   Guan M., Zhou Z., Mei L., et al., *Direct cation exchange of surface ligand capped upconversion nanocrystals to produce strong luminescence.* Chemical Communications, 2018. **54**(69): p. 9587-9590.

4.   Ma C., Xu X., Wang F., et al., *Optimal sensitizer concentration in single upconversion nanocrystals.* Nano letters, 2017. **17**(5): p. 2858-2864.

Chapter 3. Optimising passivation shell thickness of single UCNPs using a time-resolved spectrometer

3.1 Introduction

3.1.1 Smaller and brighter UCNPs

Upconversion nanoparticles (UCNPs) are typically based on $NaYF_4$ nanocrystals doped with Yb^{3+} ions as sensitisers and Tm^{3+} or Er^{3+} ions as emitters (activators). The sensitiser ions (Yb^{3+}) have relatively large absorption cross-section areas that can be used to sensitise near-infrared (e.g., 980 nm) photons. Through a network of phonon-assisted energy transfer processes, the sensitizers with high cross section areas can absorb the excitation photons efficiently and transfer to the activators. The activators typically have ladder-like multiple intermediate excited states. When one of the excited states matches that of the sensitiser ions and, most importantly, the lifetime is long enough (typically a few microseconds), the intermediate excited state can accumulate more than two sensitised photons. It can then up-convert the photons into the high energy levels of the activator to emit visible and even UV emissions [1]. Such an efficient multi-photon energy transfer process makes single UCNPs detectable under a low excitation power density of a few hundred W/cm^2. That is five orders of magnitude lower than the minimum excitation density required by conventional two-photon probes [2, 3].

UCNPs are the most efficient multi-photon probes for *in vitro* and *in vivo* bio-imaging [4, 5], deep tissue nano-thermometry sensing [6], and near-infrared induced photothermal therapies [7]. We discovered that highly doped UCNPs are super bright in micro-structured photonic fibres or under fluorescence microscopy [8, 9]. This makes them suitable for single molecule sensing. Further, we discovered that highly doped UCNPs can

easily build population inversion on one of the excited states, which helps to emit stimulated emissions under a low-power stimulated depletion laser. For example, at 808 nm, the first upconversion super-resolution nanoscopy using a low-cost low-power diode laser was enabled [10]. This suggests that UCNPs are suitable for long-term super-resolved imaging of sub-cellular structures and single biomolecules through deep tissue.

Nevertheless, developing smaller and brighter UCNPs is desirable for cellular and sub-cellular applications. The grand challenge is their relatively large surface, which is accessible to numerous surface quenchers. This explains why upconversion nanoparticles have significantly lower quantum efficiency than bulk crystals.

3.1.2 Passivation effect

In recent years, passivating UCNPs with inert shells has been found to be very useful for separating UCNPs away from surface quenchers, thereby significantly enhancing the brightness of UCNPs [11, 12].

The passivation effect has also been found to be useful for increasing the concentrations of both sensitisers [8] and activators [13]. This reduces the minimum excitation power required for imaging and tuning the energy transfer process [14-16]. Conversely, the shell cannot be too thick, as this results in larger sizes of UCNPs. The question of how thick it should be requires further quantitative research [17]. Ideally, it should be determined by quantitative measurement of single UCNPs. The former initial researches to optimize shell thickness for UCNP was carried out by measuring particle aggregates in solutions[18]. However, this is limited by the sensitivity of the available instruments.

3.1.3 Challenges associated with single nanoparticle characterisation for researching energy transfer

The characterisation of single nanoparticles will continue to advance the field of nanotechnology, including quantification of single nanoparticles and correlating their structure and growth conditions [8, 13, 19, 20]. The simultaneous measurement of both the spectrum and the lifetime decay of a single UCNP is important for understanding the energy transfer and optical properties of UCNPs. However, there have been challenges due to the weak emissions from single UCNPs. L. Zhang et al have developed a time-resolved spectroscopy system for UCNPs [21], yet its sensitivity cannot reach for single UCNP.

We have developed a filter-based spectrometry system and have applied it to single nanoparticle characterisation. We investigated the emission brightness, spectrum, and temporal domain behaviours of UCNPs with different shell thicknesses. We examined both the raising time during pulsed excitation and the decaying behaviours after the excitation pulses. We found that the optimal shell thickness of 5 nm resulted in the highest emission brightness for the fully emitted wavelength. A shell thickness of 21.5 nm resulted in the highest brightness for 455 nm. It also resulted in the highest ratio of emission brightness between 455 nm and 800 nm. Further, we demonstrated that the spectrometry system is sensitive enough to measure the time-resolved spectrum from a single UCNP, with the emission rate as low as 60 counts per ms; this finding is significant for the comprehensive study of the energy transfer processes of UCNPs. This demonstration is also significant for UCNP multiplexing sensing which is based on both wavelength and lifetime.

3.2 Experiments

3.2.1 Materials

To identify the optimal shell thickness and to investigate its role in the upconverting process of UCNPs, we synthesised a series of UCNPs with differing core-shell structures. The core was NaYF$_4$: 8% Tm^{3+}, 20% Yb^{3+} UCNPs. Such high Tm^{3+} doping concentrations have been found to be very useful in biophotonic applications such as single nanoparticle sensing [9] and super-resolution imaging [22]. The shell was inert NaYF$_4$. Therefore, it will only passivate the surface of UCNPs without bringing extra energy transfer. As shown in the TEM images, the core of the UCNP was 30 nm (Figure 3.1(a)) and the shell thicknesses were the shell the shell thicknesses were 1.1 nm, 6.3 nm, 8.4 nm, 25.9 nm and 29.5 nm, respectively (see Figure 3.1(b), (c), (d), (c), and (f), respectively). Here, the size bar is 100 nm. The single nanoparticle sample was prepared as described in Chapter 2.
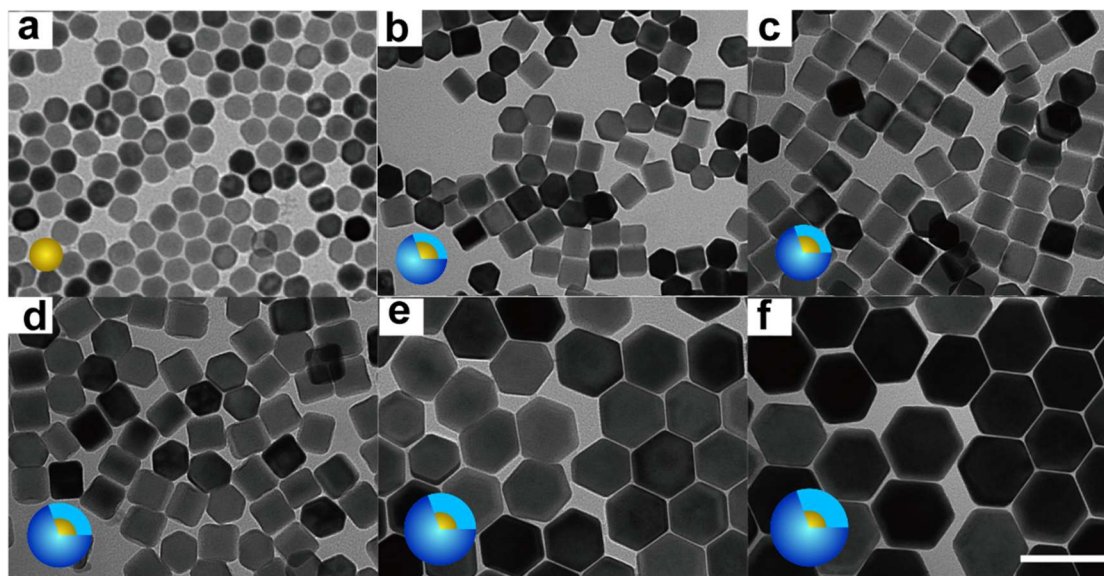
Figure 3.1 TEM images of the UCNP cores of NaYF$_4$: 8%Tm^{3+}, 20%Yb^{3+} (a) and the UCNP core-shells of NaYF$_4$: 8%Tm^{3+}, 20%Yb^{3+} - NaYF$_4$ with different shell thickness of (b) 1.1 nm, (c) 6.3 nm, (d) 8.4 nm, (e) 25.9 nm and (f) 29.5 nm. Scale bars is 100 nm.

Figure 3.2 is a result done by my collaborator, it shows the EDS analysis of single core-shell UCNPs (NaYF$_4$:Yb, Er@NaGdF$_4$), where the NaGdF$_4$ was clearly seen as the shell from the Gd elemental map while Yb and Y

were shown in the core area. Line scanning across an individual nanoparticle shows that the Yb and Y has decreased profile from the core to the shell area while the Gd profile increases from core to the shell as labelled in the squares. This suggests that the ion exchange occurred at the interface of the core and shell for the Yb diffusing from core to the shell.

This ion exchange from core to shell results in a less effective shell thickness than the designed shell thickness, as the doping ions in the core diffuse into the inert shell. However, the ion exchange would only occur within 5 nm at the interface, suggesting the ion exchange effect would be mitigated when the shell thicker than 5 nm.
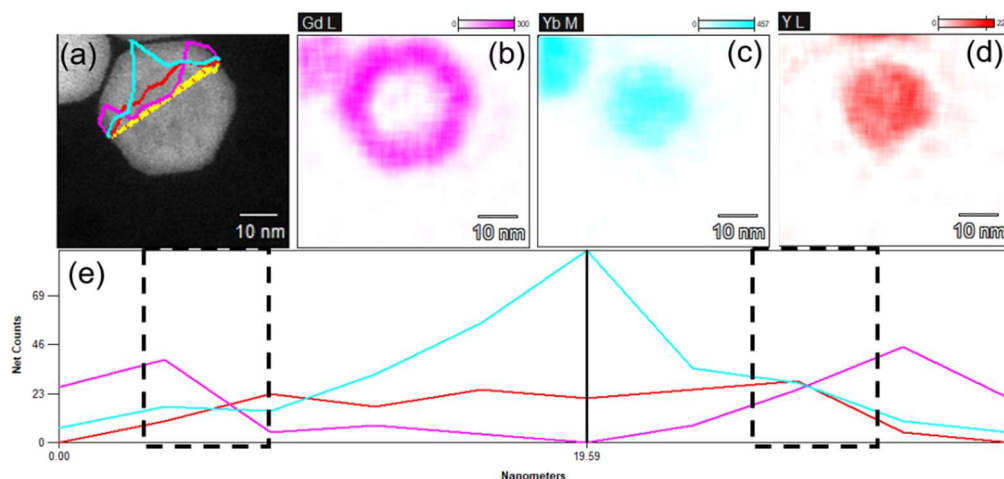
Figure 3.2 (a) TEM image of NaYF$_4$:Yb, Er@NaGdF$_4$ nanoparticles, (b-d) Elemental mapping graphs of Gd, Yb, and Y respectively corresponding to the nanoparticle in (a), (e) line scanning across the individual nanoparticles in (a) for the elements of Gd, Yb and Y.

3.2.2 System and spectrometer design

With the aim of comprehensively studying a single UCNP, we developed an optical filter-based spectrometer coupled to the SNCS. The detailed introduction of this system can be found in Chapter 2.

For spectrum measurement, the emission from the sample was input to a filter-based spectrometer (Figure 3.3(a)) through an optical fibre. It was

then focused onto a long pass linear variable filter (LVLWP, Delta) and a short pass linear variable filter (LVSWP, Delta) to select certain output wavelengths. This was coupled to a SPAD though an optical fibre. The spectrum was measured by recording the signal from the SPAD for different output wavelengths.

The resolution of this spectrometer is about 3nm, which is limited by the filter band pass sharpness we used to build the spectrometer. To calculate the resolution, we measure the spectrum of a wide spectrum light source. We moved the filters closed enough to make the left and right edge of the spectrum meet. Then we moved them closer, to make the top light intensity of the spectrum decreased to 80%. At last, the FMHM of this final spectrum peak is the resolution we can achieve.

The emission spectrum from a single UCNP taken by this filter-based spectrometer is shown in Figure 3.3(b). This demonstrates a signal intensity that is at least seven times higher than a commercial spectrometer (Horiba, Micro-HR), despite having the same UCNP, SPAD detector, and exposure time. This enhancement stems from the fact that a diffraction grating-based spectrometer loses part of the optical signal on other, useless diffraction orders. It suggests that the filter-based spectrometer is ideal for analysing single nanoparticles with weak emissions, such as single UCNPs with emission rates as low as 10 counts/1 ms (Figure 3.3(b)).
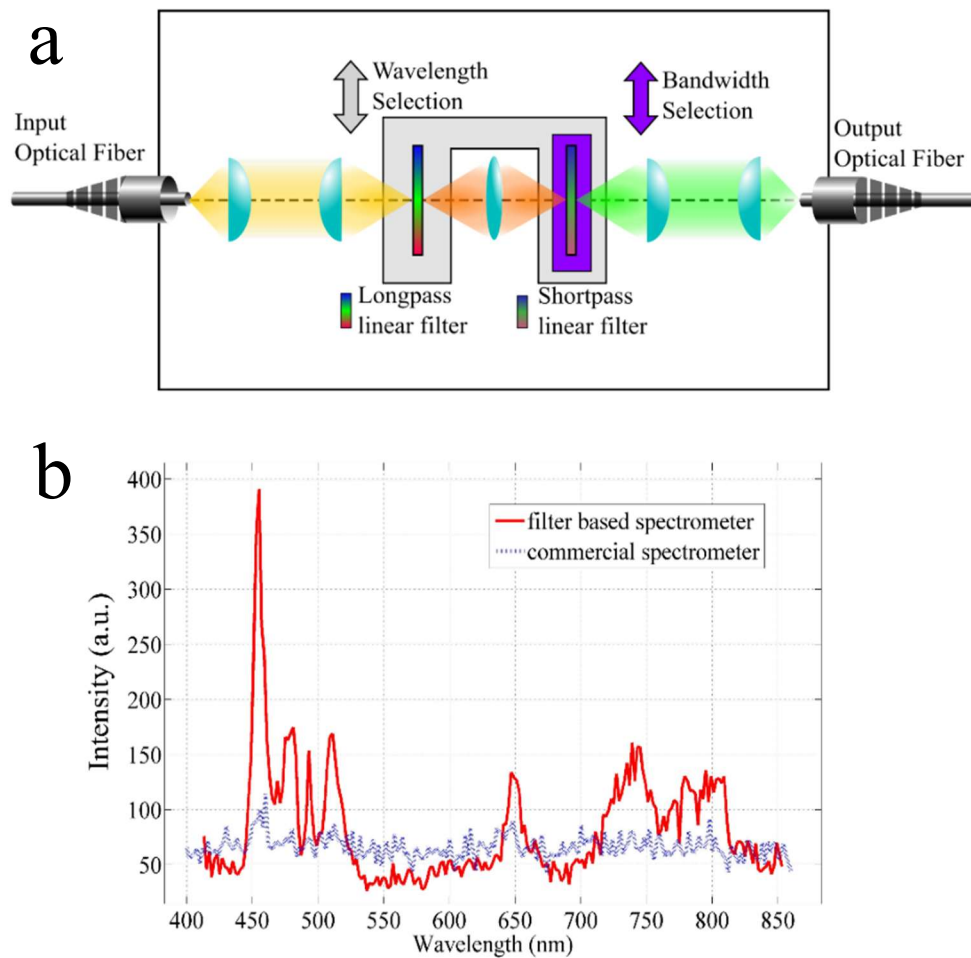
Figure 3.3 The optical set up to measure a single particle image, spectrum, and time-resolved spectrum. (a) Laser scanning confocal microscopy system coupled with an optical filter-based spectrometer through an optical fibre. (b) The optical design of the optical filter-based spectrometer. The bandwidth of output wavelength from the spectrometer is controlled by the relative position between two filters which control the balance between spectrum resolution and output signal strength. The central wavelength value is selected by moving the two filters to certain positions with respect to the optical axis of the system. (c) Emission spectrums from a single upconversion nanoparticle with emission brightness of 10 counts/1 ms, measured with a commercial spectrometer and our filter-based spectrometer with the same detector and measurement conditions.

3.3 Results and discussion

3.3.1 Intensity

A quantitative comparison of emission brightness between UCNPs with different shell thicknesses is shown in Figures 3.4 (a) and (b). The quantitative measurement was conducted by confocal imaging of single UCNPs (Figure 3.4(b)) with the aforementioned system (Figure 3.4 (a)). Each Gaussian spot in the confocal image represents a nanoparticle. Its maximum pixel value indicates the brightness of the particle (i.e., the integrated emission intensity from all wavelengths). The emissions of UCNPs with different shell thicknesses are uniform, with a mono-dispersed intensity profile. At least 15 particles were used to calculate the intensity of particles of one thickness. This was used to calculate the average emission intensities shown in Figure 3.4 (a).

The result shows clearly that the overall emission intensity of the core-shell UCNPs was greatly enhanced with the shell coating in 1.1 nm and reached to the maximum with the 6.3 nm and 8.4 nm inert shell. With much thicker shell coating in 25.9 and 29.5 nm, the overall emission intensity slightly dropped. The enhancement of the emission intensity can be attributed to the passivation role of the inert shell preventing the surface quenching from quantum tunnelling. The maximum passivation was achieved in shell thickness of 6.3 nm as well as 8.4 nm owing to the ion exchange effect [23, 24], i.e., the diffusion of sensitizer and emitter ions from core to the inert shell. Owing to the concentration gradient from core and the inert shell, the ion exchange would occur at the interface of the core and the shell within around 5 nm [25-27], which results in a less effective shell thickness than the physical shell thickness and mitigated the shell passivation effect from the possibly diffused ions to the surface.

Thereby, the thin shell would not passivate the surface quenching efficiently as the thicker shell, thus the optimized surface passivation was presented with the shell in 6.3 nm and 8.4 nm for the maximum intensity. The slight decrease with even thicker shell coating could be attributed to the possible defects between the shell layers because there were two or three steps for the thick shell coatings.
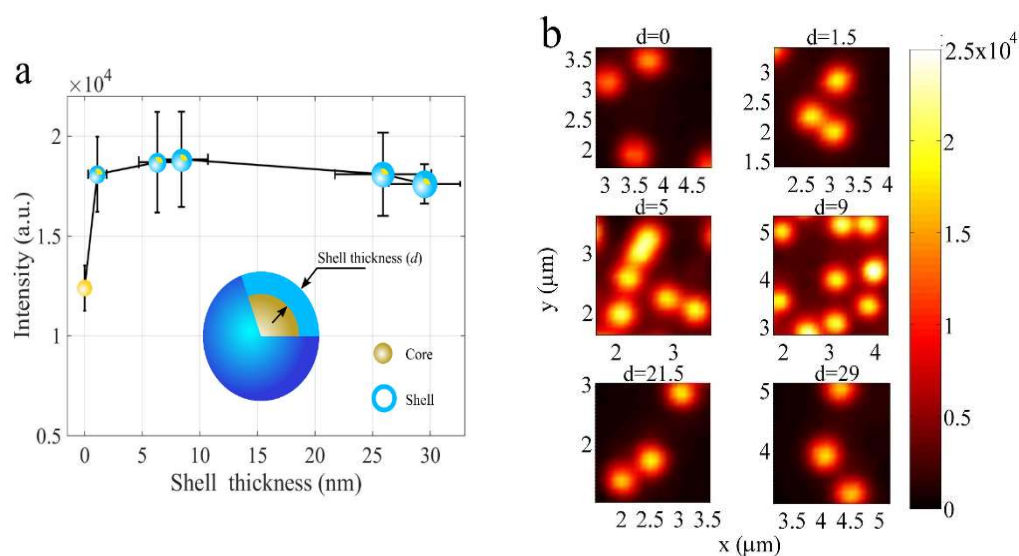
Figures 3.4 Comparison of emission brightness between upconversion nanoparticles (UCNPs) with different shell thicknesses. (a) Emission intensity of UCNPs with different shell thicknesses. (b) Confocal microscopy quantitative measurement of single NaYF$_4$: 8% Tm^{3+}, 20% Yb^{3+} UCNPs with different shell thicknesses: 0, 1.5, 5, 9, 21.5, and 29 nm. The unit of the colour bar is counts per 50 ms.

To further understand the physical process of the core-shell structure, we employed single particle spectrum and time-resolved emission analysis.

3.3.2 Mechanism discussion with detailed data

The emission spectrums from single UCNPs with different shell thicknesses are compared in Figure 3.5(a), in which the peak intensities of 455 nm, 651 nm, and 805 nm were tracked and plotted as inset figure of 3.5 (a).
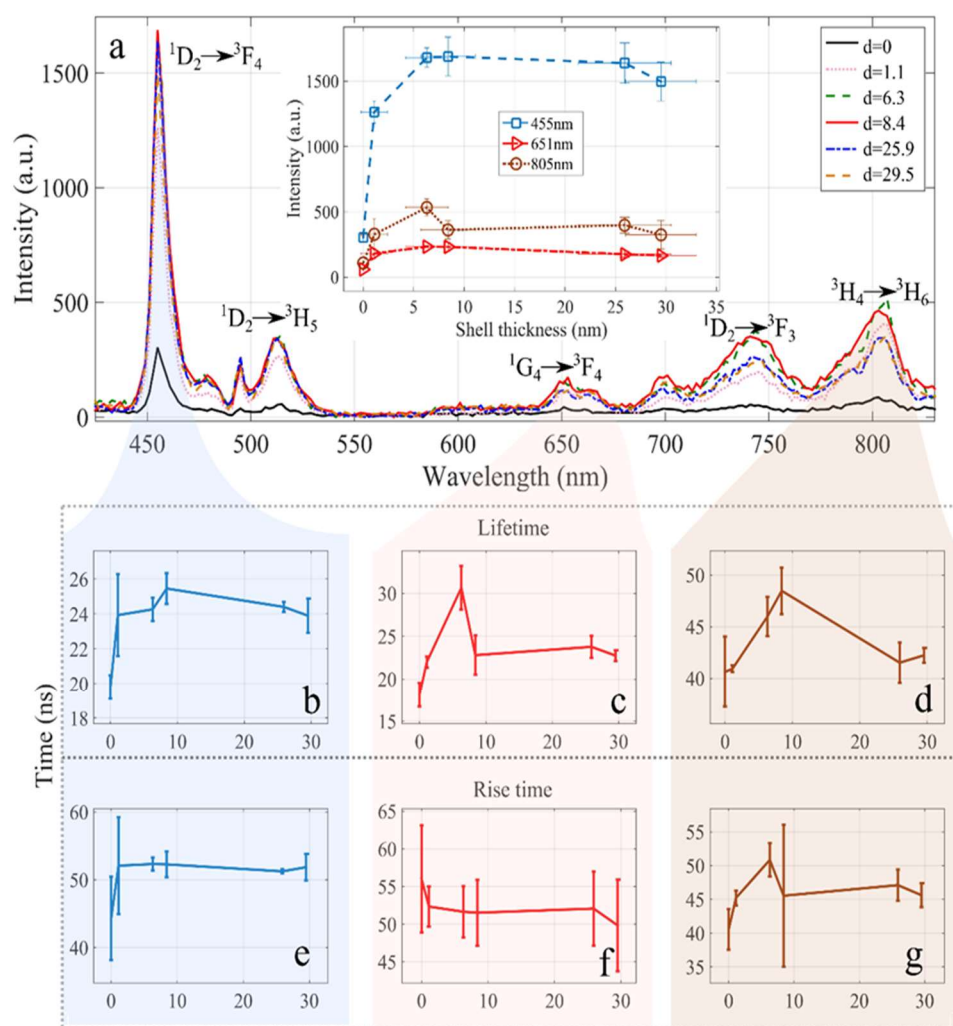
Figures 3.5 (a) Spectra of single UCNPs core and core-shell nanostructures with different shell thickness. The inset figure is the averaged intensity values for 455 nm, 651 nm and 805 nm emission amplitude and the energy transfer diagram. The lifetime and rise time of UCNPs emission for 455 nm (b and e), 651 nm (c and f) and 805 nm (d and g).

By increasing the shell thickness the intensity of all three emissions are enhanced and all reached to the maximum at the 6.3 nm shell and plateaued at the 8.4 nm, then a slight decrease occurred along the increase of the shell thickness. This finding is consistent with the quantitative measurement conducted via the confocal imaging for the single UCNPs (Figure 3.4 (a)). 6.3 nm thick inert shell is the optimised shell coating

could be attributed to the fully passivated surface on core UCNPs. The surface passivation stops the non-radiative energy transfer from sensitisers (Yb^{3+}) and emitters (Tm^{3+}) to the surface quenchers but enables more efficient energy transfer from the sensitisers (Yb^{3+}) and emitters (Tm^{3+}). Consequently, this could induce a significant increase in the rise time of low energy level (805 nm) (shown in Figure 3.5(g)) due to the accumulative photons at the lower level for the inert shell passivated UCNPs. On the contrary, the photons at the lower level (805 nm) would be excited to higher levels (455 and 651 nm) inducing small increase in the rise time for higher energy levels (shown in Figures 3.5 (e) and 4 (f)). This can be attributed to a lower carrier transfer rate from the sensitiser. The surface passivation also terminates the non-radiative transition path in the emitter so that the lifetimes are increased (shown in Figures 3.5 (b), 3.5 (c) and 3.5 (d)).

When the shell thickness increases to more than 8.4 nm, apart from the termination of the non-radiative path, two energy transfer processes start to play larger roles. As a result of the competition between the two processes, as shown in Figure 3.6, emission intensity from 455 nm ($^1D_2$ to $^3F_4$) shows less dependence on shell thickness. Emission intensities from 651 nm ($^1G_4$ to $^3F_4$) and 805 nm ($^3H_4$ to $^3H_6$) decrease with increased shell thickness (see Figure 3.5 (a)).
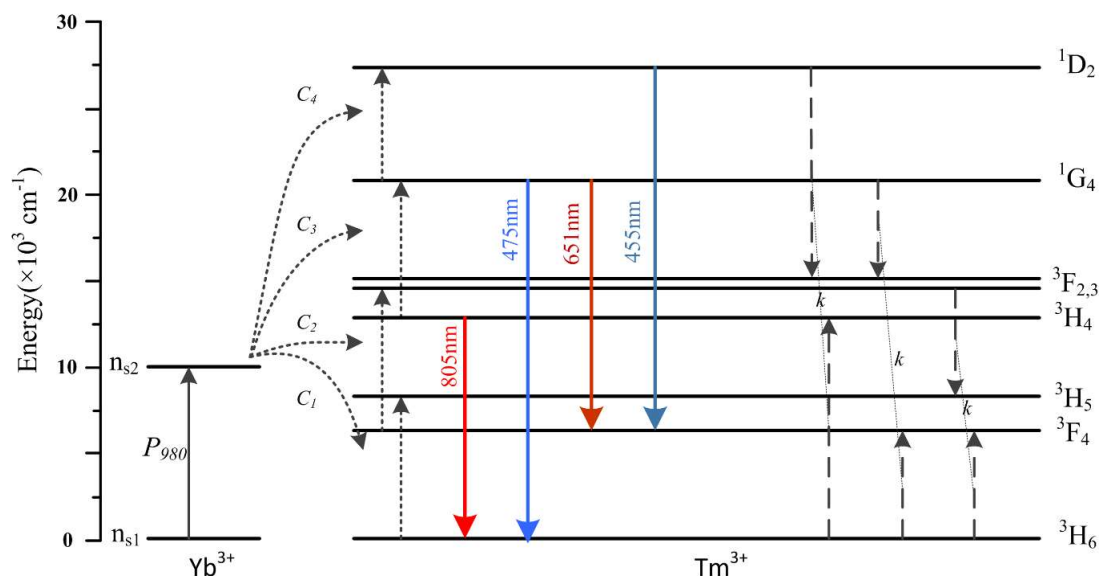
Figure 3.6 Energy level diagram for NaYF$_4$: 20%Yb^{3+}, 8%Tm^{3+}

One of the processes is the enhancement in upconversion efficiency. This stems from the rebalancing of carrier distribution after surface passivation. This process decreases emission intensity from lower energy levels (651 nm and 805 nm) but increases emission intensity from higher energy levels (455 nm). This process also decreases the raising time and lifetime on $^3H_4$ levels because more carriers move to higher energy levels (see Figures 3.5 (d) and (g)).

We suggest that there is another unknown process that induces a non-radiative transition path. Its effectiveness is confirmed by the decreased lifetime on $^1D_2$ (see Figure 3.5 (c)) and the reduced intensity of 455 nm. This is despite the fact that it is balanced out by an enhanced upconversion process. This unknown process results from element diffusion or stress introduced internal defect during the shell growth period.

the enhancement in upconversion efficiency is mediated, which results in smaller decrease on the lower energy levels (651 nm and 805 nm) shown in figure 3.5 (c), 3.5 (d). The reduced intensity in both higher energy level and lower energy levels (455nm, 651nm and 800 nm at insert figure)

indicates the non-radiative transition. In this region, the internal quencher may be increased from the interfaces between the sequent coated shells for 25.9 nm and 29.5 nm shells. It is worth noting that the lifetime of 800 nm (Figure 3.5 (d)) reaches its maximum when shell thickness is 8.4 nm, in which the surface of UCNP is totally passivated. All the suggested processes discussed are shown in Figure 3.7.
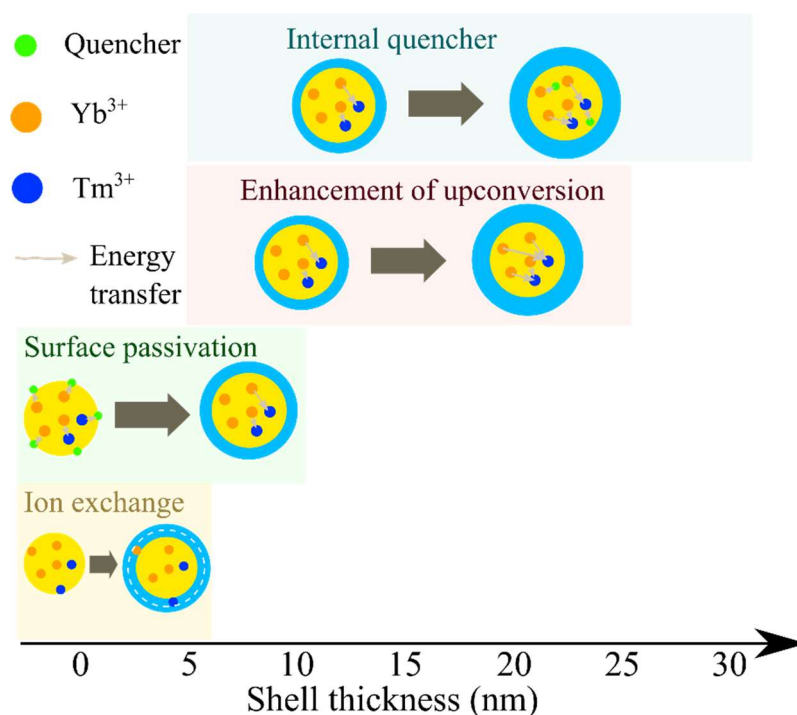
Figure 3.7 The physical process for core-shell UCNPs with different shell thicknesses: Ion exchange effect results in a smaller effective shell thickness (white break lines) than physical shell thickness. This difference in thickness became constant when the physical shell thickness is larger than 5nm. Surface passivation plays a considerable role for the intensity enhancement from the thickness 0 nm to 8.4 nm. The enhancement of upconversion efficiency and internal quenchers becomes serious when the thickness is as thick as 25.9 nm and more.

3.3.3 Performance of filter-based spectrometer

To further demonstrate the performance of the spectrometer, the time-resolved spectrum from a single UCNP was measured.

Time-resolved spectrum is a technique used to study dynamic processes in materials utilizing spectroscopic methods. With the illumination of pulsed lasers, the processes as short as 10^{-16} seconds can be researched. When measuring the time-resolved spectrum, the spectrum intensity is measured with the time tracking at each wavelength and the excitation laser is turned on and off at designed time. Compared with normal spectrum, the time-resolved spectrum has a time axis, which has the laser on, and off on fixed peroid.

The time-resolved spectrums of the UCNPs with different shell thicknesses is shown in Figure 3.8 (a-d). Figure 3.8 (a) and (c) exhibits 3D and 2D plots of the time-resolved spectrum on 0.5% mol Tm^{3+} and 20% Yb^{3+}-doped single UCNPs. To the best of our knowledge, this is the first demonstration of its kind. The emission intensity from this particle is as low as 60 photon counts per ms. Figure 3.8 (b) and (d) shows the spectrum on a single 8% mol Tm^{3+} and 20% Yb^{3+}-doped UCNP. For this experiment, a 980 nm laser started from -1000 μs and switched off at 0 μs, as labelled with white lines. During the laser operation period, the 0.5% Tm^{3+}-doped UCNP showed an extremely long rising time (see Figure 3.8(c)) compared with the 8% Tm^{3+}-doped UCNP (see Figure 3.8(d)). As shown in Figure 3.8(c), the emission from $^3H_4$ (800 nm) was observed to reach its maximum after the laser had been switched off. This can be attributed to the energy transfer process in the sensitiser. Hence, this technology is significant for the comprehensive study of energy transfer processes, internal quantum efficiency, cross relaxation, and time-resolved multiplexing sensing.
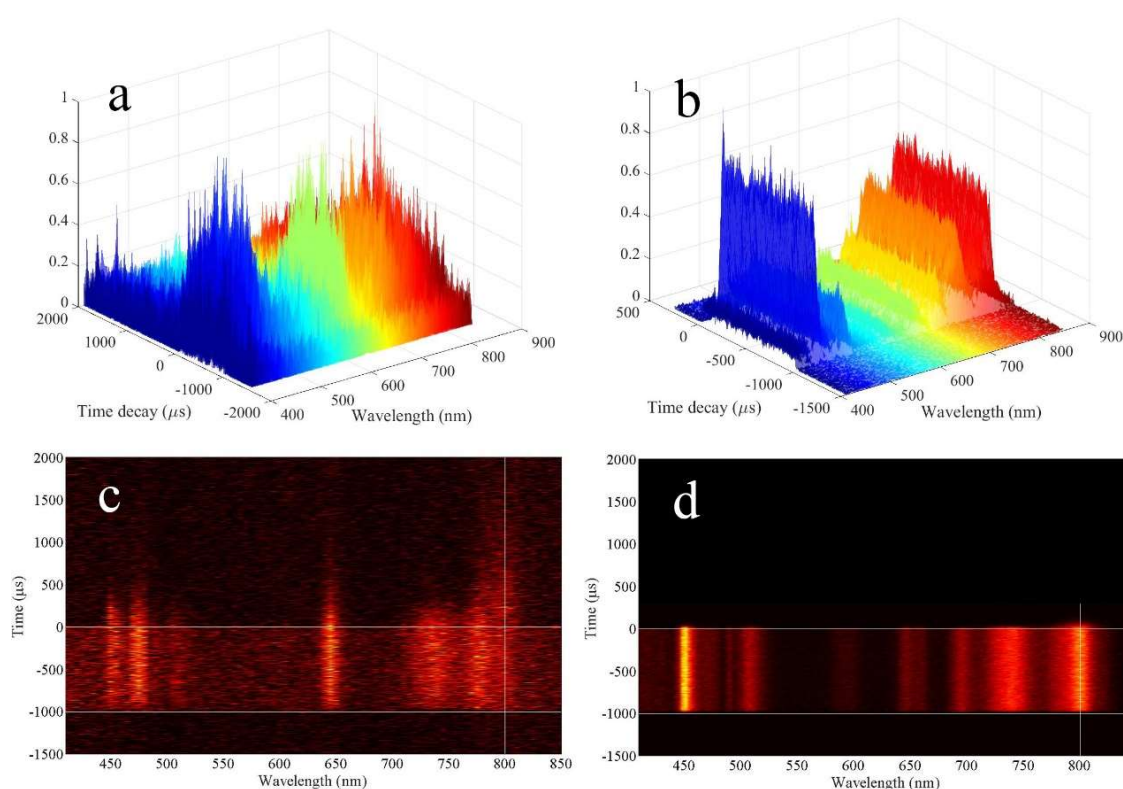
Figure 3.8 Time-resolved spectrum from a single UCNP. 3D (a) and 2D (c) plots of the time-resolved spectrum from a single 0.5% mol Tm^{3+}-doped UCNP with 40 nm diameter. 3D (b) and 2D (d) plots of the time-resolved spectrum from a single 8% mol Tm^{3+}-doped UCNP with 40 nm diameter. The horizontal lines in (c) and (d) define the laser on and off times. The vertical line marks the 800 nm position.

3.4 Conclusion and perspective

We developed an ultra-sensitive spectrometry, when applied, we found the optimal shell thickness is 6.3 nm for 8% Tm^{3+} and 20% Yb^{3+} doped UCNP in terms of luminescent emission and the emission lifetime. UCNPs with 6.3 nm shell thickness showed the highest emission intensity in quantitative comparisons among UCNPs with different shell thickness from 1.1 nm to 29.5 nm. The quantitative spectrum and time-resolved emissions indicated that the surface of UCNPs were gradually passivated due to increasing shell thickness until 8.4 nm. The enhancement in upconversion efficiency played an important role when the shell of the UCNP was larger than 6.3 nm and when an unknown internal quencher

induced a non-radiative transition path. When the shell thickness increased to 25.9 nm, the non-radiative quenching process from the interface of the shell coatings plays major role for the small decrease in intensity. Future work studying quantitative spectrums for UCNPs with different Yb^{3+} and Tm^{3+} concentrations will minimise the unknown non-radiative transition and further reduce the optimised shell thickness. Furthermore, we demonstrated time-resolved spectrums for 0.5% and 8% Tm^{3+} doped single UCNPs. Future work using time-resolved spectrums to calculate internal quantum efficiency (IQE) for single UCNPs will advance knowledge in energy transfer processes for UCNPs.

References

1. Zhou B., Shi B., Jin D., et al., *Controlling upconversion nanocrystals for emerging applications.* Nature nanotechnology, 2015. **10**(11): p. 924.

2. Chan E.M., *Combinatorial approaches for developing upconverting nanomaterials: high-throughput screening, modeling, and applications.* Chemical Society Reviews, 2015. **44**(6): p. 1653-1679.

3. Watson J.M., Marion S.L., Rice P.F., et al., *Two -photon excited fluorescence imaging of endogenous contrast in a mouse model of ovarian cancer.* Lasers in surgery and medicine, 2013. **45**(3): p. 155-166.

4. Wu S., Han G., Milliron D.J., et al., *Non-blinking and photostable upconverted luminescence from single lanthanide-doped nanocrystals.* Proceedings of the National Academy of Sciences, 2009. **106**(27): p. 10917-10921.

5. Nyk M., Kumar R., Ohulchanskyy T.Y., et al., *High contrast in Vitro and in Vivo photoluminescence bioimaging using near infrared to near infrared up-conversion in Tm^{3+} and Yb^{3+} doped fluoride nanophosphors.* Nano letters, 2008. **8**(11): p. 3834-3838.

6. Rodríguez-Sevilla P., Zhang Y., Haro-González P., et al., *Thermal scanning at the cellular level by an optically trapped upconverting fluorescent particle.* Advanced Materials, 2016. **28**(12): p. 2421-2426.

7. Wang C., Cheng L., and Liu Z., *Drug delivery with upconversion nanoparticles for multi-functional targeted cancer cell imaging and therapy.* Biomaterials, 2011. **32**(4): p. 1110-1120.

8. Ma C., Xu X., Wang F., et al., *Optimal sensitizer concentration in single upconversion nanocrystals.* Nano letters, 2017. **17**(5): p. 2858-2864.

9. Zhao J., Jin D., Schartner E.P., et al., *Single-nanocrystal sensitivity achieved by enhanced upconversion luminescence.* Nature nanotechnology, 2013. **8**(10): p. 729-34.

10. Liu Y., Lu Y., Yang X., et al., *Amplified stimulated emission in upconversion nanoparticles for super-resolution nanoscopy.* nature, 2017. **543**(7644): p. 229-233.

11.   Fischer S., Bronstein N.D., Swabeck J.K., et al., *Precise tuning of surface quenching for luminescence enhancement in core–shell lanthanide-doped nanocrystals.* Nano letters, 2016. **16**(11): p. 7241-7247.

12.   Johnson N.J.J., He S., Diao S., et al., *Direct evidence for coupled surface and concentration quenching dynamics in lanthanide-doped nanocrystals.* Journal of the American Chemical Society, 2017. **139**(8): p. 3275-3282.

13.   Yang Y., Zhu Y., Zhou J., et al., *Integrated strategy for high luminescence intensity of upconversion nanocrystals.* ACS Photonics, 2017. **4**(8): p. 1930-1936.

14.   Chen X., Jin L., Kong W., et al., *Confining energy migration in upconversion nanoparticles towards deep ultraviolet lasing.* Nature communications, 2016. **7**: p. 10304.

15.   Wang F., Deng R., Wang J., et al., *Tuning upconversion through energy migration in core–shell nanoparticles.* Nature Materials, 2011. **10**(12): p. 968-973.

16.   Deng R., Qin F., Chen R., et al., *Temporal full-colour tuning through non-steady-state upconversion.* Nature nanotechnology, 2015. **10**(3): p. 237.

17.   Liu J., Chen G., Hao S., et al., *Sub-6 nm monodisperse hexagonal core/shell NaGdF$_4$ nanocrystals with enhanced upconversion photoluminescence.* Nanoscale, 2017. **9**(1): p. 91-98.

18.   Wang Y., Liu K., Liu X., et al., *Critical shell thickness of core/shell upconversion luminescence nanoplatform for FRET application.* The journal of physical chemistry letters, 2011. **2**(17): p. 2083-2088.

19.   Ma C., Xu X., Wang F., et al., *Probing the interior crystal quality in the development of more efficient and smaller upconversion nanoparticles.* The journal of physical chemistry letters, 2016. **7**(16): p. 3252-3258.

20.   Gargas D.J., Chan E.M., Ostrowski A.D., et al., *Engineering bright sub-10-nm upconverting nanocrystals for single-molecule imaging.* Nature nanotechnology, 2014. **9**(4): p. 300-305.

21.   Zhang L., McKay A., and Jin D., *High-throughput 3-dimensional time-resolved spectroscopy: simultaneous characterisation of luminescence properties in spectral and temporal domains.* RSC Advances, 2013. **3**(23): p. 8670-8673.

22.   Lu Y., Zhao J., Zhang R., et al., *Tunable lifetime multiplexing using luminescent nanocrystals.* Nature Photonics, 2014. **8**(1): p. 32-36.

23.   Fan S., Gao G., Busko D., et al., *Monodisperse β-NaYF₄: Yb³⁺, Tm³⁺ hexagonal microplates with efficient NIR-to-NIR up-conversion emission developed via ion exchange.* Journal of Materials Chemistry C, 2017. **5**(37): p. 9770-9777.

24.   Fan S., Gao G., Lin Z., et al., *Highly stable and efficient pure green up-conversion emission of rod-like β-NaGdF₄: Yb³⁺, Ho³⁺ submicro-crystals via ion-exchange for fluorescent labeling.* Journal of Materials Chemistry C, 2018. **6**(19): p. 5210-5217.

25.   Hudry D., Busko D., Popescu R., et al., *Direct evidence of significant cation intermixing in upconverting core@ shell nanocrystals: Toward a new crystallochemical model.* Chemistry of Materials, 2017. **29**(21): p. 9238-9246.

26.   Dong C., Korinek A., Blasiak B., et al., *Cation exchange: a facile method to make NaYF4:Yb, Tm-NaGdF₄ core–shell nanoparticles with a thin, tunable, and uniform shell.* Chemistry of Materials, 2012. **24**(7): p. 1297-1305.

27.   Zhang F., Shi Y., Sun X., et al., *Formation of hollow upconversion rare-earth fluoride nanospheres: nanoscale kirkendall effect during ion exchange.* Chemistry of Materials, 2009. **21**(21): p. 5237-5243.

Chapter 4. Single particle interference: 3D super-resolution position sensing

4.1 Introduction

4.1.1 Super resolution technique

The development of the super-resolution technique in the last decade has largely changed the picture of scientific research, especially with respect to cellular bioimaging research. This technique has facilitated discoveries and new knowledge in cell biology and its developer was honoured with the 2014 Nobel Prize in Chemistry.

Before the super-resolution technique was invented in the 1990s, the optical imaging method was limited by the "diffraction limit". It means that the resolution of microscopy was limited by optical diffraction because of the beam size and lens size constraint. The diffraction limit is caused by airy disk obeys the Abbe rule, which is:

$$\text{d} = \lambda/2nsin\alpha$$

where d is the resolution, λ is the optical imaging wavelength, n is the refractive index of image media, and α is the maximal half-angle of the cone of light that can enter or exit the lens. The limitation is normally about half of the imaging wavelength.

The key to breaking the diffraction limit is to render the molecules discernible for a short period while preventing other molecules within the same diffraction region from being detected together. Several techniques have been developed based on this principle [1].

STED [2] and reversible saturable/switchable optical linear fluorescence

transitions (RESOLFT) microscopy [3] control energy transitions between states and switch fluorophores on and off at localised positions. While photo-activated localisation microscopy or stochastic optical reconstruction microscopy (PALM/STORM) stochastically turns on single fluorophores, then turns off and later turns on some other fluorophores. With position fitting techniques, the full picture can be reconstructed. This method is also called the coordinate-stochastic method [4, 5]. This kind of method achieves position confining at the cost of time. Another technique is structured illumination microscopy (SIM), which uses a rotation of designed pattern to obtain higher frequency information by deconvolution methods.

Adequate understanding of interactions in all three dimensions (3D) is essential for cell and nanomedicine research. But unfortunately, the axial resolution of current super-resolution technologies remains a significant challenge. As shown in Figure 4.1, the resolution at the XY plane has been largely improved, and resolution can be obtained at the 30 nm level. However, the axial resolution of typical super resolution methods is still around the100 nm level [6]. Zeng compared the performance of super-resolution methods in terms of axial resolution, penetration depth, and scanning speed [7]. As can be seen in Figure 4.2, the current axial resolution methods below 100 nm exhibit a common scanning speed problem, where their speed is either slow or medium. Thus, it is necessary to develop a new method with high axial resolution and as well as high scanning speed.
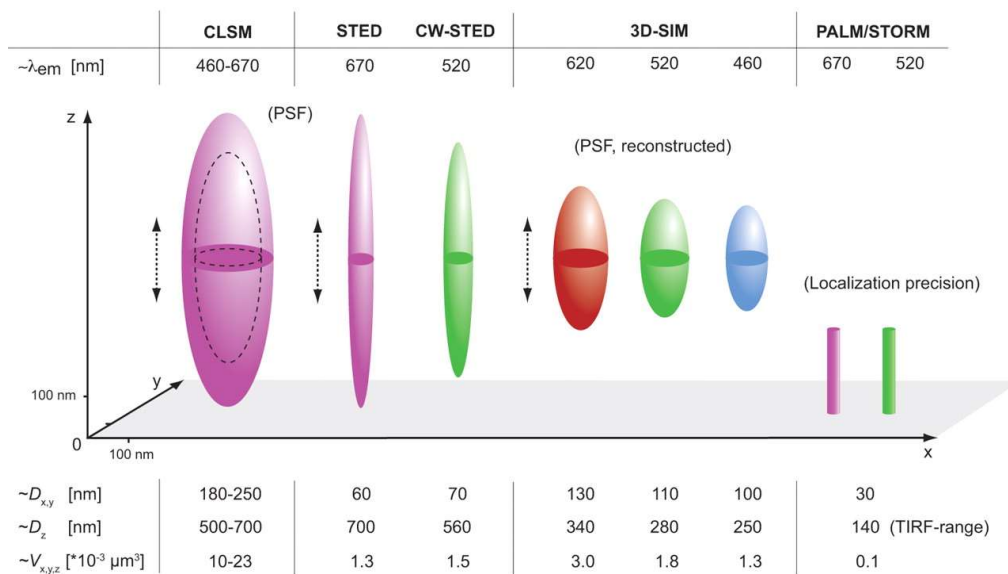
The table at the top of Figure 4.1:

	CLSM	STED	CW-STED	3D-SIM			PALM/STORM	
~λ_{em} [nm]	460-670	670	520	620	520	460	670	520
~$D_{x,y}$ [nm]	180-250	60	70	130	110	100	30	
~D_z [nm]	500-700	700	560	340	280	250	140	(TIRF-range)
~$V_{x,y,z}$ [*10^{-3} μm³]	10-23	1.3	1.5	3.0	1.8	1.3	0.1	

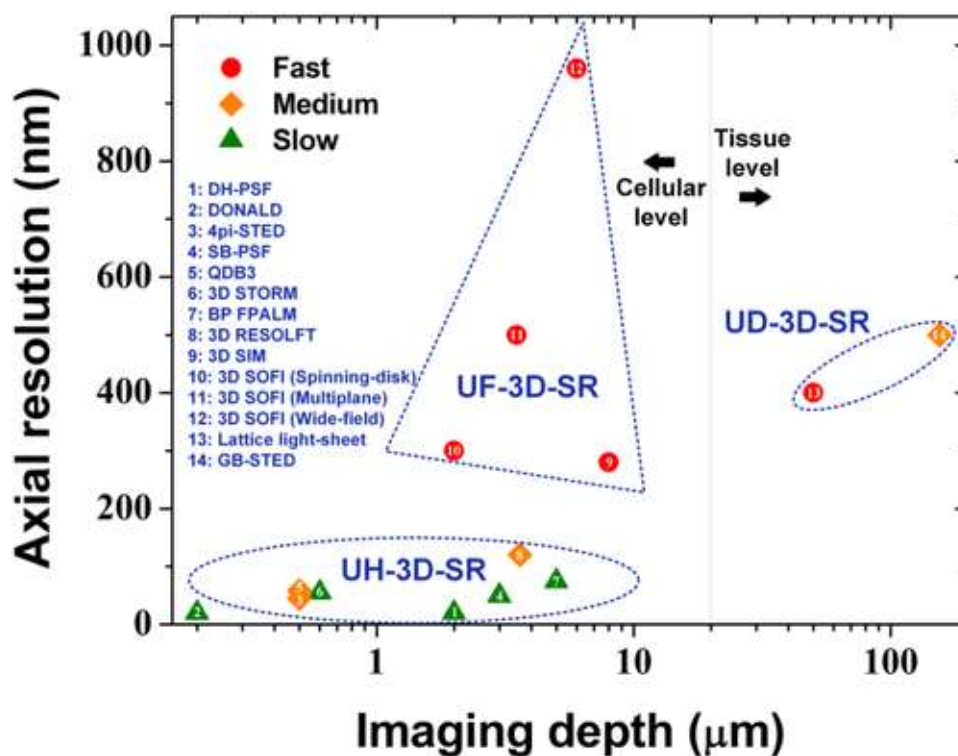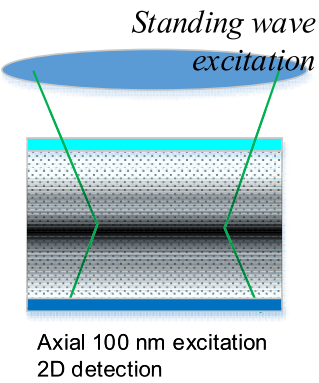*Figure 4.1 The resolution performance of typical super resolution technologies [6].*

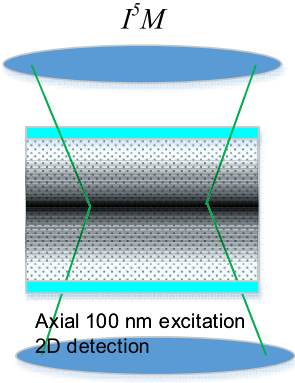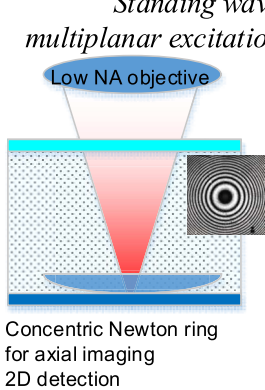*Figure 4.2 Review of current 3D super resolution technologies in terms of axial resolution, scanning speed, and image depth [7].*
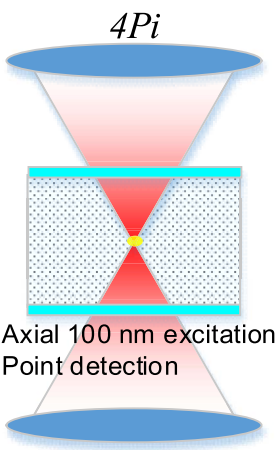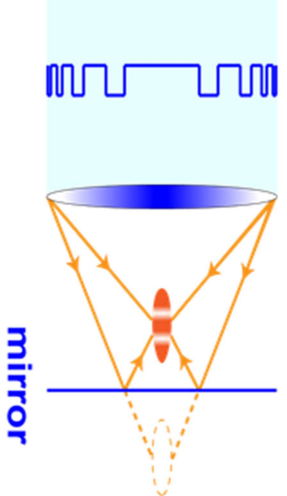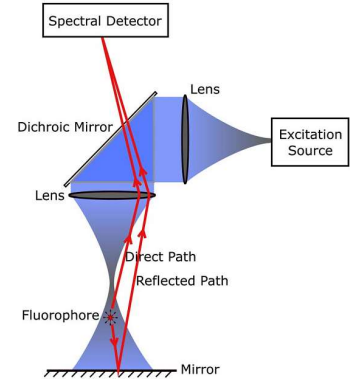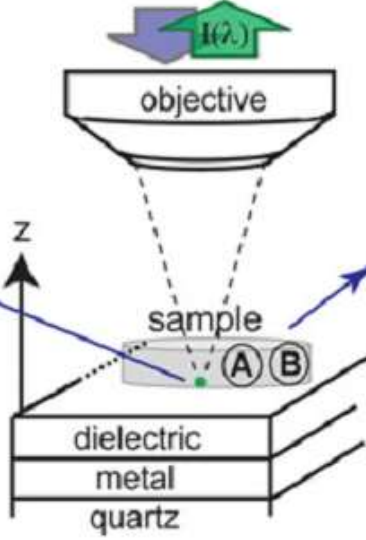
4.1.2 Interference microscopy

Interference super resolution microscopy (InM) [8] is a type of microscopy employing optical interference; it achieves axial resolution beyond the diffraction limitation. This kind of microscopy has been specifically developed to obtain higher axial position.
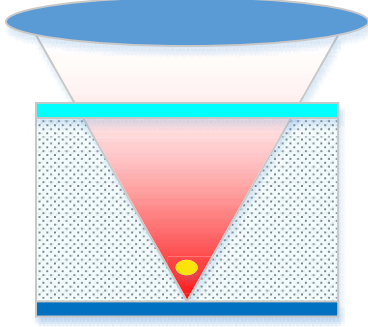
InM usually requires juxtaposed high numerical aperture objectives to produce a standing excitation wavefront and few light pathways to create an interference image of the sample on sensor CCD. Typical InM include standing wave [9, 10], I^5M [11](incoherent interference illumination (I^3) added to image interference microscopy(I^2M), thus I^5M), and 4Pi [12-14](2 objective lens provide solid angel of 4Pi), each of which give sub 100 nm axial resolution.

Table 4.1 Current interference microscopy technologies with resolution and working principles [15].

Technique	Illustration	Description
Standing wave fluorescence microscopy (SWFM)	*Standing wave excitation* Axial 100 nm excitation 2D detection	Based on wide-field microscopy, it can enhance the local electromagnetic field through interference between the incidence and the reflection. However, because the out-of-focus plane fluorescence can also be excited, this technique was not demonstrated experimentally with the mirror.

I^{5}M	*I^{5}M* Axial 100 nm excitation 2D detection	Based on wide-field microscopy of two opposing objectives, I^{5}M generates a thin plane of fluorescent excitation through interference. It is the first to demonstrate experimentally the wide-field axial narrowing concept.
Standing wave multiplanar excitation (SWME)	*Standing wave multiplanar excitation* Low NA objective Concentric Newton ring for axial imaging 2D detection	By employing a low NA objective, a flat mirror, and a plan-convex lens to load the specimen, Newton rings can be generated, in which the number of the ring denotes the axial position of the dye. It can also be used with high NA objective, in which case the mirror should be changed to a plano-convex reflector.
4Pi	*4Pi* Axial 100 nm excitation Point detection	Based on confocal point-scanning microscopy with two opposing objectives, 4Pi can generate an axially narrowed PSF with 100 nm width.

Isotropic focusing		With phase modulation, two real focal spots are generated; one of them is then reflected by a mirror to generate 4Pi like interference.
Spectrally self-interference fluorescence microscopy (SSFM)		In SSFM a mirror with spacer much larger than wavelength ($>10\lambda$) is employed. The fluorescence spectrum carrying the axial position information can be revealed through spectral detection.
Spectrally coded optical nanosectioning (SpecON)		In SpecON, the sample is placed on top of a Langmuir–Blodgett thin film as spacer, before the metal layer. Through careful control of the thickness of dielectric LB film, FRET can be generated between the fluorophore and the metal, resulting in a modulation to the fluorescent emission spectrum with the axial position of the fluorophore. Nanosectioning can be obtained through the FRET analysis.

| Mirror enhanced axial narrowing super-resolution (MEANS) | Axial 100 nm excitation Point detection | In MEANS, a high NA objective is used; with the specimen loaded on a mirror, and a dielectric layer is used as spacer. The local field can be enhanced by 3.6-fold, with axially narrowing detection. The lateral resolution of STED can be improved by two-fold, with better optical sectioning capability. |

Recently, a new type of InM, the mirror enhanced axial narrowing super resolution (MEANs) approach, has been developed; this approach can confine the excitation point spread function (PSF) on the axial position within 110 nm [15]. In turn, this approach substantially enhances both the axial (two-fold) and lateral (six-fold) for STED, without additional system complexity. However, an axial resolution below 10 nm still cannot be achieved.

An approach named spectral self-interference has been used to further enhance axial resolution. This approach can detect the axial position of the fluorophore by analysing the fringes in the fluorescence spectrum created by the interference between directed emitted light and reflected emitted light. Typical methods such as spectrally self-interference fluorescence microscopy (SSFM) [16, 17] and spectrally coded optical nanosectioning (SpecON) [18] can provide sub-10 nm axial resolution. However, the process of monitoring spectrum change along the axial direction is complicated and slow, which limits its application to particle sensing and tracking. Due to the short wavelength excitation used, this

spectral self-interference approach has limited penetration depth and a strong out of focus background.

4.1.3 UCNPs for interference microscopy

UCNPs can absorb multiple NIR photons and generate shorter wavelength photons through the multiple-step excitation process between lanthanide activator ions (e.g., Er^{3+}, Tm^{3+}) and ytterbium sensitiser ions (Yb^{3+}). Due to this large anti-stokes shift, UCNPs are promising for background-free imaging [19]. Owing to the distinct energy levels in activator ions, UCNPs have a multi-colour emission with narrow emission bandwidth, as compared with dyes and semiconductors. Recently, the carrier interaction between these energy levels has enabled STED-like super resolution nanoscopy, which only requires low-power, low-cost, and continuous wave (CW) diode lasers to achieve sub-30 nm optical resolution [20]. High-speed super-resolution imaging of cellular cytoskeleton protein structures has been demonstrated using UCNPs [21]. Most recently, bright and photo-stable UCNPs have been found suitable for eye-visible single nanoparticle tracking and intracellular viscosity detection [22]. However, none of these studies show whether UCNPs can be used for axial distance sensing with nanoscale resolution.

In this work, we report that applying self-interference on single UCNPs can achieve super resolution microscopy for axial distance sensing without suffering from background noise and without the need for a complex optical system. A mirror substrate underneath the nanoparticle results in self-interference between its emission and reflected emission. Taking advantage of the multi-band emission, UCNPs can generate two distinct self-interference patterns by two wavelengths. The intensity ratio

between the two wavelengths can be used to detect particles' axial positions, as the two self-interference patterns are ultra-sensitive to the axial position of the particles. With optimised excitation power, we demonstrate that the nanoscale interferometry sensor (NIS) can be used to achieve a stepped substrate with 10 nm level height difference. We further identified a unique incomplete destructive interference (IDI) phenomenon, based on low degree of coherence on emission from UCNPs. The IDI phenomenon offers the first solution to achieve real-time super-resolution imaging without any scanning process and without a structured or modulated excitation beam.

4.2 System

4.2.1 Fabrication of uniform upconversion nanoparticles

$NaYF_4$: 20%Yb/8%Tm nanocrystals were synthesised similar to our previously reported method [22]. The protocol for synthesising 33 nm $NaYF_4$:20%Yb/8%Tm nanocrystals was similar to producing the core nanocrystals, except for the different quantity of the Na source. The TEM image of a fabricated upconversion nanoparticle in Figure 4.3 shows that the nanoparticle is uniform in size and shape.
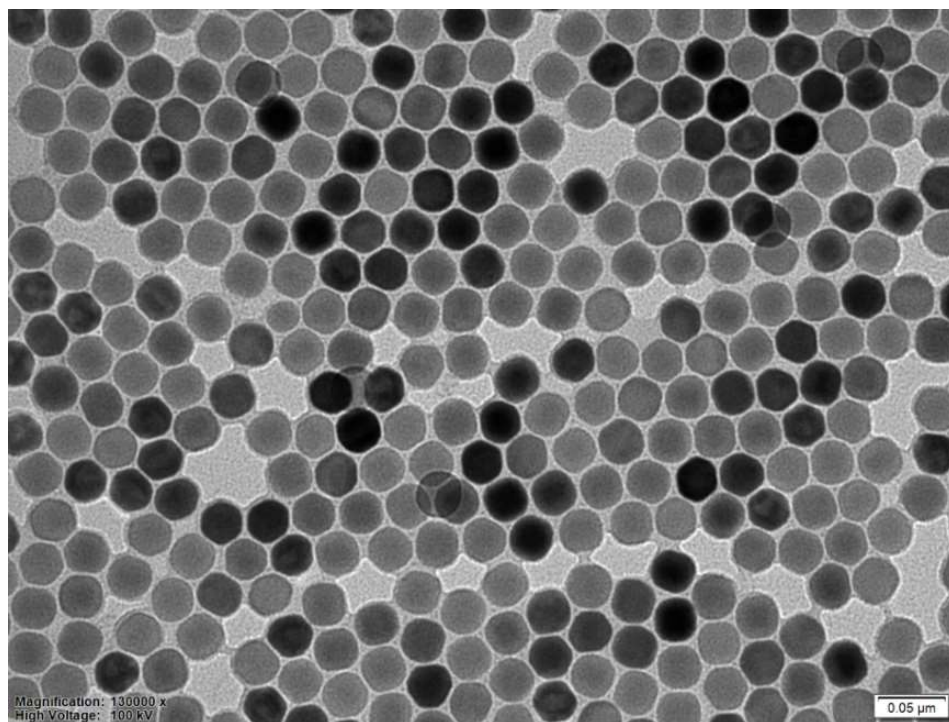
Figure 4.3 TEM image of 33 nm NaYF₄:20%Yb/8%Tm.

4.2.2 Mirror samples

Mirror samples were fabricated by the New South Wales Node of the Australian National Fabrication Facility. There were two types of samples fabricated for this project.

The first type was the normal silver mirror samples with different silicon layer thicknesses acting as spacers. The substrate is a silicon wafer, and then 200 nm silver was deposited on this wafer to serve as a reflector. At last, different thicknesses of silica layer from 50 nm to 500 nm were deposit on the silver to make spacers.

The second type of sample was used to check our axial resolution performance. It used the first type of mirror with spacer thickness about 50 nm as a substrate, and then deposit areas with different thickness (about 30 nm to 55 nm) for distance sensing.

The first type was used in all experiments except in the 4.6 section, where the second type of mirror sample was used to make distance sensing.

4.2.2.1 Fabrication of normal mirror samples

The fabrication of the mirror samples with different thicknesses, from 50-500 nm, was performed according to the following procedure (Figure 4.4):

• surface plasma (SP) clean (4-inch 100 Si wafer);

• Evaporate 10 nm of Ti + 200 nm of Ag + 50 nm of SiO_2 using the PVD75-GP film deposition system;

• Dice wafer into 10 mm by 10 mm pieces.
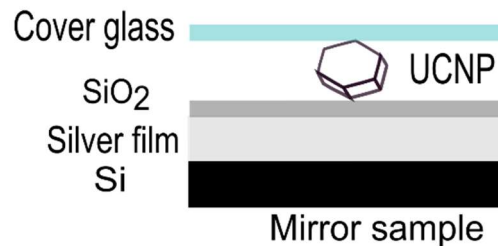
Figure 4.4 Structure of mirror sample.

The thickness of the silica layer is measured with ellipsometry, and the silica thickness samples we fabricated are 55.1, 87.3, 117.1, 138.4, 157, 170.1, 198.2, 251, 310.4, and 467.4 nm. If add the radius of the UCNP (16.5 nm), it will be 71.6, 103.8, 133.6, 154.9, 173.5, 186.6, 214.7, 267.5, 326.9, and 483.9 nm.

4.2.2.2 Fabrication of mirror sample with patterns for distance sensing

This sample was prepared for 10 nm level distance sensing. the following procedure was employed:

1. Alignment markers

Acetone + isopropanol (IPA) + N_2 clean (2 pieces of 10 mm by 10 mm);

Spin photoresist glue nLoF 2020 resist at 5000 rpm for 30s;

Prebake the samples at 115°C for 90 s;

Expose markers at 10 mW/cm^2 for 2.2 s on the mask aligner MA6;

Postbake the samples at 115 °C for 90 s;

Develop for 60 s in AZ836 developer followed by deionised (DI) rinse;

Evaporate 45 nm of Cr using vapor deposition;

Lift off in 80 °C N-Methyl-2-pyrrolidone (NMP);

2. Oxide layers

Spin photoresist glue nLoF2020 resist at 5000 rpm for 30s;

Prebake the samples at 115°C for 90 s;

Expose left rectangle pattern at 10 mW/cm^2 for 2.2 s on the Karl Suss
MA6 mask aligner;

Postbake the samples at 115°C for 90 s;

Develop for 60 s in AZ836 followed by DI rinse;

Evaporate 47.3 nm of SiO$_2$ on the PVD75-GP film deposition system;

Lift off in 80°C NMP;

Spin nLoF2020 resist at 5000 rpm for 30 s;

Prebake at 115°C for 90 s;

Expose middle rectangle pattern at 10 mW/cm^2 for 2.2 s;

Postbake at 115°C for 90 s;

Develop for 60 s in AZ836 followed by DI rinse;

Evaporate 37.3 nm of SiO$_2$ on the PVD75-GP film deposition system;

Lift off in 80°C NMP;

Spin nLoF2020 resist at 5000 rpm for 30 s;

Prebake at 115°C for 90 s;

Expose right rectangle pattern at 10 mW/cm^2 for 2.2 s on the MA6 mask
aligner;

Post-bake at 115°C for 90 s;

Develop for 60 s in AZ836 followed by DI rinse;

Evaporate 57.3 nm of SiO_2 on the PVD75-GP film deposition system; Lift off in 80°C NMP.

4.2.3 Preparation of monodispersed single particle mirror sample

To obtain a well-distributed single nanoparticle sample on each mirror sample, the dip casting method was used rather than the drop casting method we described in Chapter 2 because the surface of mirror samples is different with the glass surface. After measuring the concentration of the original upconversion nanoparticle cyclohexane solution, it was diluted into the concentration of 0.01 mg/ml. Then, 2 ml was placed into a shallow dish. Hold the mirror by a tweezer, and quickly dip it into the prepared dish and then removed and left to air dry.

4.3 Simulation theory, methods, and results

To understand the self-interference of single upconversion nanoparticle on a mirror surface, we carried out simulation of emission and excitation interference on the mirror samples. To perform this simulation, we must introduce interference theory. This section will introduce several typical simulation methods.

4.3.1 Interference and coherence theory

In physics, interference is a phenomenon that two waves overlap to form a resultant wave of greater, lower, or the same amplitude. Interference occurs under three conditions: first, the two waves should have a similar frequency. Second, they should have a stable phase shift. Third, their propagation vector should have the same component.
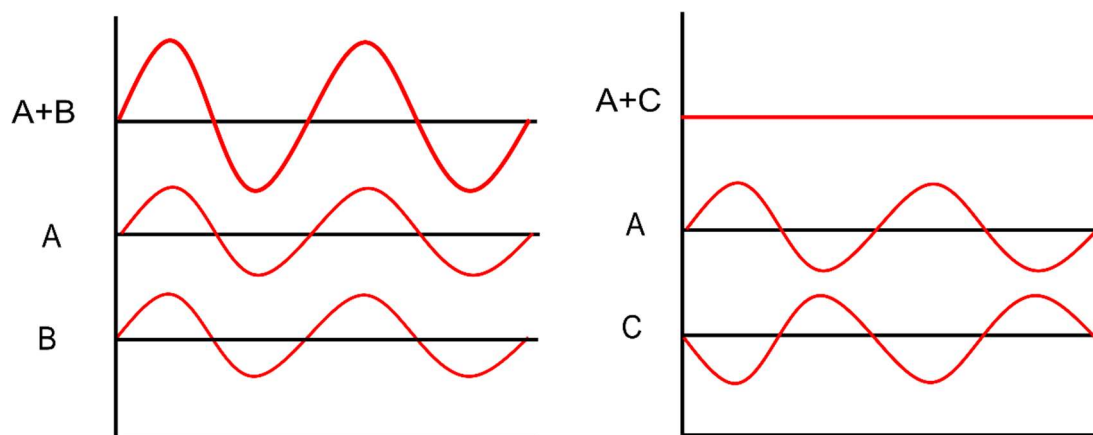
Figure 4.5 Interference between two parallel waves. Left picture is the interference of A and B, which are of same phase. Right picture is the interference of A and C, which are of opposite phase.

Figure 4.5 is an example of interference between two waves. When these two waves are in phase, the two lower waves create constructive interference (left), which results in a wave of enhanced amplitude. When they are 180° out of phase, they will exhibit destructive interference (right) and cause a zero intensity at the wave interference area.

Figure 4.6 Interference at P position between two point light sources Q_1 and Q_2.

To understand interference, the interference of two point light sources can be studied mathematically.

A wave can be described as:

$$\tilde{U}(P) = A(P)e^{i\varphi(P)} \tag{4.1}$$

If there are two light sources Q_1 and Q_2 with spherical radiation at the same vibration frequency in the same media, based on the wave overlapping principle, the complex amplitude of any point P in the space is:
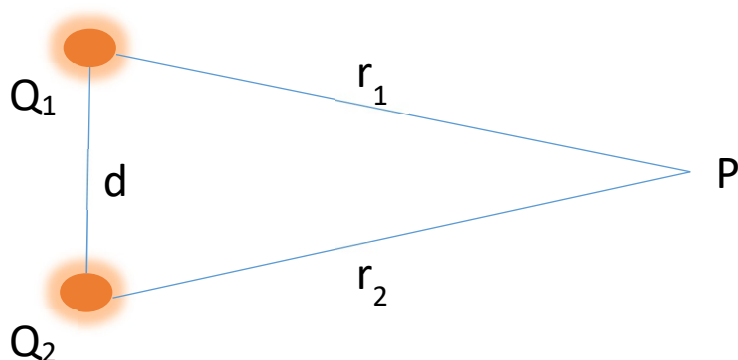
$$\tilde{U}(P) = \tilde{U}_1(P) + \tilde{U}_2(P) \tag{4.2}$$

The intensity of that point is:

$$I(P) = [A(P)]^2 = \tilde{U}^*(P)\tilde{U}(P) = \tilde{U}^*(P) \tag{4.3}$$

$$= (\tilde{U_1}^*(P) + \tilde{U_2}^*(P))\left(\tilde{U_1}(P) + \tilde{U_2}(P)\right)$$

$$= [A_1(P)]^2 + [A_2(P)]^2 + A_1(P)A_2(P)(e^{-i\varphi_1(P)+i\varphi_2(P)} + e^{i\varphi_1(P)-i\varphi_2(P)})$$

Then we have $I(P) = I_1(P) + I_2(P) + 2\sqrt{I_1(P)I_2(P)}cos\delta(P)$ (4.4)

Here $\delta(P) = \varphi_1(p) - \varphi_2(p)$ (4.5)

I(P) is not simply equal to the addition of the intensities coming from the two light sources. There is another component, $2\sqrt{I_1(P)I_2(P)}cos\delta(P)(P)$, which is the phase difference of the waves coming from the light sources. When $\cos\delta(P) > 0$, $I(P) > I_1(P) + I_2(P)$, and there is interference construction. When $\cos\delta(P) < 0$, $I(P) < I_1(P) + I_2(P)$, and there is interference deconstruction.

Two waves are coherent if they have a constant relative phase, the same frequency, the same waveform. Coherence describes all properties of the correlation between a single wave, or several waves or wave packets. For coherence, there are two parts of coherence: temporal coherence and spatial coherence.

Temporal coherence is the measure of coherence between the value of a wave and itself delayed by a fixed phase. It tells how well the wave could interfere with itself at a different time. Temporal coherence tells us how monochromatic a source is. The ideal light source is of one wavelength only, and it can interfere with itself forever. But practically, the real light source always has a wavelength range. The interfere between different wavelengths will make the interference change with time. The bigger the wavelength range is, worse monochromaticity, the coherence will decrease quicker with time.

Spatial coherence is the cross-correlation between two points in a wave for all times. It describes how well the coherence between different positions of a wave and the area which can have significant interference defined as the coherence area. The size of the coherence area is defined as the coherence length, which is a feature of a light source.

Temporal coherence and spatial coherence together make the coherence happen. The coherence degree is measured by the interference visibility, which is defined as $\upsilon = \frac{I_{max} - I_{min}}{I_{max} + I_{min}}$, which means the ratio between oscillating intensity and the average intensity. If we have two waves interfered as equation 4.4 shows, then the interference visibility could be $\upsilon = \frac{2\sqrt{I_1 I_2}}{I_1 + I_2}$.

4.3.2 Simulation methods

Common simulation methods include Fast Fourier Transform (FFT) propagation methods, the diffraction integration method, and the vector integration method. The former two methods are scalar methods and the last one is a vector method.

The FFT method is based on Fourier optics, and the wave is taken a superposition of the plane wave spectrum, which is a continuous spectrum of plane wave component (harmonic functions) for every tangent point on the far-field phase front. FFT is a scalar integration method, using paraxial approximation, which constraint its range of application in the low NA case (NA< 0.7). Some methods originated from FFT, and modified to solve the problems of FFT, such as Hankel Transform method.

Diffraction integration method is a method based on the principle of Huygens-Fresnel. The wave is regarded as a series of expanding spherical waves. Every point from the original wavefront can be treated as a source of secondary wavelets, every point of new wavefront is the integration of these secondary wavelet in that position. This method is still not able to analysis the high NA case since it still using paraxial approximation, as well as the different polarization component.

The vector integration method is crucial for calculating the neighbourhood of the focus of high NA optics. Here, we performed a simulation using a high NA of 1.4 and a near-field within 500 nm. Therefore, the vector integration method was applied [23].

4.3.2.1 Vector integration method

A vector field is an assignment of a vector to represent each point in a subset of a space. A vector field in the plane, for example, can be shown as a group of arrows with a given magnitude and direction, each attached to a point in the plane. In this theory, the light field through the edge of the aperture function is treated as individual plane waves with different propagation directions. All the vectors point to the focus point and the field of the focal region can be seen as the superposition of these plane waves. Vector fields are often used to model, such as the speed and direction of moving fluid throughout space or the strength, as it changes from point to point. Detailed derivation of the method can be found in the work of Török et al. [24].

Figure 4.7 A beam focused by a lens into the focus point.
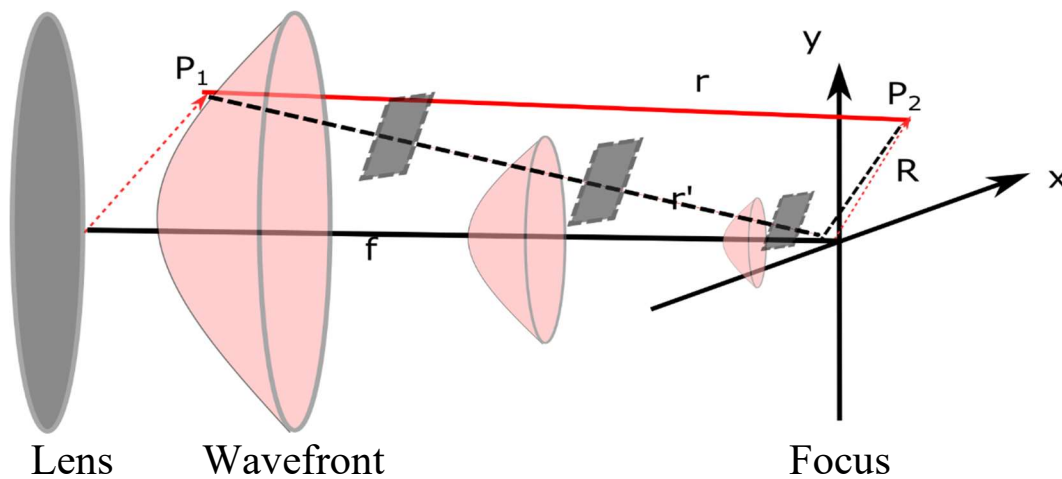
Consider that every point from the original wavefront can be treated as a source of secondary wavelets which will emit a series of secondary disturbances; the new wavefront will be obtained by integrating all these disturbances. As Figure 4.7 shows, the field (U) at point P2 can be calculated by adding all the disturbances of the other point P1 in the aperture plane:

$$U(P_2) = \iint U(P_1) \frac{e^{-ikr}}{r} \kappa(x) dS \tag{4.6}$$

Under assumptions:

(1) after passing through a lens, the incident wavefront is a spherical surface;

(2) the distance between point P1 and P2 (denoted r in Figure 4.7) can be replaced by distance r', which is the flat wavefront propagation distance between point P1 and P2;

(3) the area element dS can be replaced by $f^2 d\Omega$; here, Ω is the solid angle of the area element;

(4) the directional factor $\kappa(x)$ is assumed to be one;

(5) distance r can be assumed to be equal to focal length f.

the time-independent electric field at point P2 can be expressed as below:

$$U(P_2) = \frac{i}{\lambda} \iint P(P_1) e^{-ik\hat{S}\cdot\vec{R}} d\Omega \tag{4.7}$$

where the spherical coordinate represents P1 with origin point at O, the polar angle is θ, the azimuthal angle is φ, and the radial distance is fixed as f since the wavefront is assumed to be spherical. Then, a cylindrical coordinate is used to express P2, originating at O with the azimuthal angle and radial distance r_2. Using the above coordinate system, we have:

$$d\Omega = \sin\theta d\theta d\varphi$$

$$\hat{S} \cdot \vec{R} = r_2 \sin\theta \cos(\varphi - \psi) + Z_2 \cos\theta \tag{4.8}$$

Then, the expression becomes:

$$U(r_2, \psi, z_2) = \frac{i}{\lambda} \iint P_\theta(\theta, \varphi) e^{-ikr\sin\theta\,\cos(\varphi-\psi)-ikz_2\cos\theta} \sin\theta d\theta d\varphi$$

$$(4.9)$$

Here, we can introduce the radial and axial optical coordinates υ and u, defined as:

$$\begin{cases} \upsilon = kr_2 \sin\alpha \\ u = 4kz_2 \sin^2(\alpha/2) \end{cases}$$

$$(4.10)$$

The equations can be modified to:

$$U(\upsilon, u) = \frac{2\pi}{\lambda} \exp(-ikz_2) \int_0^\alpha P(\theta) J_0\left(\frac{\upsilon\sin\theta}{\sin\alpha}\right) \exp\left(\frac{iu\sin^2(\theta/2)}{2\sin^2(\alpha/2)}\right) \sin\theta d\theta$$

$$(4.11)$$

4.3.2.2 Fresnel theory

Here the refractive indices of two adjacent materials are n_1 and n_2 and their interface is a plane, as shown in Figure 4.8. When a parallel light passes through from one side, there will be refraction and reflection. The Fresnel equation describes the reflection and refraction of light when incident on the interface between different optical media.
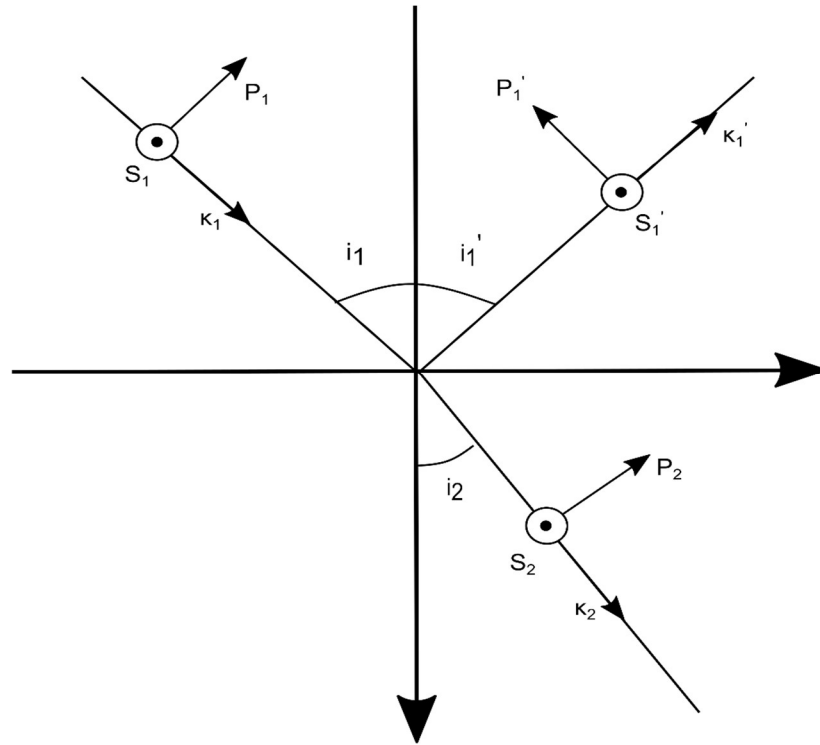
Figure 4.8 The reflection and refraction between two media interfaces.

According to electromagnetic field theory, there are S and P vectors which are vertical and parallel to the light propagation plane. The electric component vectors of the reflection and refraction field follow these equations (Figure 4.8):

$$\widetilde{E}'_{1P} = \frac{\tan(i_1 - i_2)}{\tan(i_1 + i_2)} \widetilde{E}_{1P} \tag{4.12}$$

$$\widetilde{E}_{2P} = \frac{2n_1 \cos i_1}{n_1 \cos i_1 + n_1 \cos i_2} \widetilde{E}_{1P} \tag{4.13}$$

$$\widetilde{E}'_{1S} = \frac{\sin(i_1 - i_2)}{\sin(i_1 + i_2)} \widetilde{E}_{1S} \tag{4.14}$$

$$\widetilde{E}'_{2S} = \frac{2\cos i_1 \sin i_2}{\sin(i_1 + i_2)} \widetilde{E}_{1S} \tag{4.15}$$

Here, $\tilde{E}_{1P}$, $\tilde{E}_{1S}$ are the electric vectors of the incident light, $\tilde{E}'_{1P}$ and $\tilde{E}'_{1S}$ are the electric vectors of the reflection light, and $\tilde{E}_{2P}$ and $\tilde{E}_{2S}$ are the electric vectors of the reflection light. And i_1, i_1' and i_2 are the incident angle, reflection angle, and the refraction index, respectively.

Then, if we want to obtain the transmissivity and reflectivity using the above equation, we need to use the energy conservation principle:

$$\mathcal{R}p + \mathcal{T}p = 1, \mathcal{R}s + \mathcal{T}s = 1 \tag{4.16}$$

Here $\mathcal{R}$ and $\mathcal{T}$ are the energy flux reflection and transmissivity.

The energy flux and intensity are related to the reaction area. The cross-section of the refraction and incident light has a ratio of $\cos i_2/\cos i_1$, so $\mathcal{T} = \left(\frac{\cos i_2}{\cos i_1}\right) T$. For reflection, the cross-section area is the same, so $\mathcal{R}$ is equal to R.

Then, we can transform (4.16) to:

$$Rp + \left(\frac{\cos i_2}{\cos 1}\right) Tp = 1, \tag{4.17}$$

$$Rs + \left(\frac{\cos i_2}{\cos i_1}\right) Ts = 1. \tag{4.18}$$

For the intensity and amplitude of light, the reflection and incident light have the same refractive index; therefore, $R = |\tilde{r}|^2$. Refraction light has a different refractive index compared to incident light, thus we have $T = \frac{n_2}{n_1|\tilde{t}|}^2$.

Then, we have the following relation:

$$|\tilde{r}_P|^2 + \left(\frac{n_2 \cos i_2}{n_1 \cos i_1}\right) |\tilde{t}_P|^2 = 1 \tag{4.19}$$

$$|\tilde{r}_S|^2 + \left(\frac{n_2 \cos i_2}{n_1 \cos i_1}\right) |\tilde{t}_S|^2 = 1 \tag{4.20}$$

We know there are definitions:

$$\tilde{r}_P = \frac{\widetilde{E}'_{1P}}{\widetilde{E}_{1P}} \tag{4.21}$$

$$\tilde{r}_S = \frac{\widetilde{E}'_{1S}}{\widetilde{E}_{1S}} \tag{4.22}$$

$$\tilde{t}_P = \frac{\widetilde{E}_{2P}}{\widetilde{E}_{1P}} \tag{4.23}$$

$$\tilde{t}_S = \frac{\widetilde{E}_{2S}}{\widetilde{E}_{1S}} \tag{4.24}$$

Finally, 4.21)-(4.24) and (4.12)-(4.15) obtain:

$$\tilde{r}_P = \frac{\tan(i_1 - i_2)}{\tan(i_1 + i_2)} \tag{4.25}$$

$$\tilde{r}_S = \frac{\sin(i_1 - i_2)}{\sin(i_1 + i_2)} \tag{4.26}$$

$$\tilde{t}_P = \frac{2 n_1 \cos i_1}{n_2 \cos i_1 + n_1 \cos i_2} \tag{4.27}$$

$$\tilde{t}_S = \frac{2 n_1 \cos i_1}{n_1 \cos i_1 + n_2 \cos i_2} \tag{4.28}$$

Using these equations, we can obtain the reflectivity and transmission at different angles. For our simulations, we need to know the reflection energy phase shift factor, which is $\frac{\sin(i_1 - i_2)}{\sin(i_1 + i_2)}$ for S vector and $\frac{\tan(i_1 - i_2)}{\tan(i_1 + i_2)}$ for P vector. However, our simulations method is not complete as it does not

include the factor of temporal coherence, therefore the simulation of hole is not perfect and need further development.

4.4 Single UCNP interferometer

4.4.1 Single UCNP particle self-interference phenomenon

Confocal microscopy generally provides a wide PSF (Figure 4.9 (a)) which limits the axial location accuracy of nanoparticles with a size smaller than the diffraction limitation. A metallic substrate (e.g., silver layer) can reflect the emission from a single nanoparticle back to itself, thereby creating interference between the emission and the reflected emission. The resultant interference pattern indicates the detecting signal intensity for different distances away from the mirror surface. Experimentally, we keep the detecting plane at the same position as the emitting nanoparticle (surface of SiO_2 layer as shown in Figure 4.4). This interference pattern (Figure 4.9 (b) and 4.9 (c)) can be used to improve the axial resolution for a single nanoparticle's axial locating.

UCNPs are one of the best candidates for single nanoparticle interference due to their unique optical properties. A typical emission spectrum from a single UCNP is shown in Figure 4.9 (a), where the UCNPs are loaded on a normal glass slide, and two distinct emission peaks can be found at 455 nm ($^1D_2$ to $^3F_4$) and 800 nm ($^3H_4$ to $^3H_6$), with sharp emission linewidths of 9 nm and 27 nm, respectively.

With a mirror substrate underneath a UCNP, the interference between the UCNP's original emission beam and the reflected emission beam generates two distinct interference patterns from the two corresponding colours (455 nm and 800 nm) of the emission peaks. Due to the sharp

emission linewidth of UCNPs and resultant feasible degree of interference, the nanoscale position change of UCNPs in the pattern leads to substantial emission intensity changes in both 455 nm and 800 nm bands, and substantial changes in their ratios.
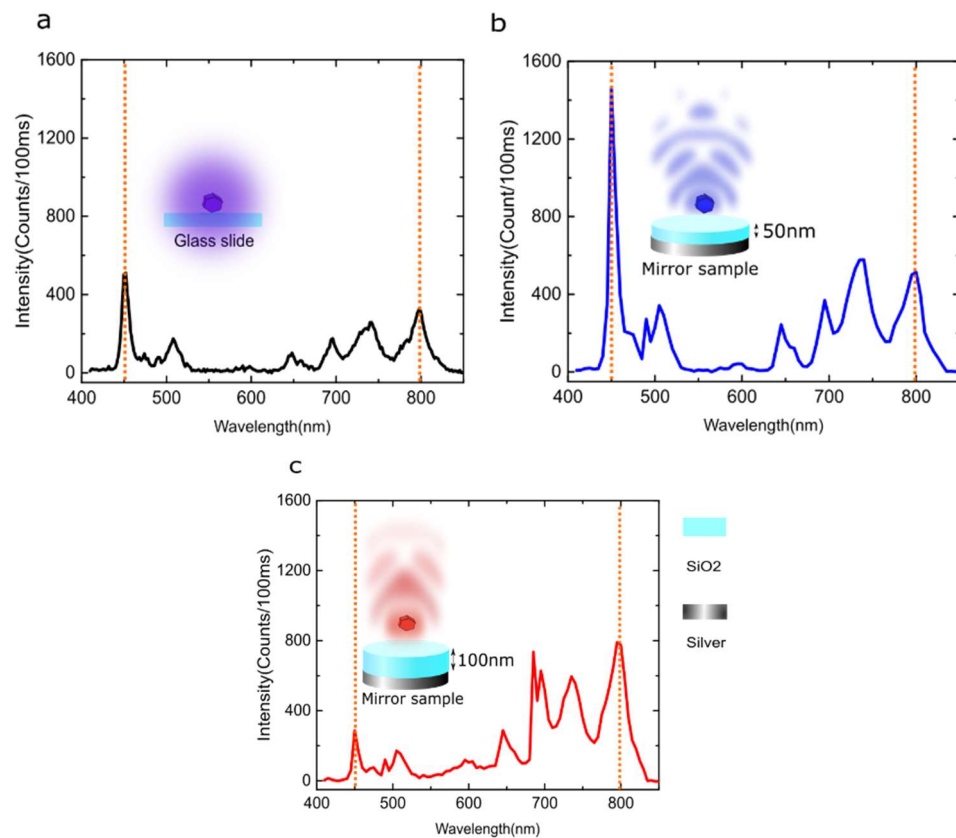

Figure 4.9 Self-interference phenomenon enables sharp emission change for a UCNP placed on a mirror. (a) The UCNP on a transparent glass slide with spherical emission point spread functions (b) Obvious 455 nm emission enhancement when UCNP is placed on a 50 nm mirror, where 455 emission interferes constructively. (c) Obvious 800 nm emission enhancement when UCNP is placed on a 100 nm mirror, where 800 nm interferes constructively.

Figure 4.9 (b) and (c) are the spectrums of the UCNP we measured on the mirror samples with 50 and 100 nm thickness. It should be noted that the UCNPs emission of both 50 nm sample and 100 sample is much stronger than the normal glass slide sample (4.9 (a)). The emission of the 50 nm

sample and 100 nm sample are obviously different in both intensity and ratio. In the 50 nm sample, the 455 nm blue emission band is much stronger than the 800 nm emission. While for the 100 nm sample, the 800 nm emission band is much stronger than the 455 nm emission. Therefore, nanoscale axial position locating can be achieved by measuring the emission intensity or the intensity ratio for 455 nm and 800 nm, which will be introduced later.

4.4.2 Emission interference research

4.4.2.1 Excitation saturation level

When a single UCNP is placed on a mirror, both the excitation and emission will interference and this interaction will determine the final emission intensity. To study the interference phenomenon clearly, we need to fix either the emission or excitation. There is one way to separate out the emission interference factor which is increasing excitation power level to make photoluminescence (PL) intensity saturate so that all the particles at different distances have the same original emission input intensity. Thus, the final emission signal collected is caused by the emission interference effect.

As shown in Figure 4.10, the PL intensities of the full spectrum, the 455 nm emission and the 800 nm emission are all saturated when the excitation power exceeds 10 mW. This is because excitation is increased on mirror samples. More detailed study of the non-linear power-dependent property of UCNPs could be found at Ref.[20].

Thus, the upconversion nanoparticles will actually receive more excitation than on normal glass slide samples. Therefore, if we use 100

mW excitation power, upconversion nanoparticles on all mirror samples will be saturated and have the same original input emission intensity. In that case, we could study the emission interference effect.
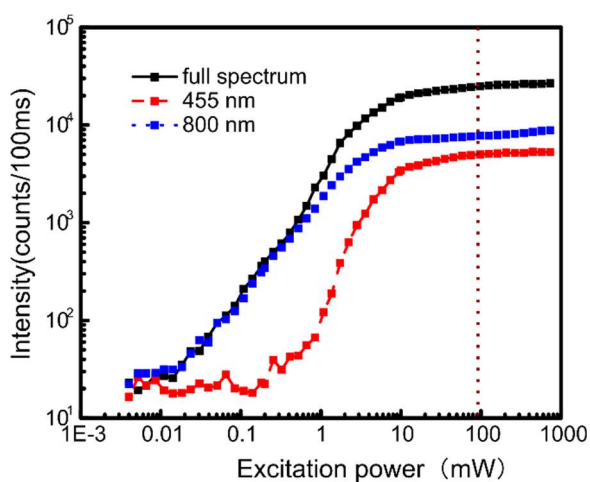

Figure 4.10 The power dependent PL intensity of different emission bands (455 nm band, 800 nm band, and the full spectrum band). All the emission intensities are saturated when the excitation power exceeds 10 mW.

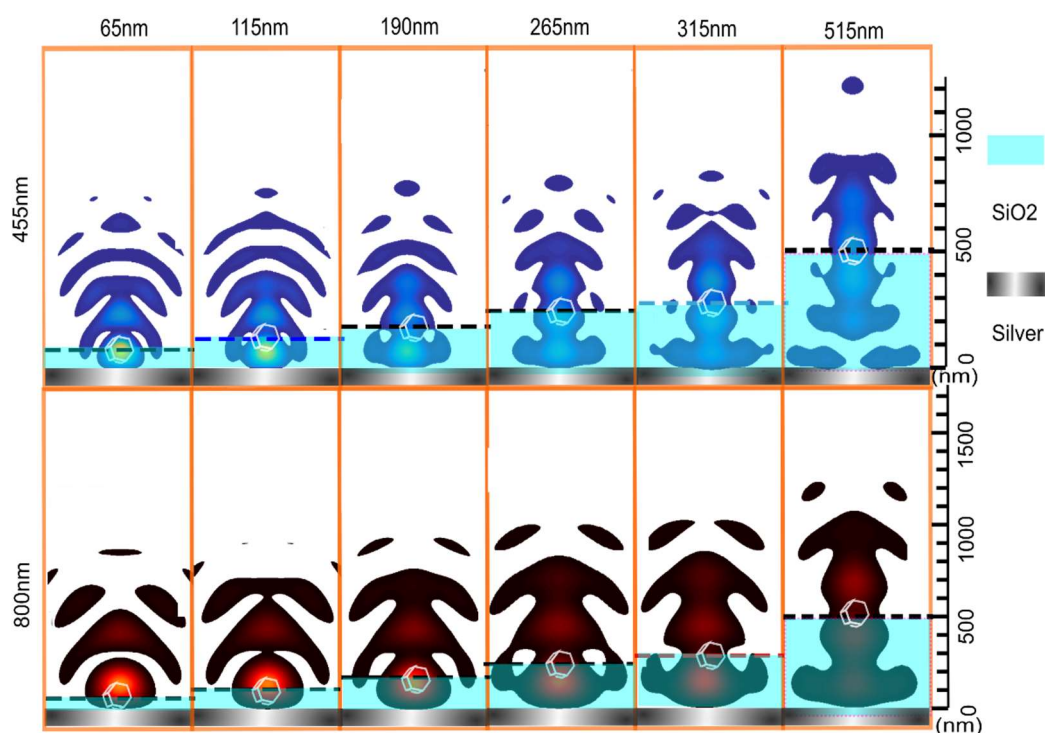## 4.4.2.2 Emission interference phenomenon

Figure 4.11 Simulation results of 455 nm and 800 nm emission distribution patterns when a UCNP is placed at different demitter positions (from 65nm to 515nm) with the same original emission intensity. The patterns change obviously when axial positions change.

Changes in the distance between the emitter (UCNP) (demitter) and the mirror surface will result in different interference patterns. Figure 4.11 simulates how the interference pattern changes for different demitters with the simulation theory introduced in 4.3. The simulation is an initial result, as it only takes the particles as the normal light source, without taking interference between different dipole direction into account.

 In this work, the distance is controlled by tuning the thickness of SiO_2. The break lines in the figure indicate the positions of the UCNPs and the signal collection position.

It is obvious that the interference patterns of 455 nm and 800 nm are dramatically distinct. For the 455 nm emission, the intensity collected is at the bright position initially with 50 nm spacer. With the increase of the demitter, the intensity will decrease will the dark area, then it will increase again. While for 800 nm emission, the intensity will increase at first, and then reduce and increase with the distance. It is also shown that the 455 nm emission changed fast than the 800 nm with distance, which is reasonable as 455 nm wavelength is shorter than 800 nm and have a smaller interference period. It can also be found that, with increased demitter, the intensity distribution will be dispersed from near the mirror surface.
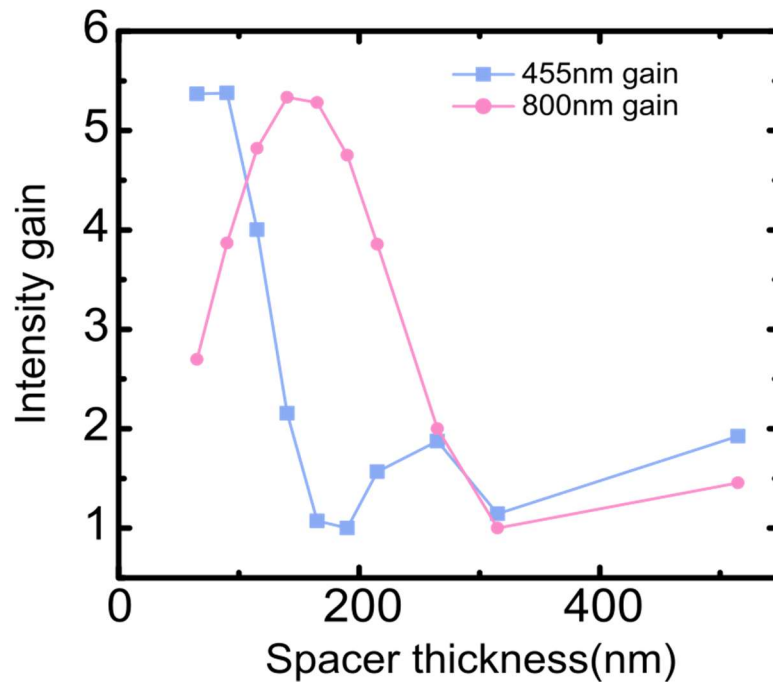
Figure 4.12 Simulation intensity gain results for 455 nm and 800 nm emission intensities at different distances. The simulated demitters are 65nm, 90 nm, 115nm 140 nm, 165 nm, 190 nm, 215 nm, 265 nm, 315 nm, and 515 nm.

The simulated detecting intensity for different demitters is shown in Figure 4.12. The intensity gain value is defined as the ratio between expected intensity and the intensity without interference. Note that this simulation is for the saturated emitter which has stable emission intensity, independent of the excitation change introduced by different spacer thicknesses. It can be seen from Figure 4.12 that the intensity gain can be as high as 5.5 for 455 nm and 800 nm emission at 65 nm and 140 nm, respectively. And in the valley, the gain is closed to 1 which means the intensity is the similar to the intensity of the normal glass slide sample. The change in Figure 4.12 stems from the constructive and destructive point in the interference pattern (Figure 4.11), with a shifted maximum position for different wavelengths.
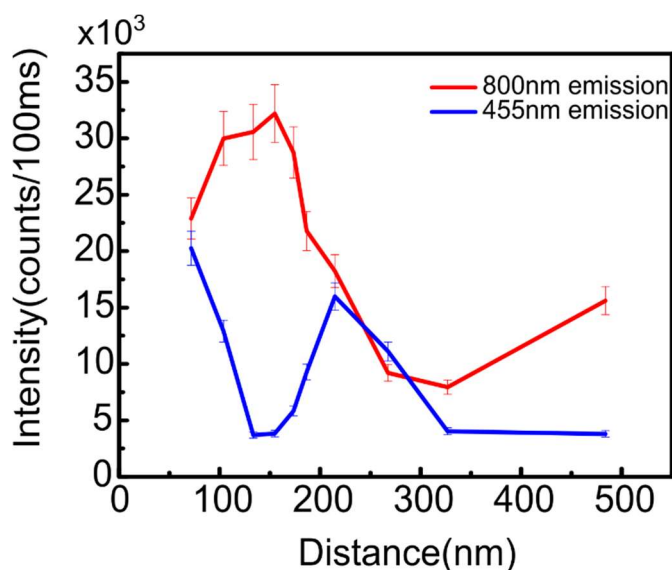
Figure 4.13 Experimental results for PL confocal intensity on samples with different thicknesses (50 nm -500 nm) under excitation power of 100 mW (intensity curve). The distance between the nanoparticle and the mirror is calculated by adding the spacer thickness with the radius of the single UCNP size (16.5 nm). The demitter of the samples are 71.6, 103.8, 133.6, 154.9, 173.5, 186.6, 214.7, 267.5, 326.9, and 483.9 nm. Error bars are included.

To create saturation of the UCNP for different distances, the excitation power was 100 mW, one order higher than the saturation power. We measured the emission intensity from single UCNPs with different demitters. A similar trend in emission intensity is observed in the experimental results (Figure 4.13) compared with our simulation results, where the intensity of 455 nm and 800 nm emission change at similar distances and their curve shape is also similar.

It is obvious that the distance-dependent emission curve of 455 nm is out of phase with 800 nm, which results in a sharp change in the intensity ratio of 800 nm and 455 nm peaks (Figure 4.14). This sharper change benefits the distance sensing resolution.
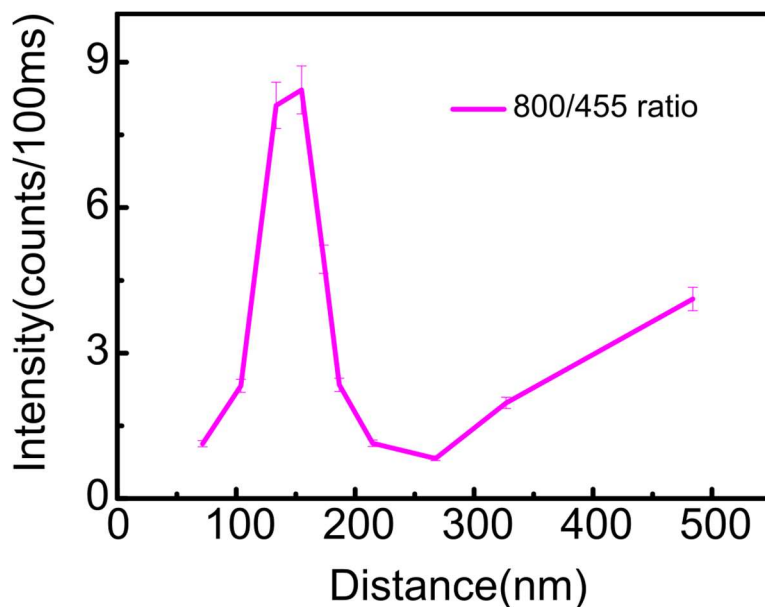
Figure 4.14 NaYF₄ 20%Yb/8% Tm 800 nm/455 nm emission ratio change with distance. The ratio has a very sharp slope due to the large contrast between 455 nm and 800 nm. Error bars are included. The demitter of the samples are 71.6, 103.8, 133.6, 154.9, 173.5, 186.6, 214.7, 267.5, 326.9, and 483.9 nm.

According to Figures 4.13 and 4.14, the calculated intensity or ratio from a single UCNP can be used to recall its distance variation within the monotonically changing range (e.g., the range of 71.6 nm to 133.6 nm).

Obviously, there are some differences between simulation and experimental result of intensity. The simulation of 455nm emission only increase a little bit to 103.8 nm peak and then decrease, but the experiment results show the intensity starts to drop from the beginning. Also, the minimum intensity demitter position is different from the simulation result. For the simulated 800nm intensity gain curve, the initial intensity at 65 nm demitter is just half of the maximum intensity, then increase to the maximum at 140 nm demitter. But the experimental curve shows higher intensity at the 65-140 nm range compared with the maximum intensity.

Furthermore, our measurement shows lifetime, as Figure 4.15 shows. The

particles with 50-250 nm demitter indicate almost the same lifetime for 800 nm emission. And for the 455nm emission, the lifetime of particles near the surface have a shorter lifetime.

The reason for the difference between the simulation and the experiment results is not apparent. It might because our simulation is not perfect or there are other factors involved such as plasmon.
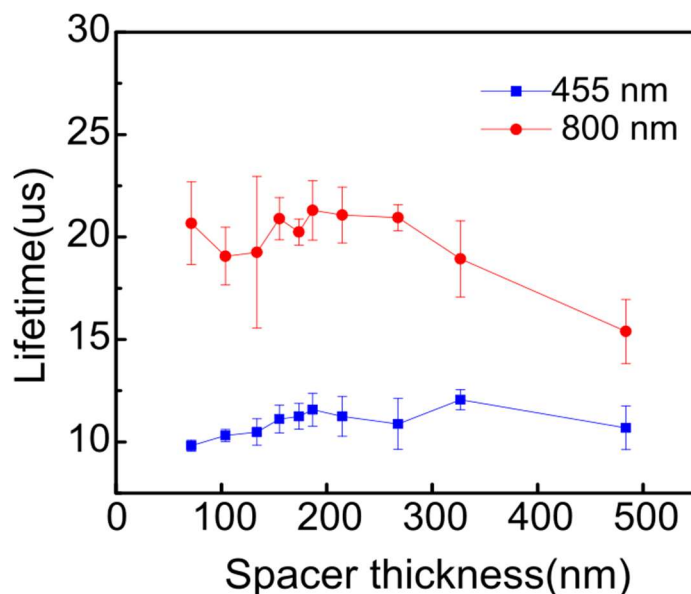

Figure 4.15 the lifetime of the UCNPs (NaYF$_4$ 20%Yb/8% Tm) on different demitters. The results were measured using single UCNPs on these samples with 475±25 nm and 800 ±25 nm bandpass filter. The demitter of the samples are 71.6, 103.8, 133.6, 154.9, 173.5, 186.6, 214.7, 267.5, 326.9, and 483.9 nm.

4.4.2.3 Error estimation method based on intensity and ratio variation

The resolution of distance sensing with intensity curve is based on the slope and variation of intensity curve. The resolution of distance sensing with 800/455 ratio curve is based on the slope and variation of intensity curve of 800/455 ratio curves. The variation of the intensity and ratio curve of 800/455 is determinated by our fabricated upconversion nanoparticles. Due to the significant progress on the synthesis of

upconversion nanoparticles, the size and phase of UCNPs are able to be precisely controlled [25]. Therefore, the variation of intensity or ratio could be better than before to achieve higher resolution.

To estimate the resolution of our nanoscale interferometer, we conduct confocal scannings of UCNP particles on a regular glass slide under 5 mW and 100 mW excitation power levels. 475 ± 25 nm and 800 ± 25 nm bandpass filters were applied when measuring the intensity at 455 nm and 800 nm emission peaks. Figure 4.16 shows the typical confocal scanning results of the single nanoparticle samples excited with 5 mW and 100 mW laser power. Then we measured the emission intensity at 455 nm and 800 nm and further calculated their mean values and variation. Ratio values between these two wavelengths were obtained and the mean ratio value and mean variation were also calculated.

With the variation value of single UCNP under 5 mW and 100 mW laser excitation, the variation in intensity and ratio under similar excitation power levels can be obtained (Table 4.2). Then, fitting the standard intensity and ratio curves using the variation value with interpolation method by MATLAB, the resolution level can be calculated.
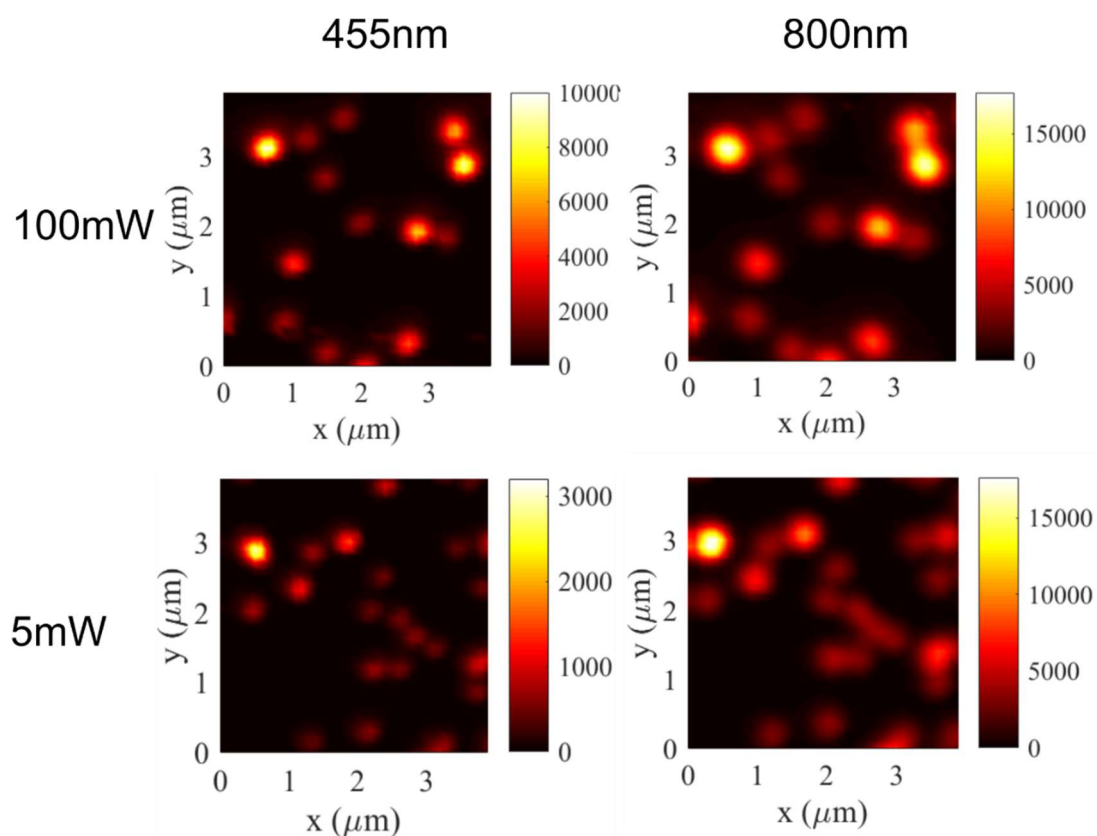
Figure   4.16   Confocal   scannings   of   upconversion   nanoparticles (NaYF$_4$:20%Yb/8%Tm) using 475±25 nm and 800 ±25 nm bandpass filter under 5 mW and 100 mW excitation power levels.

Table 4.2 Mean and standard deviation (STDEV) of single nanoparticle 455 nm emission, 800 nm emission, and the emission intensity ratio of 800/455 nm. (percent means variation percentage of mean intensity)

100 mW	800	455	Ratio	5 mW	800	455	Ratio
Mean	3996.47	2223.17	1.8001	Mean	3376.5	507.928	6.73266
STDEV	318.723	167.089	0.10571	STDEV	354.749	76.4759	0.79007
Percent	7.97512	7.51577	5.87248	Percent	10.5064	15.0564	11.7348

The emission intensity at 455 nm from a single UCNP varies by 7.5% (Table 4.2), and the fitted distribution curve is shown in figure 4.17 (left). The distribution curve shows that the 455 nm emission of single UCNP

has excellent stability, and most of the particles varies within 10%. The calculated spatial resolution based on the single particle interference effect under 100 mW high excitation power is shown in Figures 4.17 (right). This resolution is limited by the variation in the emission intensity of UCNPs. It is shown that this method can achieve sub 40 nm resolution for the range from 71.6 nm to 267.5 nm (Figure 4.17 right). It should be noted that the sensing resolution is higher in the range between 71.6 nm and 133.6 nm and it can be as high as 3 nm for a UCNP with a demitter of 75 nm.
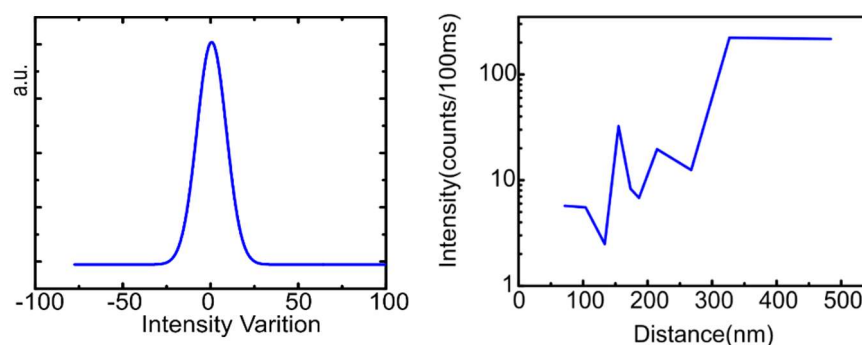

Figure 4.17 (Left)The intensity variation level of the 455 nm emission. The unit of measurement for variation is the percentage of average intensity. (Right) Resolution at different distances when using 455 nm emission intensity as distance sensing. This resolution is achieved by putting the variation of upconversion intensity from Figure 4.17 (left) into the intensity curve in Figure 4.13. The demitter of the samples are 71.6, 103.8, 133.6, 154.9, 173.5, 186.6, 214.7, 267.5, 326.9, and 483.9 nm.

The emission intensity ratio between 455 nm and 800 nm varies by 5.8% (Table 4.2), and the fitted distribution is shown in figure 4.18 (left). The distribution curve shows that the emission ratio of single UCNP has an excellent stability, and most of the particles vary within 10%. It can achieve sub 30 nm resolution for detecting a range from 71.6 nm to 326.9 nm, as shown in Figure 4.18 (right). It should be noted that the sensing

resolution is higher (below 10nm) in the range between 71.6 nm and 186.6 nm, and it can be as high as 3 nm for a UCNP with a demitter of 75 nm. In the next step, we will use these methods to test areas of different thickness and examine the performance that can actually be achieved.
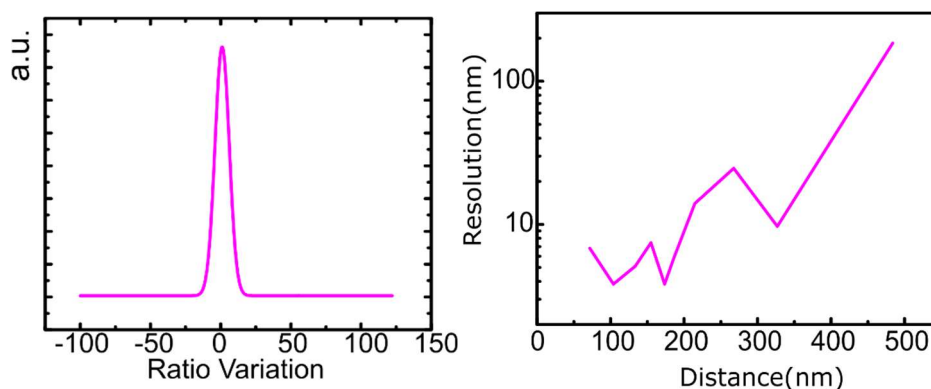

Figure 4.18 (Left)Variation level of The ratio of 800 nm/455 nm emission. The variation unit of measurement is the percentage of average ratio value;(Right) Resolution at different distances when using 455 nm emission intensity as distance sensing. This resolution is achieved by putting the variation in upconversion intensity ratio from Figure 4.18 (left) into the intensity ratio curve in Figure 4.14. the points in the right picture are the thicknesses of the samples we used. The demitter of the samples are 71.6, 103.8, 133.6, 154.9, 173.5, 186.6, 214.7, 267.5, 326.9, and 483.9 nm.

4.5 Excitation interference

Besides interference of the emission of UCNPs, the mirror substrate also leads to strong excitation interference which can be used to further improve the sensitivity and resolution of UCNP distance sensing.

Similar to the emission interference, the interference on the excitation beam (976 nm laser) creates an interference pattern as shown in Figures 4.19. It is shown that the excitation power act on the UCNP is in the dark area (lower intensity) at first. With more demitter, the intensity will

increase and then decrease, which is similar to the 800 nm emission interference pattern. The distribution of the excitation laser power also become more dispersed from near the mirror surface.
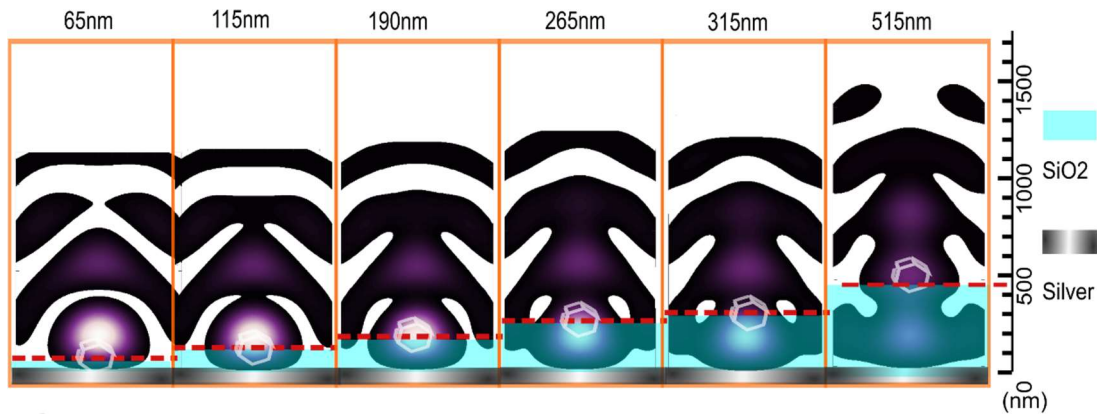

Figure 4.19 Simulation of the excitation power distribution pattern when a UCNP is placed at different demitter positions (from 65 nm to 515 nm) with the same original excitation power. The simulation is based on the simulation method introduced in 4.3.

Figure 4.20 shows the excitation power gain changed with demitter. The excitation gain value is defined as the ratio between expected excitation intensity and the intensity without interference. As the UCNP moves away from the mirror substrate, the excitation power is increased to 2.7 times at the position of 190 nm. Further increases in the demitter will decrease the excitation power. Due to the unique nonlinear power dependent curve of UCNPs (Figure 4.10), the emission from a UCNP changes dramatically with the excitation power. This property stems from the energy transfer mechanism in the upconversion processes. The upconversion process is a nonlinear process where two and more photons are absorbed when one photon is emitted.
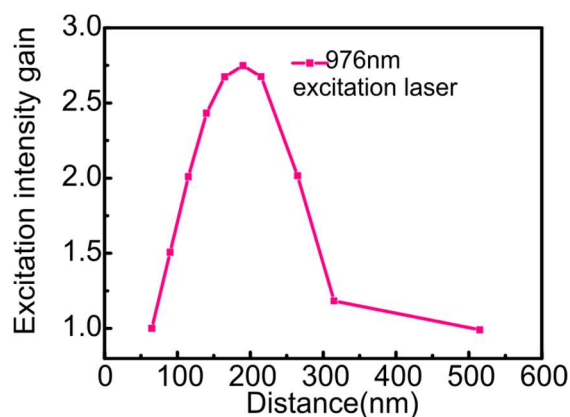
Figure 4.20 The simulated excitation gain curve. Data is from the intensity at the particle positions in Figure 4.19. The 976nm laser is the wavelength of the excitation laser. The excitation intensity gain curve shows how many times the intensity is enhanced compared with standard glass slide case. The simulated demitters are 65nm, 90 nm, 115nm, 140 nm, 165 nm, 190 nm, 215 nm, 265 nm, 315 nm, and 515 nm.

The combination of this excitation-induced emission change with the aforementioned emission interference is shown for 455 nm (Figure 4.21(a)) and 800 nm (Figure 4.21(b)). We measured the fluctuation that occurs at 5 mW excitation, ensuring that the maximum excitation amplitude on the interference pattern was lower than the saturating excitation intensity. Higher excitation power (100 mW excitation) will result in the maximum excitation amplitude exceeding the saturating excitation intensity, leading to smaller fluctuation in emission intensity.

It is notable that the emission from 455 nm is from a four-photon excited state, which leads to a much sharper emission intensity change with increasing pumping power, as compared with the emission from 800 nm which is from a two-photon excited state. This mismatched power dependent response further enhances the steepness in the distance-dependent emission ratio. Benefiting from the excitation beam interference effect and the nonlinear emission response to excitation

power, the emission ratio reaches 35 at the demitter of 140 nm, as shown in Figure 4.21 (c).

The intensity curve of 455nm emission at different excitation power is different. For the 455nm intensity curve at 5 mW excitation power, the samples with demitter in the range of 65 nm to 140 nm changes do not decrease straightly but decrease slowly at first and then decrease faster. It should be noted that even the faster stage is still slower than the 100 mW curve. For the 800 nm emission, the first peak of the emission curve is position at 133.6 nm for 5 mW excitation, while 154.9 nm for 100 mW excitation.

These changes all come from the modulation of the interference excitation. At power levels lower than saturated power, the pumping power change makes the emission change. Therefore, within the range of 71.6 nm to 190 nm, the monotonously increased excitation power modulates with the 455 nm and 800 nm emission curves. It will lead to an increase for samples with longer demitter, which is expressed as the changes we observed in the above paragraph.
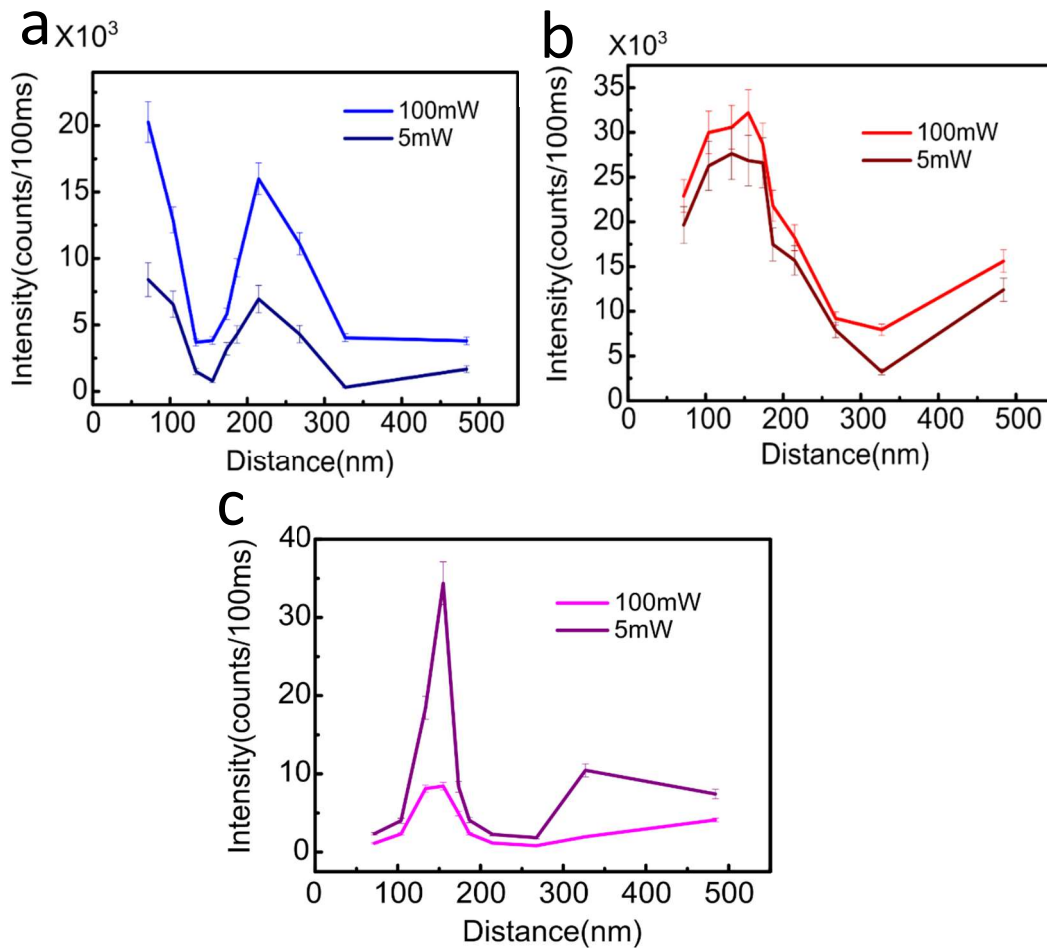
Figure 4.21 The factor of excitation power on PL intensity of NaYF₄ 20%Yb/8%Tm with different demitters. (a) The 455 nm intensity curve with an excitation power of 100 mW and 5 mW. (b) The 800 nm intensity curve at 100 mW and 5 mW. (c) The ratio curve at 100 mW and 5 mW. The demitters of the samples are 71.6, 103.8, 133.6, 154.9, 173.5, 186.6, 214.7, 267.5, 326.9, and 483.9 nm. The error bars are added.

Figure 4.22 (a) and 4.22 (b) compare the estimated distance sensing resolution between excitation powers of 5 mW and 100 mW, applying a 455 nm emission intensity change and an emission ratio between 455 nm and 800 nm, respectively. It is notable that the 5 mW excitation power can achieve a similar resolution of 100mW for these two methods although the signal to noise ratio is worse at 5 mW. It is more exciting that it even has better resolution in some area such as the range between 200 and 300 nm when using the ratio method. The sensing method based on the

emission ratio exhibits slightly better resolutions compared with the intensity method.
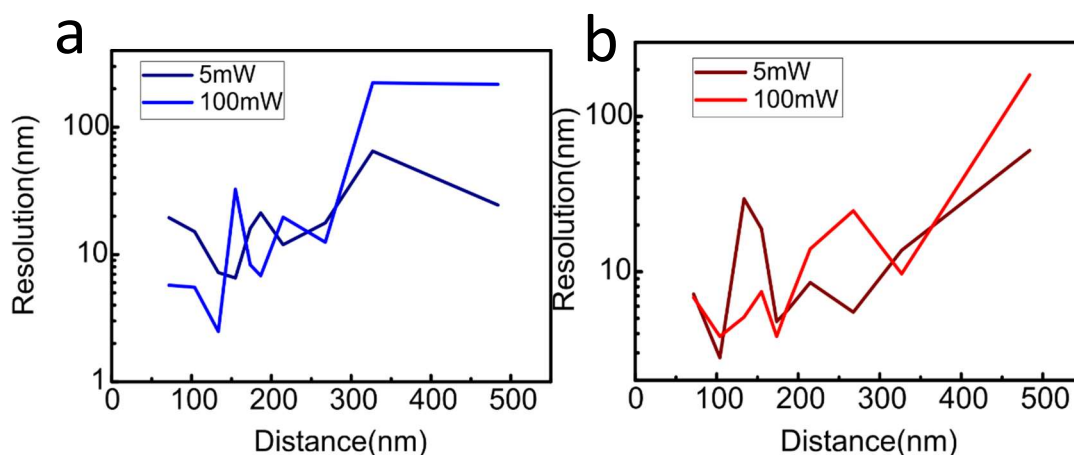

Figure 4.22 (a) and (b) are the axial resolutions at 455 nm intensity of NaYF₄20% Yb/8% Tm at different axial positions, and the 800/455 nm ratio calculated with the collected 455 nm and 800 nm emissions. The resolution is estimated based on the intensity and ratio variation. The demitter of the samples are 71.6, 103.8, 133.6, 154.9, 173.5, 186.6, 214.7, 267.5, 326.9, and 483.9 nm.

4.6 Applications of distance sensing

To test the distance sensing performance of the single UCNP interferometer, we fabricated a sample as shown in Figure 4.23. The fabrication and the composition of this sample were described in Section 4.2.2.2. On this sample, there are two areas with thicknesses of 133.6±3.2 nm and 122.8±6.5 nm, respectively, which were measured by atomic force microscopy (AFM), as shown in Figure 4.23.
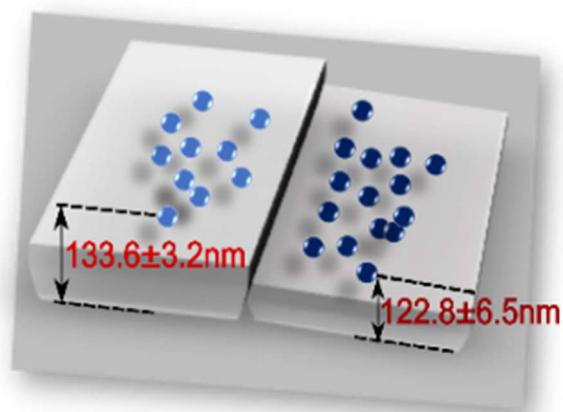
Figure 4.23 Fabrication sample with two thicknesses to test our axial resolution performance.

Calculation of the thickness is performed using the approached shown in the following. First, confocal scanning is performed on these areas with the bandpass filters 475±25 nm and 800±25 nm, as shown in Figure 4.24. Using the confocal data collected, we can obtain the average 455 nm and 800 nm intensity, and then the 800/455 intensity ratio. After substituting these into our calibration intensity curve or ratio curve with the same excitation power (here we used 5 mW), we can determine the thickness of these two areas, as shown in Figure 4.25.

Figure 4.24 Confocal scan results of the fabricated area with two bandpass filters (475/50 nm and 800/50 nm) and. The intensity distribution is shown in the insets of the corresponding confocal figure. (a) and (b) are the blue emission confocal i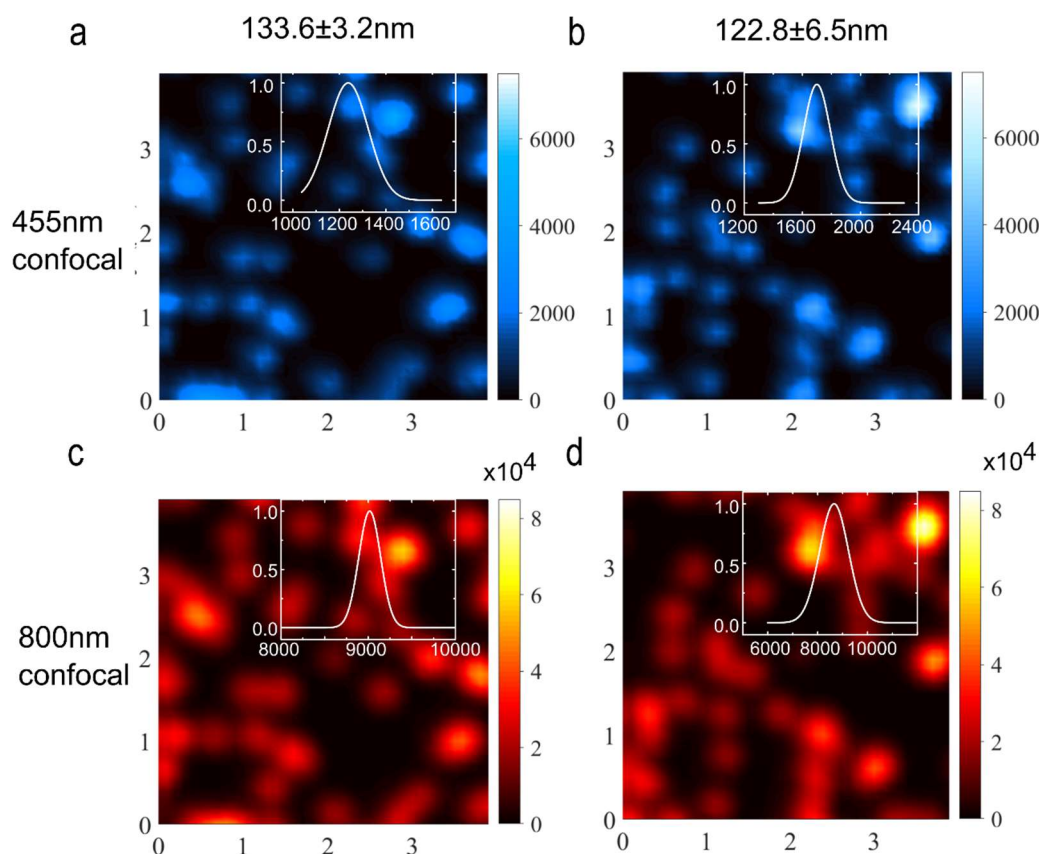ntensity scanning image of 455 nm and 800 nm. (c) (d) are the red emission confocal intensity scanning image of 455 nm and 800 nm. The insets are the intensity mean and variation distribution of the corresponding sample.

The results determined using the 455 nm intensity curve were 139.5±9.4 nm and 129.65±5.5 nm. Then, using the ratio curve, the determined thicknesses were 127.7±3.8 nm and 122.05±3.95 nm. All the results are in the region of the measured AFM thicknesses. This indicates that our single UCNP interferometer can achieve 10 nm level distance resolution. The difference between our distance sensing result and the AFM measured result is caused by the resolution of our distance sensing system, which is determined by the intensity variation of the nanoparticles, the background noise level, the

sensitivity of the detector, and the quality of single nanoparticle upconversion sample. 10 nm distance sensing at the axial direction is of great importance for bioimaging to find more details in cellular environments.
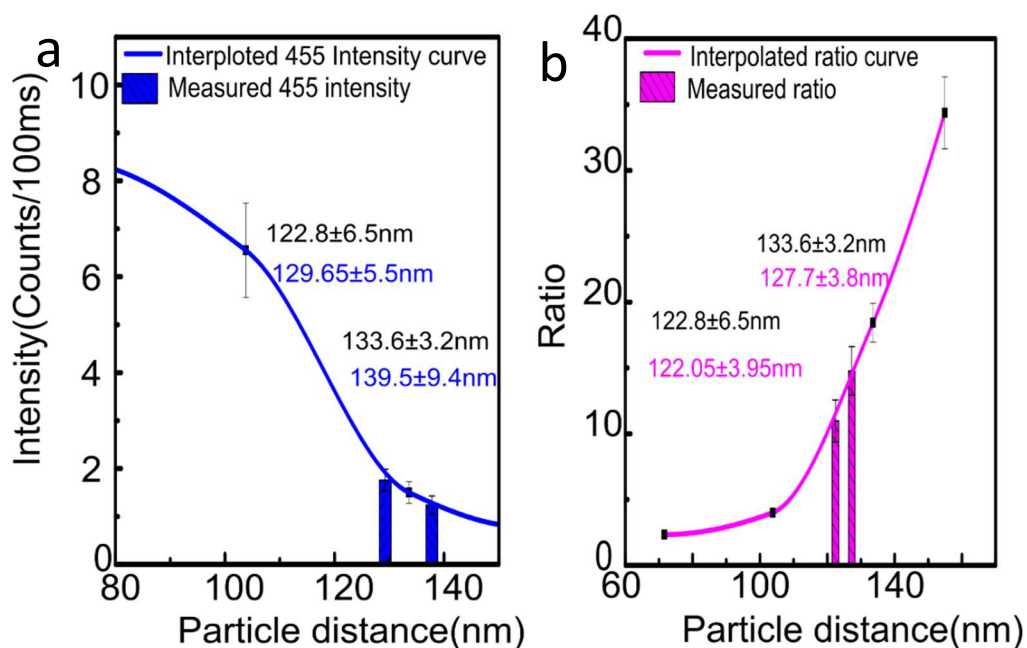
Figure 4.25 The resolved thickness results using (a) 455 nm intensity and (b) 800/455 ratio methods. The blue bar in (a) and pink bar in (b) are the intensity and ratio values we used to interpolate into the curve to get the thicknesses. The results of the 455 nm intensity method are labelled with blue and the results of the ratio method are labelled with purple. AFM results are labelled with black. All measurements and calibration curves were obtained under 5 mW excitation power.

4.7 Application for real-time super resolution

There is one interesting phenomenon when taking the imaging of the single UCNP using CCD camera. As shown in Figure 4.26, the image of single nanoparticles has a dark area in the central. This phenomenon was only found at the images of particles has 154.9 nm demitter with a 455±

25 nm bandpass filter (Figure 4.26 (a)) and particles has 326.9 nm demitter with an 800±25 nm bandpass filter(Figure 4.26 (b)).

From the intensity profile on the right of Figure 4.26 (a) and Figure 4.26 (b), the FWHM of the dips in these images is shown as 150 nm for 154.9 nm demitter sample (455±25 nm bandpass filter) and 200 nm for 326.9 nm demitter sample (800±25 nm bandpass filter). The FWHM is defined as the resolution of this real time super resolution method. It is remarkable that the dip on the PSF has an FWHM beyond the diffraction limitation. And in Figure 4.26 (c), which is a magnified area in Figure 4.26 (a), the distance between the centre of two dark areas can be as close as 310 nm, which is the distance we could resolve on a camera with our eyes. Also, it should be noted that the central dark area cannot be obtained by confocal scanning. It is because the resolution of confocal scanning is about 350 nm, but the full width of the central dark dip is about 300 nm, which is out of the resolution of confocal scanning.

It has to be mentioned that, to our knowledge, this 2D super resolution method (2DSR) offers the fastest super-resolution imaging, with a 100 ms speed to image a 7 by 7 um area (can enlarge the area by a factor of 4 with changing material). It is true video rate large area super-resolution imaging.
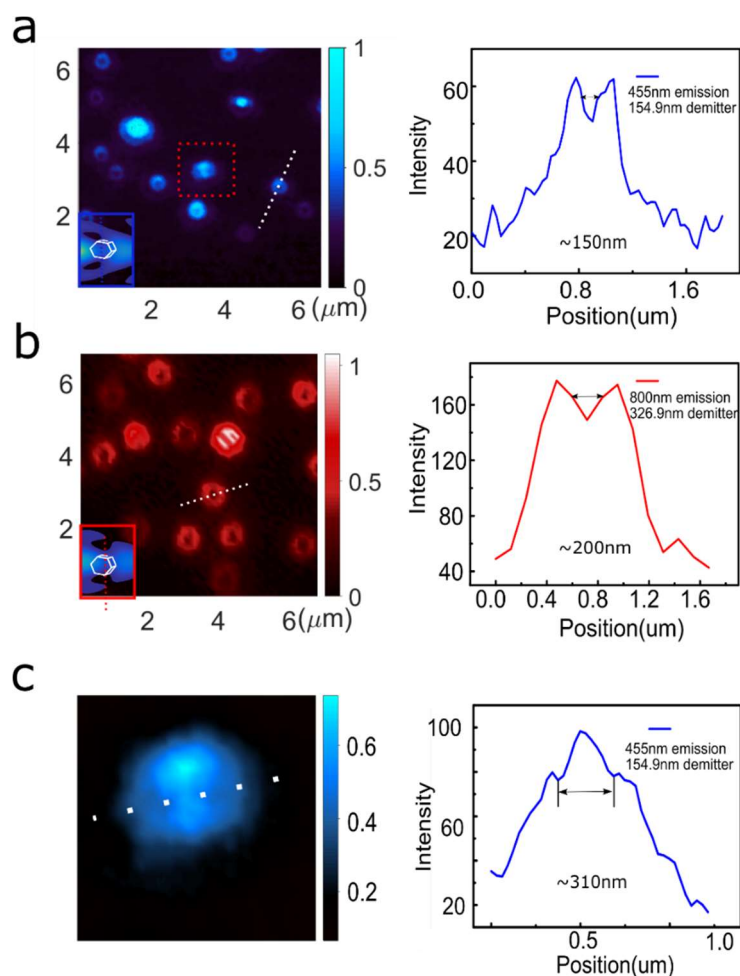
Figure 4.26 Application of the interferometer for 2D super-resolution (2DSR) microscopy. (a)The left picture shows the camera central dark image of UCNPs with 154.9 nm demitter with a 455±25 nm bandpass filter and the right figure is the profile of single UCNP, which is a typical one as labelled in the left camera image with a dashed line. The FWHM of the dip is about 150 nm. (b) The left picture shows the camera central dark image of UCNPs with 326.9 nm demitter with an 800±25 nm bandpass filter and the right figure is the profile of single UCNP, which is a typical one as labelled in the left camera image with a dashed line. The FWHM of the dip is about 200 nm. (c) The magnified image of two particles which is labelled in (a) by a square with the red dashed line. The profile in the right shows two dips in this image with a distance of 310 nm. These pictures clearly show the super resolution effect and the resolution that can be achieved.

Figure 4.27 Confocal resolution and dark area diameter comparison.

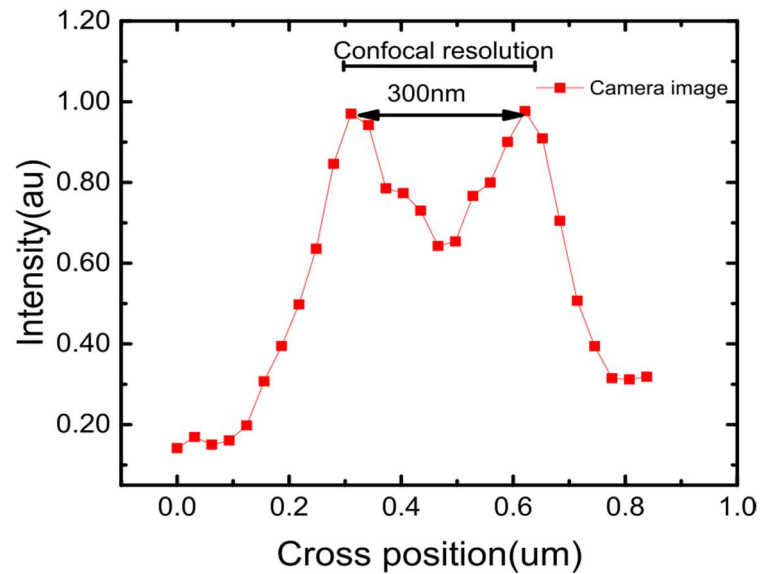This phenomenon could be explained by the destructive interference at these demitter positions. It is interesting to find the emission intensities of these UCNPs drop to a minimum at these demitter positions, as shown in Figure 4.10. The destructive interference generates dimmer emission intensity as the direct emission from the UNCP is out of phase with the reflected emission. It is notable that a UCNP has hundreds of emitters which do not have a synchronised emitting phase. Hence, as a nanoscale light source, UCNPs have inferior temporal coherence but superior spatial coherence as their size is smaller than the diffraction limitation. The combination of the inferior temporal coherence and superior spatial coherence of the UCNP creates a novel Incomplete destruction interference (IDI) phenomenon. This IDI will turn the middle of the PSF of UCNPs to a minimum without changing the amplitude at the edge of the PSF, thereby forming a "donut" shaped PSF on a single UCNP under wide-field excitation.

The IDI should stem from the overlay of emission from electronic dipole with different orientations. As a result of the inferior temporal coherence and superior spatial coherence of single UCNP, a very short coherent

distance will be formed. The internal working principle of IDI still needs more study. The simulation of the electronic dipole with different orientations will show us more detailed explanations.

4.8 Conclusion and perspective

In conclusion, we applied the self-interference of a single UCNP on a mirror surface for 3D location sensing. We thoroughly studied both emission interference and excitation interference. The narrow emission band of the UCNP enables sharp intensity and ratio changes with distance, which enables 10 nm level axial sensing. Further, a central dark particle image is observed at distances where destructive interference occurs. This central dark image can be applied to 2D super resolution with real-time speed.

Through these studies, we have shown the 3D location sensing performance of UCNP self-interference. These studies lay the foundation for real-time 3D super resolution techniques, which could greatly benefit biology research.

References

1. Sahl S.J., Hell S.W., and Jakobs S., *Fluorescence nanoscopy in cell biology.* Nature reviews Molecular cell biology, 2017. **18**(11): p. 685.

2. Hell S.W. and Wichmann J., *Breaking the diffraction resolution limit by stimulated emission: stimulated-emission-depletion fluorescence microscopy.* Optics letters, 1994. **19**(11): p. 780-782.

3. Hofmann M., Eggeling C., Jakobs S., et al., *Breaking the diffraction barrier in fluorescence microscopy at low light intensities by using reversibly photoswitchable proteins.* Proceedings of the National Academy of Sciences, 2005. **102**(49): p. 17565-17569.

4. Betzig E., Patterson G.H., Sougrat R., et al., *Imaging intracellular fluorescent proteins at nanometer resolution.* Science, 2006. **313**(5793): p. 1642-1645.

5. Rust M.J., Bates M., and Zhuang X., *Sub-diffraction-limit imaging by stochastic optical reconstruction microscopy (STORM).* Nature methods, 2006. **3**(10): p. 793.

6. Schermelleh L., Heintzmann R., and Leonhardt H., *A guide to super-resolution fluorescence microscopy.* The Journal of cell biology, 2010. **190**(2): p. 165-175.

7. Zeng Z. and Xi P., *Advances in three‐dimensional super‐resolution nanoscopy.* Microscopy research and technique, 2016. **79**(10): p. 893-898.

8. *Nikon Microscopy U* https://www.microscopyu.com/references/interference-superresolution-microscopy.

9. Bailey B., Farkas D.L., Taylor D.L., et al., *Enhancement of axial resolution in fluorescence microscopy by standing-wave excitation.* nature, 1993. **366**(6450): p. 44.

10. Amor R., Mahajan S., Amos W.B., et al., *Standing-wave-excited multiplanar fluorescence in a laser scanning microscope reveals 3D information on red blood cells.* Scientific reports, 2014. **4**: p. 7359.

11. Gustafsson M.G., Agard D., and Sedat J., *I⁵M: 3D widefield light microscopy with better than 100nm axial resolution.* Journal of microscopy, 1999. **195**(1): p. 10-16.

12.   Dyba M. and Hell S.W., *Focal spots of size λ/23 open up far-field florescence microscopy at 33 nm axial resolution.* Physical review letters, 2002. **88**(16): p. 163901.

13.   Gustafsson M.G., Agard D.A., and Sedat J.W. *Sevenfold improvement of axial resolution in 3D wide-field microscopy using two objective lenses.* in *Three-Dimensional Microscopy: Image Acquisition and Processing II.* 1995. International Society for Optics and Photonics.

14.   Hell S.W., Lindek S., Cremer C., et al., *Measurement of the 4Pi-confocal point spread function proves 75 nm axial resolution.* Applied Physics Letters, 1994. **64**(11): p. 1335-1337.

15.   Yang X., Xie H., Alonas E., et al., *Mirror-enhanced super-resolution microscopy.* Light: Science & Applications, 2016. **5**(6): p. e16134.

16.   Swan A.K., Moiseev L.A., Cantor C., et al., *Toward nanometer-scale resolution in fluorescence microscopy using spectral self-interference.* IEEE Journal of selected topics in quantum electronics, 2003. **9**(2): p. 294-300.

17.   Moiseev L., Ünlü M.S., Swan A.K., et al., *DNA conformation on surfaces measured by fluorescence self-interference.* Proceedings of the National Academy of Sciences, 2006. **103**(8): p. 2623-2628.

18.   Elsayad K., Urich A., Tan P.S., et al., *Spectrally coded optical nanosectioning (SpecON) with biocompatible metal–dielectric-coated substrates.* Proceedings of the National Academy of Sciences, 2013. **110**(50): p. 20069-20074.

19.   Wang F., Banerjee D., Liu Y., et al., *Upconversion nanoparticles in biological labeling, imaging, and therapy.* Analyst, 2010. **135**(8): p. 1839-1854.

20.   Liu Y., Lu Y., Yang X., et al., *Amplified stimulated emission in upconversion nanoparticles for super-resolution nanoscopy.* nature, 2017. **543**(7644): p. 229.

21.   Zhan Q., Liu H., Wang B., et al., *Achieving high-efficiency emission depletion nanoscopy by employing cross relaxation in upconversion nanoparticles.* Nature communications, 2017. **8**(1): p. 1058.

22.   Wang F., Wen S., He H., et al., *Microscopic inspection and tracking of single upconversion nanoparticles in living cells.* Light: Science & Applications, 2018. **7**(4): p. 18007.

23.   Gu M., *Advanced optical imaging theory*. Vol. 75. 2000: Springer Science & Business Media.

24.   Török P., Varga P., Laczik Z., et al., *Electromagnetic diffraction of light focused through a planar interface between materials of mismatched refractive indices: an integral representation.* Journal of the Optical Society of America A, 1995. **12**(2): p. 325-332.

25.   Wang F., Han Y., Lim C.S., et al., *Simultaneous phase and size control of upconversion nanocrystals through lanthanide doping.* nature, 2010. **463**: p. 1061.

Chapter 5. Conclusions and perspectives

5.1 Conclusions

Single nanoparticle characterisation plays an increasingly important role in nanomaterial research. As promising luminescence nanoparticles, UCNPs have received significant attention from researchers in biomedical science and material science. Using the proposed single nanoparticle characterisation, we can achieve much better understanding of the fundamental science of UCNPs, and thus, these participles can be applied in multiple disciplines, including super-resolution imaging, biosensing. and nanophotonics devices.

In Chapter 1, I reviewed the advantageous properties of UCNPs and their applications based on these properties. The literature review showed the promising applications of UCNPS in fields such as bioimaging, biosensing, anti-counterfeiting, and drug release. Further, I reviewed the development of single nanoparticle characterisation technology and demonstrated the significant benefits of this technology for super-resolution imaging, biosensing, displaying, and anti-counterfeit applications. Finally, I introduced my major targets during my PhD which are studying the optimal shell thickness and self-interference phenomenon of UCNPs.

In Chapter 2, I described how to build an advanced single nanoparticle characterisation system (SNCS), including system setup, operation principles, the characterisation process, and programming of the controlling software. Following this, I summarised my collaborative work to demonstrate the applications of the SNCS. This system has shown its significant potential through investigations of concentration quenching,

multiplexing imaging, and single particle tracking.

In Chapter 3, the SNCS was used to investigate the optimisation of shell thickness of core-shell UCNPs. We developed an optical filter-based spectrometer, which is sensitive enough to measure emission rates as low as 60 counts per ms. This is important for the comprehensive study of the energy transfer processes of UCNPs. With its assistance, we achieved comprehensive measurements of the emission intensity, spectrum, and lifetime of single UCNPs. We found that the optimal shell thickness of 6.3 nm resulted in the highest emission brightness for fully emitted wavelengths. The physical process for core-shell UCNPs with different shell thicknesses is discussed.

In Chapter 4, I used the SNCS to study the self-interference effect of a single UCNP. We found that this effect can be used to enhance the emission intensity of UCNPs, and the enhancing factor is high in relation to its phase position (the axial position with respect to the reflecting surface). We further employed this process to generate a nanoscale distance sensor with 10 nm accuracy, which can be used for living cell sensing in the future. Moreover, we have discovered an IDI in the single nanoparticle interference process which results in a doughnut-like PSF with FWHM below the diffraction limitation. This can be used to create real-time super resolution technology.

5.2 Perspectives

The single UCNP characterisation described in this thesis opens up range of novel research directions in the future. In the following, I list three major potential research directions that deserve further investigations.

5.2.1 Single UCNP lasing

The transition of lasers from microscale to nanoscale has been of interest to researchers in both nanophotonics and biophotonics fields because of the potential ability for nanoscale localised excitation and detection. Microscale lasers have been used for sensing, optogenetics, and a broad range of applications in biophotonics. There have been many research efforts attempting to develop a nanoscale laser [1]. Materials such as nanowires [2, 3], quantum dots [4], and microspheres [5] have shown the lasing phenomenon. However, the study of single nanoparticle lasers is really limited by their lower gain.

UCNPs as a nanomaterial are increasingly applied in biophotonics. The development of UCNP lasing is of great importance and is increasingly attracting attention from researchers [6, 7]. This material has the potential to be used to achieve a single nanoparticle laser. Recently, a type of Tm^{3+}-doped energy looping upconverting nanoparticle was embedded onto the surface of a microsphere [8]. With whispering gallery modes (WGM) in the cavity, the UCNPs in the microsphere showed lasing.

In the coming future, a well-designed microcavity could be developed to make single UCNP lasing more effective, or alternatively, a single nanoparticle itself could be developed as a cavity; this would contribute significantly to the development of UCNP applications. Advanced single nanoparticle characterisation and analyses will be of great need in this research.

5.2.2 Mirror enhanced near-infrared emission saturation nanoscopy (NIRES)

Super resolution technology is undergoing significant development. New materials such as UCNPs are attracting increasing research interest [9].

The main benefits of UCNPs as super resolution particles are that their NIR excitation enables high penetration depth and they have low background noise levels. Further, their excitation power level is 2-3 orders lower than traditional probes.

Recently, my colleague developed a multi-photon near-infrared emission saturation nanoscopy technique using upconversion nanoparticles. Through scanning a doughnut shape 980 nm laser, UCNPs can be excited, creating 800 nm emission. The NIR excitation and emission results in a 93 μm penetration depth into liver tissue. The unique excitation power dependent curve resulted in a sub-50 nm resolution (1/20th of the excitation wavelength) [10]. As shown in Chapter 4, a mirror substrate could achieve narrower PSF than normal. With a mirror making the 980 nm laser exhibit self-interference, the shape of the doughnut excitation would be sharper and higher resolution would be expected.
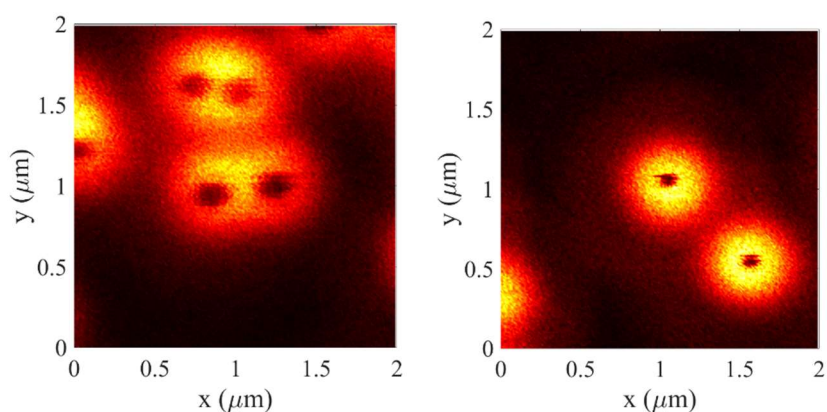

Figure 5.1 the donut beam confocal scanning of UCNPs on a glass slide (left) compare with UCNPs on a mirror surface with 138.4 nm silica layer as a spacer. The left figure has an FWHM of 140 nm while the right figure has 70 nm.

We did confocal scanning of single $NaYF_4$:20Yb%/8%Tm (size=33 nm) UCNP on a silver mirror surface with a 138.4 nm silica layer as a spacer, under 50 mW excitation power. The confocal scanning of the same UCNP

sample on a glass slide was also done. Our initial experiments show that the resolution can be enhanced from 140 nm to 70 nm when using the mirror. It shows the interference effect could enhance the resolution by providing a narrower PSF.

5.2.3 Interaction of multiple emitters within a single UCNP

This would be a continuous work of Chapter 4. As discussed in Chapter 4, we believe the central dark image is caused by the IDI phenomenon. However, the physical origin of the IDI effect remains unclear.

To understand the physical mechanism, we would need an examination of the interaction process among multiple emitters in UCNPs. Potential works including changing doping concentrations, particle size, and particle structure design are possible options to research this. More detailed single nanoparticle characterizations such as lifetime, spectrum, and image are also needed. Ultimately, the result of this research is expected to result in more exciting technologies such as real-time super resolution and super-radiance fluorescence.

References

1.   Hill M.T. and Gather M.C., *Advances in small lasers.* Nature Photonics, 2014. **8**(12): p. 908.

2.   Gao Q., Saxena D., Wang F., et al., *Selective-area epitaxy of pure wurtzite InP nanowires: high quantum efficiency and room-temperature lasing.* Nano letters, 2014. **14**(9): p. 5206-5211.

3.   Yan R., Gargas D., and Yang P., *Nanowire photonics.* Nature Photonics, 2009. **3**(10): p. 569.

4.   Wu J., Chen S., Seeds A., et al., *Quantum dot optoelectronic devices: lasers, photodetectors and solar cells.* Journal of Physics D: Applied Physics, 2015. **48**(36): p. 363001.

5.   Humar M. and Yun S.H., *Intracellular microlasers.* Nature Photonics, 2015. **9**(9): p. 572.

6.   Chen X., Jin L., Kong W., et al., *Confining energy migration in upconversion nanoparticles towards deep ultraviolet lasing.* Nature communications, 2016. **7**: p. 10304.

7.   Zhu H., Chen X., Jin L.M., et al., *Amplified spontaneous emission and lasing from lanthanide-doped up-conversion nanocrystals.* ACS nano, 2013. **7**(12): p. 11420-11426.

8.   Fernandez-Bravo A., Yao K., Barnard E.S., et al., *Continuous-wave upconverting nanoparticle microlasers.* Nature nanotechnology, 2018: p. 1.

9.   Liu Y., Lu Y., Yang X., et al., *Amplified stimulated emission in upconversion nanoparticles for super-resolution nanoscopy.* nature, 2017. **543**(7644): p. 229-233.

10.   Chen C., Wang F., Wen S., et al., *Multi-photon near-infrared emission saturation nanoscopy using upconversion nanoparticles.* Nature communications, 2018. **9**(1): p. 3290.